

**AC trapping  
and  
high-resolution spectroscopy  
of  
ammonia molecules**

Jacqueline van Veldhoven

---

AC trapping and high-resolution spectroscopy of ammonia molecules  
Jacqueline van Veldhoven

Thesis Radboud Universiteit Nijmegen - Illustrated  
With references - With summary in Dutch and German

ISBN-10: 90-9021018-0

ISBN-13: 978-90-9021018-6

NUR: 926

Subject headings: Low Temperatures / Electric Fields / Molecular Beams  
Cover: Ontwerp door de auteur. Afgebeeld is een foto van de AC val. De val bestaat uit twee ringen met twee end caps (een doorsnede is te zien op blz. 66 van dit proefschrift). Omdat de ringen en end caps van glad gepolijst metaal gemaakt zijn, spiegelen hun oppervlaktes zeer sterk. Daardoor zijn beide end caps dubbel te zien, één keer direct en één keer als weerspiegeling.

# **AC trapping and high-resolution spectroscopy of ammonia molecules**

een wetenschappelijke proeve op het gebied van  
de Natuurwetenschappen, Wiskunde en Informatica

## **Proefschrift**

ter verkrijging van de graad van doctor  
aan de Radboud Universiteit Nijmegen  
op gezag van de Rector Magnificus prof. dr. C.W.P.M. Blom  
volgens besluit van het College van Decanen  
in het openbaar te verdedigen  
op maandag 11 december 2006  
om 15.30 uur precies

door

Jacqueline van Veldhoven

geboren op 25 april 1979  
te Ede

Promotor : Prof. dr. G.J.M. Meijer  
Copromotor : Dr. H.L. Bethlem  
Vrije Universiteit, Amsterdam  
Fritz-Haber-Institut der Max-Planck-Gesellschaft, Berlin

Manuscriptcommissie : Prof. dr. W. van der Zande  
Prof. dr. J.M. Doyle  
Harvard University, Cambridge  
Priv.-Doz. dr. E. Peik  
Physikalisch-Technische Bundesanstalt, Braunschweig

The work described in this thesis is performed as part of the research program of the “Stichting voor Fundamenteel Onderzoek der Materie” (FOM), which is financially supported by the “Nederlandse organisatie voor Wetenschappelijk Onderzoek” (NWO), and is performed at the FOM-Institute for plasmaphysics ‘Rijnhuizen’ in Nieuwegein, the Netherlands, and at the Fritz-Haber-Institut der Max-Planck-Gesellschaft in Berlin, Germany.

# Dankwoord

Het zal nu meer dan 5 jaar geleden zijn dat ik op zoek ging naar een stageplek voor mijn studie natuurkunde. Zoals gebruikelijk ging ook ik de verschillende afdelingen van de universiteit langs om inlichtingen over de mogelijkheden in te winnen. Ik heb er toen geen moment over nagedacht dat mijn beslissing wel eens meer dan alleen het komende jaar zou kunnen beïnvloeden.

Wist ik veel dat het feit dat een zekere Gerard Meijer nog steeds één dag per week op de universiteit aanwezig was ertoe zou leiden dat ik huis en haard zou verlaten om drie jaar lang in Berlijn te gaan wonen. En eerlijk gezegd had ik er ook geen idee van dat het project dat mijn uiteindelijke beslissing zou beïnvloeden pas vijf jaar later in gang zou worden gezet, en niet door mij. Het is een wonderlijke wereld... Ondertussen is het fonteinproject in goede handen en als ik zo terug kijk, kan ik alleen maar zeggen dat ik een geweldige tijd heb gehad. En daar heb ik een boel mensen voor te bedanken!

Allereerst de persoon die op elk artikel achteraan staat: Gerard. Gerard, door jouw enthousiasme, gekoppeld aan je onbegrijpelijke vermogen altijd op het kritieke moment in het lab te zijn, heb ik altijd met veel plezier voor je gewerkt. Niet minder belangrijk was echter dat je deur altijd open stond, directeur of geen directeur, en hoewel ik het niet vaak nodig heb gehad, wist ik dat ik altijd bij je langs kon komen als er iets was, en dat je dan achter me zou staan. Omdat je een goede baas was en daarbij nooit uit het oog hebt verloren een leuke vent te blijven, dank je wel.

Hoewel Gerard altijd elke gelegenheid aangreep ook in het lab zijn handen uit de mouwen te steken (getuige een recent waterlek en twee professoren al schroevend onder de vloer), zijn door de jaren heen meerdere mensen verantwoordelijk geweest voor de dagelijkse begeleiding in het lab. Allereerst was daar Rienk, die zijn eigen enthousiasme meebracht en die me mijn eerste stappjes door de wereld van de experimentele fysica bijbracht. Jammer genoeg wilde Rienk niet mee naar Berlijn, en voor de latere spectroscopie-begeleiding nam Jochen het over, de eerste Duitse aanwinst van onze groep. Niet alleen leerde hij Nederlands, zodat ik dit niet naar het Duits hoeft te vertalen, maar bovendien kan ik me ook na deze periode geen enkele computervraag herinneren die Jochen onbeantwoord heeft gelaten. Bedankt en danke!

Degene echter die me het langst begeleid heeft en waarvan ik het vermoeden

heb dat hij de meeste invloed op mijn wetenschapshouding heeft gehad is Rick. Copromotor, naast je soms wat cynische kijk op het leven en je gevoel voor humor dat niet door iedereen begrepen wordt, vond ik het typerend hoe je er altijd voor probeerde te zorgen dat je medewerkers het naar hun zin hadden. Ondanks je vreemde muzieksmaak en puriteinse houding als het op taal aan komt, ben ik onder de indruk van je kiene zin voor wetenschap en je bereidheid om andere mensen te helpen. Onder gebruik van een ietwat ongewone afkorting van mijn naam stond je altijd voor me klaar. Dank je.

Er zijn meer dingen aan een lab verbonden dan alleen wetenschap, en degene die daar het meeste vanaf weet is ongetwijfeld Paul. Van Paul heb ik niet alleen solderen geleerd, maar ook een degelijke labhouding. Altijd in meer dan alleen zijn eigen werk geïnteresseerd, dacht Paul altijd mee om het experiment te verbeteren. Paul, niet alleen daarvoor, maar ook om de verbinding die je naar de rest van Rijnhuizen vormde, om je onmisbare hulp bij de verhuizing naar Duitsland en de vertaalslag die je ons daar hielp maken en niet als minste om jouw en Marianne's gastvrijheid, wil ik je graag hartelijk bedanken.

André, ook jou wil ik bedanken, voor het construeren en bouwen van de afremmer en de AC val, en de klep en het frame en de vacuumkamers en tjonge, wat eigenlijk niet? Maar ook omdat ik bij jou gezien heb dat sommige dingen precies moeten en andere dingen niet en voor de dartuitleg...

As there's more to a lab than only science, so there is more to science than only experiments. Boris, thank you very much for all your calculations, that I could never ever have done by myself and, not less importantly, for all your patient explanations and for being a genuinely nice guy. Do svidania.

Waldo, zonder jou weet ik niet hoe ik ooit ook maar een enkele microgolf in de opstelling had gekregen. Bedankt. Ook Rijnhuizen mag ik niet vergeten, het kleinste dorpje van Nederland, samen met al zijn dorpsinwoners, die Rijnhuizen tot Rijnhuizen maken. Bedankt voor de gezellige sfeer, de bereidwillige infrastructuur, de Rijnhuizen cafes en, niet te vergeten, het omroepsysteem. Mijn eerste medepromovendi, Floris, voor alle filmdiscussies en Bas, wiens poster vrij verwarring boven mijn bureau hing, bedankt. Het is onmogelijk iedereen te noemen, maar ik wil vooral ook de mensen van de werkplaats bedanken en natuurlijk de FELIX groep en de moleculaire dynamica groep, waar altijd wel onderdelen te stelen of terug te vinden waren. En, zeker niet als onbelangrijkste, Hajnal, voor de gedeelde busritten en emotionele ondersteuning en af en toe een omhelzing waar het nodig was. Ik vond je jeugdige uitstraling iedere keer weer verfrissend.

Auch am Fritz-Haber-Institut habe ich viel Unterstützung bekommen und auch viel Spaß gehabt. Danke an Alle, die schon da waren, dafür, dass ihr uns Wilkommen geheißen habt, Inga, Christa, und Bea, und im Labor Jürgen, Manfred, Rolf, Wolfgang, Henrik und Uwe (Hoppe). Später kamen Uwe (Lehmann) und dann Sandy dazu, danke Euch Beiden für die gute Laserbetreuung. Ich hatte noch nie so viel Leistung... Auch die Leute in der Werkstatt und im E-Labor haben uns sehr gut geholfen. Insbesondere möchte ich mich gerne

bei Peter Zilske, Georg und Viktor bedanken, für alle Hilfe beim Schalteraufbau, und ganz im Allgemeinen danke an alle Leute für Euer Verständnis und Verstehen hinsichtlich der ganzen Gruppe dutzender Holländer.

I owe some extensive thanks to the scientific community at the Fritz as well. I guess no one will be surprised if I start with Cyndi. Cyn, I'm truely glad you came to work with us this last one and a half years. For counsel given and counsel taken, for listening and for laughing and for fun, thank you. Cheap enough to be truely an honorary dutch girl, but only when you are spending money on yourself, somehow you always manage to cheer me up when I need it. Thank you for being a friend. And, oh yeah, for taking that picture that got into the FOM Express.

Melanie, danke, dass du weiter über die Machine wachen wirst und dass Du mein Deutsch immer verbessert hast. Für dich hat das leider dazu geführt, dass du auch meine Zusammenfassung verbessern musstest... Es hat mich gefreut mit Dir zusammen arbeiten zu können.

I should give a special thanks to all the girls at the institute, especially those of the girls' room, although in a way, I guess all the girls belong a little to that room... Apart from the already mentioned Cyndi and Melanie, Sophie, Adela, Irena, Kirstin and Undine created a special atmosphere, that I, being the first girl to join the group, could certainly appreciate. I will keep some fond memories of Mr. & Mrs. Smith and that fondue restaurant.

David, too bad you couldn't be with us for longer, it was fun having you around. Nico, Steven, Andreas, Frank, Michael, Marcin, Gert, Bretislav, Wieland, Sam, Horst, Patrick, Ludwig, Peter (both of you), André, Hugo, Koos and all the others in the lab and around it, thanks for the nice atmosphere in the lab and during lunch en Joop en Joost voor de leuke naamsverwarring.

I also want to thank the members of the manuscript committee, Wim, Ekkehard and John, for reading through this entire thesis and giving their OK, with special thanks to John, for being the second professor who had fun solving that recent waterleak.

Ook buiten het werk om heb ik veel steun ontvangen. Zo zijn daar de Marnix-meiden, die door de jaren heen voor veel plezier gezorgd hebben, van vakanties en trilveen tot plakboeken en fatale chocoladefondues. En een van hen zorgde ook voor huisvesting: Andrea, bedankt voor de gezellige tijd samen en de kletsavonden in de keuken en ook Pjotr, dat je het niet erg vond dat ik die laatste maanden ben blijven hangen. Bedankt, Annelies, voor de regelmatige logeeravonden, Jootje, voor de morele ondersteuning, Jess, voor het zelfgemaakte ijs (de volgende keer dat ik wil blijven slapen zal ik het van tevoren zeggen), Anneloes, voor de brood-soepkommen in Boston en Linda, voor die lieve beer.

Ich möchte auch den Brüdern und Schwestern aus der Versammlung Steglitz-Ost sehr danken, die dafür gesorgt haben, dass ich mich in Berlin sehr schnell einleben konnte. Insbesondere bedanke ich mich bei Tamara wegen der gemütlichen Zeit, die wir zusammen verbracht haben, und bei Jörg und Sylvia wegen

der schönen Zeit bei Euch im Garten. Irmpchen und Klaus, danke für die vielen Sonntag Nachmittage, die Ihr meinewegen geopfert habt. Auch die Brüder und Schwestern vom Buchstudium waren immer sehr nett, zumal Angelica und Dirk, die mich so häufig mitgenommen haben und die außerdem so lieb waren, die Aussprache des Wortes 'toll' mit mir zu üben. Wolfgang und Heidi, Helmut und Barbara und vor allem Dethlef und Beate, ich fand Eure Gastfreundlichkeit erwärmend. Danke Euch Allen, ich freue mich sehr Euch kennengelernt zu haben. Ook de broeders en zusters in Ede en Utrecht wil ik graag bedanken voor alle steun die ze me door de jaren heen gegeven hebben. Ramona, bedankt voor alle morele ondersteuning en de gezelligheid.

Het allerbeste heb ik tot het laatst bewaard. Bedankt familie. Luusje en Clau, bedankt dat jullie er zijn. Bedankt voor de Bolero en het Pfaueninsel en de sauna. En Clau en Ed, voor de uitgebreide opmerkingen op mijn samenvatting. Henk en Mini, pap en mam, bedankt, voor mijn leven, en begrip en de ondersteuning door dik en dun, de vele telefoongesprekken en bezoekjes. Ik houd van jullie.

Das war alles sehr toll!

Jacqueline



# Contents

## Dankwoord

<b>1 General Introduction</b>	<b>1</b>
1.1 Cold molecules . . . . .	1
1.1.1 Temperature . . . . .	1
1.1.2 High-resolution spectroscopy . . . . .	2
1.1.3 Cold collisions . . . . .	5
1.1.4 Quantum degeneracy . . . . .	6
1.2 Traps . . . . .	7
1.2.1 Traps for low-field seekers . . . . .	8
1.2.2 Importance of high-field seekers . . . . .	9
1.2.3 Traps for high-field seekers . . . . .	14
1.2.4 This thesis . . . . .	19
<b>2 The hyperfine structure of ND<sub>3</sub></b>	<b>21</b>
2.1 Introduction . . . . .	21
2.2 Experiment . . . . .	24
2.3 Results and Discussion . . . . .	29
2.3.1 Inversion spectra of <sup>14</sup> ND <sub>3</sub> . . . . .	29
2.3.2 Energy levels, fitting parameters and Stark effect for <sup>14</sup> ND <sub>3</sub> . . . . .	31
2.3.3 Energy levels, fitting parameters and Stark effect for <sup>15</sup> ND <sub>3</sub> . . . . .	40
2.4 Conclusions . . . . .	42
<b>3 Decelerated molecular beams for high-resolution spectroscopy</b>	<b>45</b>
3.1 Introduction . . . . .	45
3.2 Stark decelerator . . . . .	46
3.3 Experimental . . . . .	49
3.4 Results and Discussion . . . . .	52
3.4.1 Deceleration and bunching . . . . .	52
3.4.2 Microwave inversion spectrum . . . . .	56
3.5 Conclusions . . . . .	64

<b>4 A versatile electrostatic trap</b>	<b>65</b>
4.1 Introduction . . . . .	65
4.2 The various trapping configurations . . . . .	66
4.3 Experiment . . . . .	71
4.4 Results and discussion . . . . .	73
4.5 Conclusions . . . . .	78
<b>5 An AC electric trap for ground-state molecules</b>	<b>79</b>
5.1 Introduction . . . . .	79
5.2 Trapping principles . . . . .	80
5.3 Electrode geometry . . . . .	81
5.4 Optimal shape . . . . .	84
5.5 Motion in the trap . . . . .	89
5.6 Trapping ammonia molecules in a cylindrical AC trap . . . . .	94
5.7 Summary and Conclusions . . . . .	105
<b>Bibliography</b>	<b>109</b>
<b>6 Samenvatting</b>	<b>119</b>
6.1 Temperatuur . . . . .	120
6.2 Stark afremmer . . . . .	121
6.3 Spectroscopie . . . . .	125
6.4 Een val . . . . .	126
6.5 Ammoniak . . . . .	127
6.6 Mijn onderzoek . . . . .	128
<b>7 Zusammenfassung</b>	<b>131</b>
7.1 Temperatur . . . . .	132
7.2 Starkabremser . . . . .	133
7.3 Spektroskopie . . . . .	137
7.4 Eine Falle . . . . .	138
7.5 Ammoniak . . . . .	139
7.6 Meine Forschung . . . . .	140
<b>Appendix</b>	<b>142</b>
<b>Curriculum Vitae</b>	<b>144</b>
<b>Publicatielijst</b>	<b>145</b>



# Chapter 1

## General Introduction

### 1.1 Cold molecules

Gifted as we are with an inquisitive mind, we human beings always try to understand the world we are living in. Knowing not only that something works, but also how it works, can help us to predict the outcome of situations that may seem radically different, but that have the same underlying principles. Any theory we construct is necessarily based on a set of assumptions of how its different components function and interact with each other. To gain a deeper understanding, we must address these assumptions themselves. As our world consists of matter, understanding the molecular constituents of matter is a prerequisite for any deeper insight into its functioning and interactions. However, under everyday circumstances molecules move around uncontrollably. This makes molecules rather difficult to study. To get more extensive and more accurate data, we need to lower both the velocity and the velocity spread of the molecules, which is equivalent to saying they must be cooled down. In this thesis, neutral dipolar molecules are slowed down using their interactions with electric fields. The resulting slow molecules are used in a high-resolution spectroscopy experiment that demonstrates the advantage of cold molecules over warm ones. In later experiments, slow molecules are brought to a standstill and are trapped, both in a new electrostatic trap and, more notably, in an electrodynamic trap for ground-state molecules.

#### 1.1.1 Temperature

When discussing cold molecules, the notion of temperature is the first thing that needs to be examined. The meaning of the word temperature in every day life seems rather unambiguous. It is defined as the ‘degree of hotness or coldness measured on a definite scale’ [1]. In science, the concept of temperature is not always as straightforward. It can be defined in several ways and is often used



in a manner that is not strictly correct. The difficulty lies in the fact that a temperature can only be defined for a system that is in thermal equilibrium. In that case, the total energy is distributed over the ensemble of particles according to the Maxwell-Boltzmann distribution:

$$n(E) \propto e^{-E/kT}, \quad (1.1)$$

with  $n$  the number of particles with energy  $E$ ,  $T$  the temperature and  $k$  the Boltzmann constant. This allows, for instance, for the definition of a rotational or vibrational temperature. For kinetic energy, equation 1.1 can be written as a speed distribution (in all three dimensions):

$$F(v) \propto v^2 e^{-mv^2/2kT}, \quad (1.2)$$

with  $F(v)$  the speed distribution<sup>1</sup>,  $m$  the mass and  $v$  the speed of the particles. A low temperature is now characterized by both a small mean velocity and a narrow velocity distribution. The temperature of a packet of particles can be found by either determining how the particles are distributed over their internal energy states or by determining how they are distributed over their velocity states. In a fully thermalized sample of particles, both temperatures must be the same. If the sample is not in thermal equilibrium, they can be different and one cannot even speak of a temperature in this case. Nevertheless, physicists often choose to assign a temperature anyway. If the lack of thermalization is ignored and a packet's velocity distribution is fit to equation 1.2, a measure for the temperature will result. Oddly enough, this means that the 'temperature' can now be different in different directions.

Studying molecules in the low-temperature regime offers fascinating possibilities for several fields of research. Using cold molecules can significantly increase the resolution in spectroscopy experiments. Chapter 3 of this thesis illustrates this concept by showing spectroscopic measurements as a function of the velocity of a molecular beam of ammonia. Cold molecules are also needed for the study of cold collisions. Cold collisions are expected to boast new and intriguing phenomena that are absent in warm collisions. Furthermore, if a packet of molecules is made cold enough, with high enough density, an entirely new state of matter can be observed, the so-called Bose-Einstein condensate (BEC).

### 1.1.2 High-resolution spectroscopy

Ultimately, the resolution achievable in any spectroscopic experiment is limited by the interaction time of the investigated particles with the radiation field. The interaction time is determined by the limited size of the interaction region

---

<sup>1</sup>the average number of molecules per unit of volume with a speed  $v = |\vec{v}|$  between  $v$  and  $v + dv$

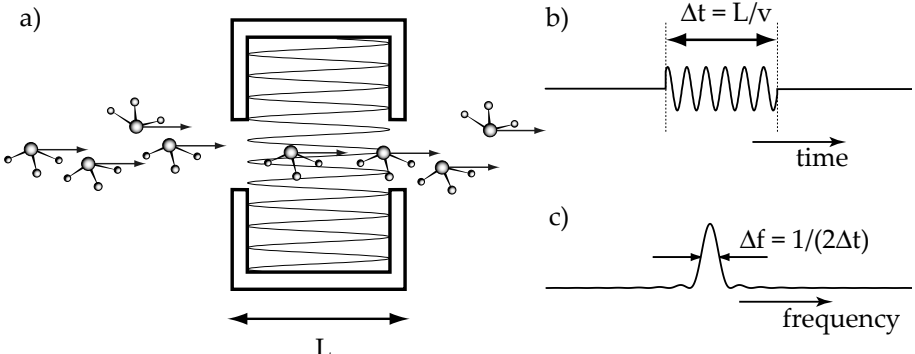
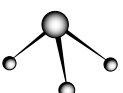


Figure 1.1: The concept of transit-time broadening.

in combination with the non-zero velocity of the examined particles. This is illustrated by figure 1.1(a), where a group of molecules is seen to traverse a microwave cavity of length  $L$ . As a result, the molecules see a radiation pattern such as shown in figure 1.1(b). The radiation is only experienced during a time  $\Delta t = L/v$ . The Fourier transform of this radiation pattern is shown in figure 1.1(c). The molecules experience a radiation pulse with a linewidth that is inversely proportional to the interaction time. This results in so-called transit-time broadening, which can only be reduced by increasing the interaction time. Obviously, the only two ways to accomplish this are either to increase the size of the interaction region or to decelerate the particles. To prevent broadening effects due to the different velocities of different particles, a small velocity spread is necessary as well. Performing spectroscopy on cold molecules should therefore tremendously improve the attainable resolution.

High-resolution spectroscopy (HRS) has applications in various fields of research. For one, it allows for exact knowledge of the energy structure of atoms and molecules, leading to such results as the highly accurate measurements of physical constants like the Rydberg constant and the  $1S$  Lamb shift [2–5]. Since frequencies can be measured with by far the highest accuracy ( $\sim 10^{-15}$ ), HRS can also be used for testing of various other fundamental theories. For instance, spectroscopic experiments are performed on molecules such as YbF [6] and PbO [7] to look for a possible electric dipole moment of the electron (EDM), which would be an indication for violation of time reversal symmetry. Violation of parity is investigated with spectroscopy as well, by measuring transitions in chiral molecules [8–11].

High precision spectroscopic measurements are also undertaken in search for a possible time variation of the fundamental constants [12, 13]. One such constant is the fine structure constant  $\alpha$ . Recent astrophysical data [14] suggest that  $\alpha$  has changed by 1 part in  $10^5$  over the age of the universe, corresponding



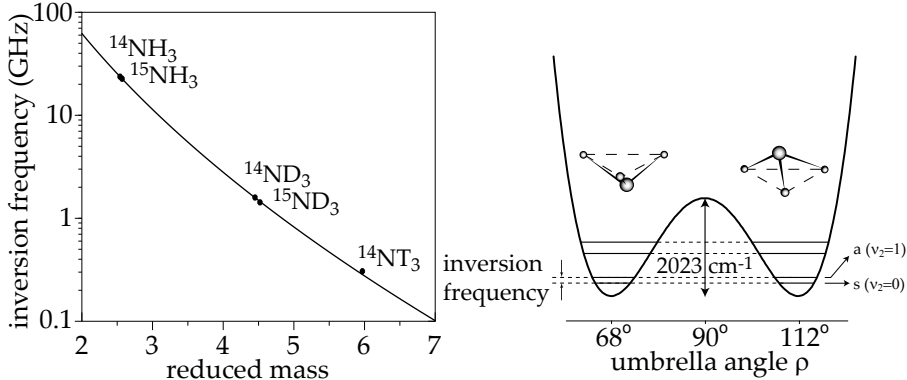


Figure 1.2: The inversion frequency of ammonia as a function of the reduced mass. On the right-hand side, the potential energy of ammonia as a function of the umbrella angle  $\rho$  is shown.

to a change of  $10^{-15}/\text{year}$  when assuming a cosmological model with a linear expansion. If confirmed, this will give very valuable insights into theories that go beyond the Standard Model. Therefore, there is a large interest in independent tests that corroborate these results [15, 16]. Various laboratory tests are being performed using clocks based on atomic transitions, which are mainly sensitive to the time variation of  $\alpha$ . For these same reasons, spectroscopy was recently performed on Stark-decelerated OH radicals [17]. Comparison of laboratory values to astrophysical data should be able to constrain  $\Delta\alpha/\alpha$  with a sensitivity of 1 ppm over the last  $10^{10}$  years.

If  $\Delta\alpha/\alpha$  varies over time, other constants are expected to vary over time as well, such as for instance the ratio of the electron-to-proton mass ( $m_e/m_p$ ) [18, 19]. Quite recently, indications were found that this time variation really does exist [20]. Spectroscopic lines of  $\text{H}_2$ , the most abundant molecule in the universe, were observed in two quasar absorption systems at a distance of  $12 \cdot 10^9$  lightyears [21]. The same lines were measured in the laboratory with unprecedented accuracy. Comparing these two sets of data with an improved calculation of the  $K_i$  coefficients, indicating the dependence of each line on the  $m_e/m_p$  ratio, resulted in a fractional change of this ratio of  $2.0 \pm 0.6 \cdot 10^{-5}$  in the last 12 billion years. Whether the  $m_e/m_p$  ratio still changes today can only be investigated by pure laboratory measurements.

A good candidate for such measurements is ammonia, the molecule investigated in this thesis. The inversion mode of ammonia involves the tunneling of the hydrogen atoms via a planar configuration to the other side of the nitrogen atom (see the right-hand side of figure 1.2). Its frequency is very sensitive to the mass of the proton, which is illustrated by the decrease of the inversion frequency in the  $|J, K\rangle = |1, 1\rangle$  level of ammonia from 23.8 to 1.59 to

0.3 GHz when the hydrogen atoms are replaced by deuterium or by tritium atoms, respectively (see the left-hand side of figure 1.2). This dependence of the tunneling frequency on the proton mass implies that if the proton mass (or rather the ratio of the electron-to-proton mass) varies over time, the inversion frequency will also vary. Theoretically one expects the inversion frequency,  $\nu_i$ , to follow the formula

$$\nu_i = \frac{a_0}{\sqrt{\mu}} e^{-a_1 \cdot \sqrt{\mu}}, \quad (1.3)$$

with  $\mu$  the reduced mass of ammonia for the inversion motion and  $a_0$  and  $a_1$  constants [22, 23]. From the known frequencies of the inversion mode of the ammonia isotopomers (see chapter 2 and [22, 24]) we find  $a_0 = 68 \text{ GHz} \cdot u^{1/2}$  and  $a_1 = 4.7 u^{-1/2}$ . From this we can determine the sensitivity of the inversion frequency to changes in the electron-to-proton mass ratio  $m_e/m_p$ . When  $m_e/m_p$  changes by  $\Delta(m_e/m_p)$  and the neutron mass changes by the same amount as the proton mass [25], the reduced mass changes by  $\mu \cdot \Delta(m_e/m_p)$ . This changes the inversion frequency in ammonia by

$$\frac{\Delta\nu_i}{\nu_i} = -5.6 \frac{\Delta(m_e/m_p)}{m_e/m_p}. \quad (1.4)$$

By comparing the inversion frequency with a suitable frequency standard over an extended period of time, the time variation of  $m_e/m_p$ , or an upper limit thereof, can be determined. In chapters 2 and 3, the inversion frequencies of  $^{14}\text{ND}_3$  and  $^{15}\text{ND}_3$  are studied, using both a supersonic beam (chapter 2), and a Stark-decelerated beam (chapter 3, only  $^{15}\text{ND}_3$ ).

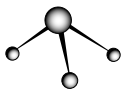
### 1.1.3 Cold collisions

The possibility to cool molecules allows for the study of cold collisions. Cold collisions show interesting features in that they display curious resonances and are affected by quantum tunneling [26, 27]. For instance, so-called Efimov states were recently detected for the first time in a cold (10 nK) sample of Cs atoms [28]. Named after their Russian inventor, Efimov states are three-body bound states that exist in regions<sup>1</sup> of the scattering length where two-body bound states are unstable. If the scattering length is negative, dimers are unstable and the stable trimers resonantly couple to three free atoms when an Efimov state intersects with the continuum threshold. At positive scattering lengths, the Efimov trimers can couple to a dimer and a free atom. The Efimov states were detected by the increase of the three-body loss rate at certain values of the scattering length due to these resonances [29].

Another example of resonances that can occur in cold molecular collisions is the Feshbach-like resonance that was observed in  $\text{Cs}_2$ , where at certain values

---

<sup>1</sup>These regions are sometimes called Borromean regions, after an Italian family whose coat of arms contains a set of three rings that fall apart if one is removed.



of the magnetic field  $\text{Cs}_4$  was formed due to inelastic collisions [30]. In electric fields, the inelastic-collision rate tends to be high at zero kinetic energy due to the dipole-dipole interaction. At low velocities, the molecules will spend more time close together, and as a result two dipoles will tend to align with respect to each other instead of with respect to the field, which leads to a change of the internal state [31]. This does not happen at larger distances, where the interaction of a dipolar molecule with the electric field is dominant.

In magnetic fields the dipole-dipole interaction, mainly responsible for high inelastic collision rates in electric fields, plays a much smaller role, as the interaction between magnetic dipoles is much smaller. Still, even in magnetic fields inelastic-collision rates can be high. Let's take the collision of a molecule with a He atom as an example. Even though the available energy in a collision with a He atom is insufficient to make a transition to higher rotational states, there can be a virtual coupling to these states nonetheless. Due to spin-rotation coupling, spin depolarization becomes possible in these excited states [32]. In collisions with molecules, which have higher binding energies than helium, the coupling needs no longer be virtual. As a result, the inelastic collision rate for molecule-molecule collisions is expected to become even higher than that for molecule-helium collisions [33]. The effect becomes less if the separation between rotational states becomes larger, or when the spin-rotation coupling is small.

#### 1.1.4 Quantum degeneracy

One more field of research that can benefit from the availability of cold molecules is the field of quantum degeneracy. In 1924, Louis de Broglie proposed that particles, apart from their expected particle-like behavior, also exhibit a wave-like behavior. This rather schizophrenic nature of matter is most clearly revealed at low temperatures. Each particle has a wavelength associated with it, which is given by:

$$\Lambda = \sqrt{\frac{2\pi\hbar^2}{mkT}}. \quad (1.5)$$

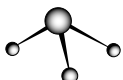
The lower the temperature of a gas becomes, the larger the de Broglie wavelength. In a trap, bosonic molecules are allowed to occupy the same trap states. Once the de Broglie wavelength becomes larger than the interparticle distance, all particles will move to the lowest energy trap state. When this happens, it becomes impossible to distinguish between different particles, and the entire ensemble behaves as a single quantum mechanical object. This process is called Bose-Einstein condensation. It was first demonstrated for atoms in 1995 [34–36], and has also been realized for homonuclear molecules recently [37–39]. Unlike atoms or homonuclear molecules, heteronuclear molecules have permanent electric dipole moments. Due to its anisotropy and long-range character, the dipole-dipole interaction is expected to influence

the dynamics of a BEC considerably. Depending on the way the dipoles are aligned, their interaction can be either attractive or repulsive. As a result, the aspect ratio of a BEC determines both the sign and the magnitude of the interactions [40]. The magnetic dipole-dipole interaction shares many features with the electric dipole-dipole interaction, but it is much weaker. Nevertheless, the first dipole-dipole interactions to be observed in a BEC were magnetic in nature [41].

In each of these areas of research, traps are either necessary, or they enhance the potential of the method considerably. Traps ensure a thermally isolated packet of molecules, with generally high densities. Both of these features are important in the study of cold collisions. If trap shapes can be easily varied, it becomes possible to study cold collisions as a function of collision energy. Chapter 4, for instance, discusses such a trap and its potential use in collision experiments. Traps are also essential for BEC experiments. No molecular BEC has been formed from pre-existing stable molecules yet. It will be shown that for this purpose, a very particular kind of trap is needed, that allows for the trapping of molecules in their ground state. The design, dynamics and experimental realization of such a trap are discussed in chapter 5 of this thesis. Finally, in high-resolution spectroscopy, interaction times can be made longest when the molecules are standing still on average, i.e., when they are trapped. As will become clear from the next section, traps generally make use of some kind of field, be it magnetic, electric or optical. There are several applications of high-resolution spectroscopy where a field can be an advantage. Where an applied field is an impediment, traps cannot be used. All in all, this amply justifies a closer consideration of traps.

## 1.2 Traps

In order to be called a trap, a system needs to meet two requirements. First, the force on the molecules needs to be zero in the center of the trap ( $\vec{F}(0) = 0$ ). Secondly, for small displacements the force has to restore the molecules towards the center ( $\nabla \cdot \vec{F} < 0$ ). To generate this force, the internal energy levels of the molecules need to change as a function of position (converting the two requirements to  $\nabla U(0) = 0$  and  $\nabla^2 U(0) > 0$ , using  $\vec{F} = -\nabla U$ , with  $U$  the potential energy of the molecule). Shifting the energy levels can be accomplished by allowing the molecules to interact with an external field. The extra term in the Hamiltonian can be evaluated using perturbation theory, and leads to mixing of the different states. Consequently, the energy levels shift. Molecules in states that shift upwards have less potential energy in low fields, and are therefore pushed towards regions of lower field. These molecules are called low-field seekers. Molecules in states that shift downwards in energy



will experience a force towards regions with higher fields and are called high-field seekers. A trap can now be formed by employing a field that is position dependent. What the trapping field should look like depends on the quantum state of the molecule. Generally, traps can be classified by whether they confine low- or high-field seekers. Both kinds of traps will be discussed in the following sections.

### 1.2.1 Traps for low-field seekers

To trap molecules in low-field-seeking states a field minimum is required. So far, two types of static fields, namely magnetic and electric have been used to trap low-field-seeking molecules. In the case of magnetic fields, the interaction of the field with the energy levels is called the Zeeman effect. Proposals to use a magnetic field to trap particles were made as early as the beginning of the 1960s [42, 43]. The first traps considered were mostly toroidal in nature and were used to trap neutrons [44]. After the onset of cooling techniques for atoms, various trapping geometries were considered to trap atoms [45–48]. Unlike the toroidal configuration, most of these traps have one central minimum of the magnetic field strength. Using generally available technology, these traps have a depth on the order of 100 mK, but they can be deeper when superconducting coils are used [49]. Traps that have a non-zero field in the center [47] are less deep, but have the advantage that they preclude so-called Majorana transitions. These transitions occur when two levels are degenerate. If this is the case, the particle may change states when crossing a region of zero field, which results in trap loss if the final state is untrapped. The best known trap with a non-zero field at the center is the Ioffe-Pritchard trap, invented by Ioffe for use with plasmas [50] and adapted for the use with neutral particles by Pritchard [45]. In 1985, atoms were magnetically trapped for the first time in the minimum of a quadrupolar field [51]. Trapping of molecules had to wait until cooling methods for molecules were further developed. This feat was finally accomplished in 1998, when a sample of CaH molecules was cooled by collisions with a cold He buffer gas and was subsequently confined in a magnetic field minimum [52].

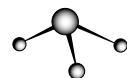
Electrostatic fields can also be used to trap low-field-seeking molecules. The change of internal energy levels due to interactions with electric fields is called the Stark effect. The first proposal to implement this Stark effect to trap neutral particles used a quadrupolar arrangement [53], but toroidal configurations were also considered [54]. As atoms lack an electric dipole moment, their interaction with electric fields is of the second order. It is therefore hardly surprising that electrostatic trapping was first demonstrated for molecules. As with magnetic traps, realization of these electrostatic traps depended on the development of appropriate cooling techniques. One cooling method also employing electric fields is the Stark deceleration method. This technique exploits the interaction of the molecules with time-varying electric fields to extract kinetic energy, resulting in a packet with an arbitrary velocity and a narrow velocity spread

(see [55] and section 3.2). The device that enables this kind of cooling, the Stark decelerator, has been used to load several different trapping geometries. The first was an electrostatic quadrupolar trap, which was used to trap ammonia molecules [56]. Later, OH radicals were trapped in a similar trap [57]. The next electrostatic configuration used as a trap was toroidal; a packet of ammonia molecules was confined in a ring-shaped hexapole [58] and was still observed after 50 round trips [59]. Illustrating the versatility of electrostatic traps, a single trapping geometry was used recently to create a quadrupolar and a hexapolar trapping field, as well as a double-well and a donut-shaped field. The design of this trap along with a discussion of the experimental results is presented in detail in chapter 4 of this thesis.

So far, all the traps discussed have been fully closed and need to be opened to reload them. However, opening allows the molecules that were already stored to leave the trap. In some specific cases though, it is possible to find a one-way path into a trap; this has been proposed for reloading of a magnetic trap for NH radicals. The packet is loaded in an excited state that is sensitive to electric fields only, and is subsequently transferred to the ground state, that has a large Zeeman, but no Stark effect [60]. If two consecutive packets do not need to be spatially overlapped, then reloading also becomes possible. This was shown recently for two packets of ammonia molecules that were consecutively loaded into a toroidal trap consisting of two half rings [61]. A different way of reloading a trap is by devising a trap with a hole in it [62]. As this trap is fundamentally unstable, molecules will leak out of the trap through the hole. The trap needs to be reloaded continuously, which is done by guiding the coldest molecules that exit an effusive source with a bent quadrupole [63]. The trap density reaches an equilibrium when the filling rate equals the leak rate. Note that the minima of all traps discussed so far were at zero electric field. Electric counterparts of the magnetic Ioffe-Pritchard trap have been proposed [64–66], but have not been demonstrated as yet.

### 1.2.2 Importance of high-field seekers

The traps discussed in the previous section are capable of confining molecules in low-field-seeking states only. However, for many applications of cold molecules, either molecules in the ground state or heavy molecules are required, and these are always high-field seeking. After calculating the energy levels of a molecule, (small) disturbances, such as those that are caused by the interaction of the molecule with an electric field, can be incorporated into the system by perturbation theory. From this theory, it follows that the new energy levels are linear combinations of the undisturbed energy levels, and that the lowest level always moves down with increasing disturbance [67]. Ground-state molecules are therefore always high-field seeking. Heavy molecules have primarily high-field-seeking states due to their small rotational constants. The rotational constant is inversely proportional to the moment of inertia, which becomes



larger with larger mass [68]. The smaller this constant, the lower the field at which mixing with higher rotational levels has to be taken into account. Due to this mixing, eventually all lower lying energy levels will go down in energy with increasing field. The heavier the molecule, the lower the field at which this happens, until the molecule becomes high-field seeking for all practical purposes. For comparison, see for instance figure 1.3, where the Stark effect of deuterated ammonia, YbF, and benzonitrile is given for selected rotational states. Deuterated ammonia is a relatively light molecule (20 amu) with a rotational constant of  $5.1 \text{ cm}^{-1}$  [69], and as a result, several of the hyperfine levels in the  $|J, K\rangle = |1, 1\rangle$  state are low-field seeking. Due to the mass of the Yb atom, YbF is rather heavy (193 amu) and has a rotational constant of  $0.24 \text{ cm}^{-1}$  [70]. Most of the displayed levels are high-field seeking. Finally, benzonitrile is a rather large molecule with a mass of 103 amu and rotational constants  $A = 0.19$ ,  $B = 0.051$ , and  $C = 0.040 \text{ cm}^{-1}$  [71]. None of the levels shown are low-field seeking in any practical region of the electric field strength.

Due to the broad range of research fields for which cold molecules are interesting, the reasons for investigating either ground-state or heavy molecules are diverse, only a few of which will be mentioned here in more detail.

### Evaporative cooling

To date, the quantum degeneracy of atoms has only been achieved through the (very) successful technique of evaporative cooling. In this technique, the hottest atoms in a sample are allowed to leave the trapping region, taking with them more than the average amount of kinetic energy. Simultaneously, thermalizing collisions between the remaining atoms ensure the decrease of their average kinetic energy. Only elastic collisions contribute to thermalization; inelastic collisions lead to trap loss and heating of the trapped ensemble. The ratio of elastic to inelastic collisions ( $\gamma$ ) determines the success of this method. For molecules in any state but the ground state, the value of  $\gamma$  is expected to be unfavorable for evaporative cooling (see section 1.1.3). For instance, for  $^{14}\text{ND}_3$  in the upper component of the  $|J, K\rangle = |1, 1\rangle$  inversion doublet, evaporative cooling is expected to be impossible for all values of the kinetic energy and the electric field. If the electric field is higher than  $10 \text{ kV/cm}$ , it might be possible for  $^{15}\text{ND}_3$ , but only if the kinetic energy is less than  $100 \mu\text{K}$  [72]. In the ground state, however, transitions to other states are impossible as long as the kinetic energy does not exceed the energy difference with the excited state, and therefore evaporative cooling should be viable.

### Precision tests on heavy molecules

**Biomolecules** Biomolecules are organic molecules that naturally occur in living organisms. They are heavy, as they generally consist of many atoms. They are often referred to as ‘the building blocks of life’, which immediately indi-

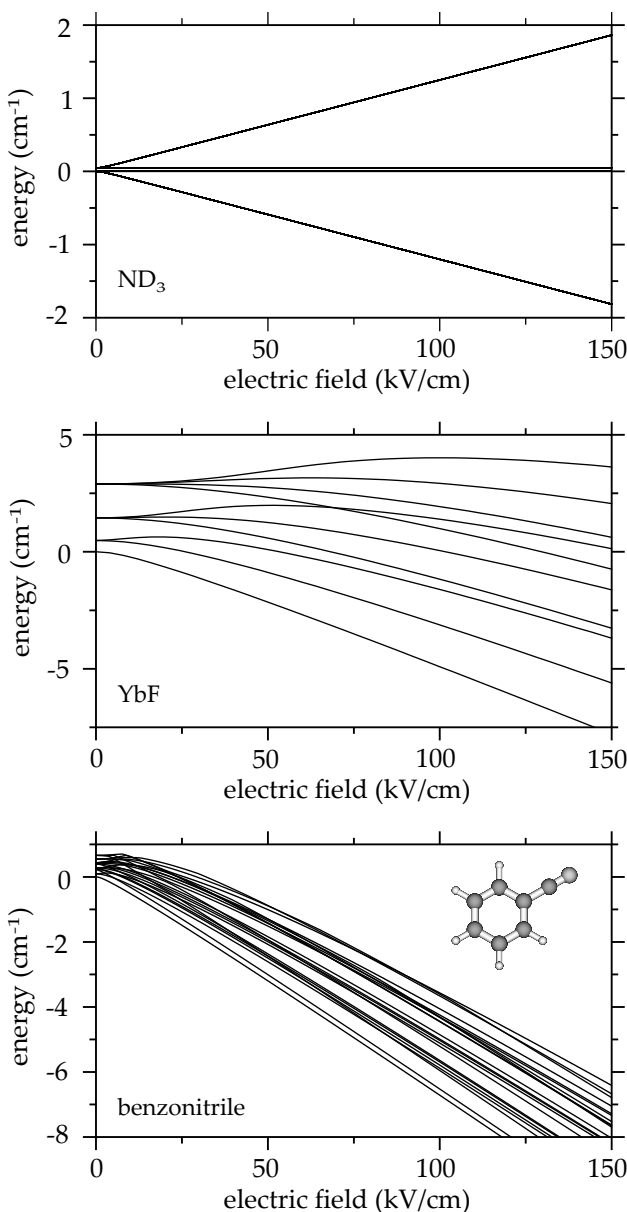
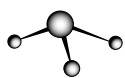


Figure 1.3: The Stark effect of ND<sub>3</sub>, YbF and benzonitrile.



cates their importance. Although over the years the knowledge of biology on a molecular level has grown, there are still some fundamental aspects that are only poorly, if at all, understood. Biological systems are immensely complex, not only due to the size and complicated structures of the molecules involved, but also because of the interaction of these molecules with their environment. There are two ways of approaching this problem. One is to directly look at a system exactly as it occurs in nature, often by studying macromolecular structures in solution. Although this method has turned out to be a successful one, it has the disadvantage that much of the spectroscopic information washes out. There are many different forms in which a molecule can exist, such as different isomers<sup>1</sup> and tautomers<sup>2</sup>, which often leads to line broadening. Additionally, it is impossible to differentiate between intrinsical molecular or intramolecular properties and features that are influenced or even dictated by the environment. This directly indicates the merits of the second method, which proposes to study these complex systems under isolated or defined conditions, for instance in the gas phase. Environmental effects can clearly be ruled out in this case, or can even be seen to increase gradually, if complexes of increasing sizes are investigated. In the gas phase, many different conformers<sup>3</sup> can be present [73]. It is possible to distinguish between conformers, for instance by using double-resonance techniques. Most conformers differ in dipole moment, which could give rise to another promising technique to differentiate between them. Their differing Stark effects and, consequently, their differing behaviours in an inhomogeneous electric field could lead to a spatial or temporal separation of these conformers when using either an AG guide or an AG-decelerator (see section 1.2.3). In this way, it should be possible to generate pure samples of only one conformer. Admittedly, the isomers that can be studied in the gas phase are not necessarily the ones that are important in biology. Still, to gain an understanding of why nature picked the particular isomers that it did, all of them need to be examined. Furthermore, detailed spectroscopic information of any of the isomers allows for testing and calibration of theory. Theory can then be extended to describe systems that are not (yet) experimentally accessible [74]. Of course, biomolecules, with their modular behavior and complex structures, are interesting for chemistry as well. The possibility to study these molecules on the timescales made available by traps offers exciting prospects of increasing our knowledge of their structure and interactions.

**Time reversal symmetry** Heavy molecules can also simply consist of heavy atoms. These type of molecules are generally important in fundamental physics where relativistic effects play a role. The heavier the nucleus of an atom, the

---

<sup>1</sup>Isomers are molecules with the same chemical formula, but with different arrangement of the atoms.

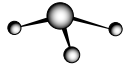
<sup>2</sup>A tautomer is one of two or more isomers that interchange relatively easily in equilibrium.

<sup>3</sup>Conformers are isomers that can interconvert by chemical bond rotations.

faster the electrons move, and consequently, the larger the relativistic effects. This is true, for instance, in the search for the electric dipole moment of the electron (EDM). The existence of an EDM would mean a violation of parity and of time reversal symmetry. Parity violation has been shown to exist already in the presence of weak interactions [75]. Time reversal symmetry has only been found in the neutral kaon so far. In the standard model, the expected value for the EDM is quite small (less than  $10^{-38} e \text{ cm}$ ), but other theories predict values that are within experimental reach. The EDM cannot be measured on the electron directly; to do so, the electron would have to be put into an electric field, in which case it would immediately fly into the electrodes. An alternative would be to use an unpaired electron in an atom (in pairs the EDM will cancel). If the electron has an EDM, it can be argued that the energy levels of the atom shift in an electric field, depending on the relative orientation of the atom in the field. Classically speaking, this is not the case. All the other charges within the atom shield the electron, by generating their own electric field that exactly counters the external field. In effect, the electron does not ‘feel’ the electric field. This is called Schiff’s theorem [76]. Relativistically, the equilibrium position of the electron is not only determined by the electric fields, but also by the motional magnetic field generated by the electron as it passes the nucleus. As a result, the net electric field can be non-zero, and effectively can even be much larger than the laboratory electric field [77]. The heavier the atom, the larger the relativistic effects, and therefore the larger this enhancement factor.

To be able to measure any energy splittings, the internal electric field of the atoms needs to be oriented. This is more easily done in molecules, where the internal electric field is linked to the molecular axis, which can be oriented with an external electric field. Good candidates for EDM measurements are therefore diatomic molecules of which one of the constituents is a heavy atom, like for instance YbF [6] or PbO [7].

**Parity violation** Heavy molecules also play a role in a different kind of symmetry breaking; they could be particularly important for measuring parity violation effects in molecules. Parity violation was proven to exist already in the 1950s, by the asymmetry of the nuclear  $\beta$  decay in  $^{60}\text{Co}$  nuclei [75]. In a  $\beta$  decay process, a neutron is converted into a proton, while emitting an electron and an antineutrino. At a deeper level, the neutron is converted by changing a down quark into an up quark and emitting a  $W^-$  boson, one of the particles that mediates the weak interaction. The  $W^-$  then decays into the electron and antineutrino. As the emitted electrons in the  $^{60}\text{Co}$  nuclei (with oriented spins) show a preference for one certain direction, this is evidence for parity violation. Parity violation has also been shown to exist in atoms [78, 79]. Here, it is manifested by a preference for one orientation of space, for instance by preferably absorbing or emitting either left- or right-circularly polarized light.



For molecules, no experimental evidence has been found as yet. It is looked for by comparing the transition energy of the two forms of a chiral molecule, that is, two molecules that are each other's mirror image (enantiomers) [80]. Apart from exploring a different region of the electroweak interaction, chiral molecules are particularly interesting because of the mysterious homochirality existing in living organisms. For reasons yet unknown, almost all building blocks of proteins, the amino-acids, are L-amino-acids, whereas almost all sugars used in DNA and RNA are D-sugars<sup>1</sup>. If and how the very small effect of parity violation can be responsible for this puzzling preference is unclear [81–83], but intriguing nonetheless. However, as these effects scale with the fifth power of the number of protons ( $Z$ ) in the nucleus of the heaviest atom, it is clear that heavy molecules are essential for this kind of research.

### 1.2.3 Traps for high-field seekers

#### Earnshaw's theorem

From the previous discussion, it follows that it is important to extend the aforementioned trapping techniques to include high-field seekers. In accordance with the field minimum that is used to trap low-field seekers, ideally, a trap for high-field seekers would consist of a field maximum in three dimensions. Unfortunately, Maxwell's equations do not allow for such a maximum in free space using static electric or magnetic fields (see the Appendix). This is usually said to be a consequence of Earnshaw's theorem.

In 1842, Samuel Earnshaw published a paper with the at first glance somewhat puzzling title '*On the nature of the molecular forces which regulate the constitution of the luminiferous ether*' [84]. Around that time, it was generally believed that light needed a medium to propagate through. This medium was dubbed the luminiferous ether, or the light-bearing ether. Earnshaw was trying to formulate some general rules for the nature of the force that would enable the ether to be light-bearing. As such, he envisioned a space filled up with particles that could vibrate in any direction when disturbed (the capability to vibrate constitutes the light-bearing property). He finds that if the force between the particles is inversely proportional to the square root of the distance between two particles ( $\vec{F} \propto \hat{r}/r^2$ ), a small displacement of one of the particles will always lead to a continued translation of this particle in at least one of the three directions. In other words, if one of the particles is moved a little bit, it will start to vibrate (constituting stability) in at most two directions, but in at least one direction, it will move off. As the force between charged particles is inversely proportional to  $r^2$ , and any field can always be described as originating from a collection of charges, this means it is impossible to trap charged particles using static fields. One of the more usual formulations of Earnshaw's theorem is that 'a collection of point charges cannot be maintained

---

<sup>1</sup>Here L and D refer to specific spatial conformations of these chiral molecules.

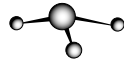
in a stable equilibrium by electrostatic interaction alone'. This can quite easily be seen from the requirement for trapping that  $\nabla \cdot \vec{F} < 0$ , as  $\nabla \cdot \vec{F}$  for any inverse-square law force is equal to zero.

Earnshaw's theorem posed quite a problem in his time, and in a way, heralded an end to classical theory as the all-encompassing theory it was believed to be until then [85]. The difficulty lay in the stability of the atom. If the charged particles within an atom were supposed to be moving, it was unclear how this could be stable, since Maxwell had shown that an accelerating charge radiates energy. If the charges were not moving, Earnshaw showed that the atom could not be stable either. Eventually, the problem was solved by quantum mechanics. Clearly, though, the atom lies outside the realm of Earnshaw's theorem. Nevertheless, there seems to be a variation on Earnshaw's theorem at work, since ground-state molecules cannot be trapped using static fields any better than charged particles. Apparently, some kind of motion or time dependence is necessary. Fortunately, these two notions provide us with several methods to trap high-field-seeking molecules despite 'Earnshaw's theorem', as can be seen in the following sections.

### Wire traps

Although Maxwell and Earnshaw do not allow for a maximum field strength in free space, of course a maximum does exist at a charge or current. To prevent particles from crashing into the electrodes, circular motion can be used. If a potential energy of  $V = \frac{L^2}{2mr^2} - \frac{\alpha}{r^n}$  is assumed, with  $V_{cf} = \frac{L^2}{2mr^2}$  the centrifugal potential, it can be seen that a minimum in the potential only occurs if  $n < 2$ . Stable trapping is therefore only possible if the force ( $F = -\frac{dV}{dt}$ ) that attracts molecules to the center of the trap does not have a stronger dependence on  $r$  than  $r^{-3}$ . In 1960, this centrifugal barrier was utilized in a charged wire focuser to focus high-field-seeking NH<sub>3</sub> molecules. The focuser consisted of a coaxial line with a voltage applied between the center conductor and the outside conductor [86]. The molecules were kept from the central wire by the centrifugal barrier. Along the wire, the motion was free, but in the plane perpendicular to the wire, the coaxial line served as a guide for high-field seekers. Better signals were obtained later on with a similar system [87]. In general, this concept works for any molecule with a linear Stark effect in the applied field [88,89], but not for polarizable particles, for which the force is proportional to  $r^{-3}$  [90]. Proposals have been made, though, to alternate the sign of the voltage and to use the resulting effective potential to trap polarizable atoms [91]. Particles with a magnetic moment can be trapped in much the same way as polar molecules by using a current-carrying wire, instead of a charged wire [42,90,92].

Several proposals have been made to adapt wire focusers to three-dimensional wire traps. An obvious idea is to bend the wire in a ring [93]. Others are to shape the outer electrode [88,89,92,94], or to form the wire into a bend and use gravity to trap the particles in the third dimension [88,92]. None of



these traps have been realized so far, though.

### Optical dipole traps and microwave traps

Another way of getting around ‘Earnshaw’s theorem’ is to use laser fields instead of static fields. If the laser frequency is far enough away from any transition frequency, the interaction of the atoms or molecules with the light will cause shifts in the energy levels, similar to the shifts caused by static fields. The difference is that this AC Stark shift is not only dependent on the field-strength, but also on the frequency. If the laser frequency is tuned below the transition frequency (red-detuned), the ground state will shift downwards (high-field seeking), but if the laser is tuned above the transition frequency (blue-detuned), the ground state will shift upwards (low-field seeking). In the case of low saturation, the atom or molecule will spend most of its time in the ground state, and therefore only the ground-state potential is relevant for trapping. Consequently, a red-detuned trap consists of a maximum of laser intensity, and a blue-detuned trap is generally formed by surrounding a light-free region with repulsive laser light. The closer the laser is to the resonance, the larger the shift, but also the higher the optical excitation rate. An optical dipole trap is therefore always far-detuned from resonance and uses higher laser intensity to compensate for the loss in trap depth [95].

Red-detuned traps are easiest to make, as it basically only takes a focused laser. Not surprisingly, it was in this kind of trap that both atoms [96] and molecules [97] were optically confined for the first time. This trap has rather weak confinement along the propagation axis, though. A much tighter confinement can be gained by retroreflecting the beam upon itself, and thereby creating a standing wave. A tight optical trap can also be created by crossing two beams. The latter option has the additional advantage that the trap becomes isotropic. Blue-detuned traps are a bit more difficult. To surround a region with laser light, so-called light sheets can be used, that are formed by strong elliptical focusing of a laser beam. Alternatively, a hollow laser beam, which is confining in two dimensions, can be combined with two additional laser beams, that are orthogonally crossed with the hollow beam to generate confinement in the third dimension. A third option is to use evanescent waves, produced by total internal reflection on the vacuum side of a vacuum-dielectric interface. These evanescent waves are almost ideal mirrors for atoms, and as such, can be used to trap atoms as well.

The two most important disadvantages of optical dipole traps are their limited volume and trap depth. One way of trying to overcome this problem is to confine particles in the amplitude maximum of a standing microwave. This method is very similar to optical dipole trapping. One of the main advantages of microwave traps is that the spontaneous-emission rates are very low. This makes it possible to get much closer to the resonance frequency, which increases the trap depth considerably. In addition, amplifiers are available for large

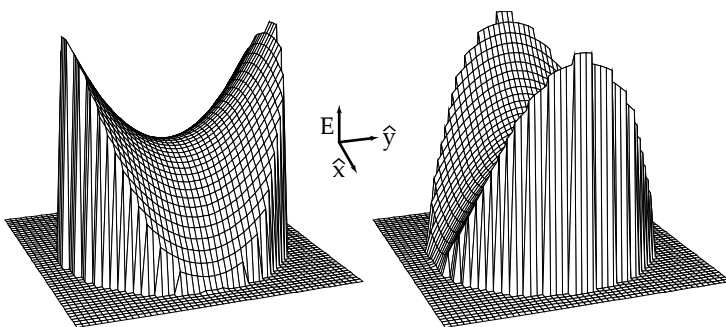
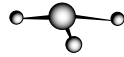


Figure 1.4: Two saddle-point fields

frequency regions in the microwave range that make it possible to have much higher output power in the microwave than in the optical range. Moreover, the volume of a microwave trap is directly related to the frequency, and as such, is much larger than that of an optical trap. For instance, in a trap for NH<sub>3</sub> that uses radiation close to the inversion frequency of the |J, K⟩ = |1, 1⟩ state (23.8 GHz) in the vibrational and electronical ground state, the volume is around 0.1 cm<sup>3</sup> [98] (compared to around 10<sup>-5</sup> cm<sup>3</sup> for optical dipole traps). In 1994, the first microwave trap was demonstrated for Cs atoms, using a spherical microwave cavity [99], and recently a microwave trap was proposed for polar molecules as well [100].

### AC traps

A different method to confine high-field-seeking molecules is AC trapping, which is the method pursued in this thesis (chapter 5). This method employs fields that have a field strength that is shaped like a saddle point, i.e., it has both a minimum and a maximum in at least one dimension. The third dimension has either a maximum or a minimum. A trap for high-field-seeking molecules can be formed by switching between this field, and a field that exchanges each minimum for a maximum, and vice versa (see figure 1.4). In that case, a molecule alternately experiences a focusing and a defocusing force in each dimension. Ideally, the fields are shaped such that the difference between these two forces at any position is in sign only, but not in magnitude. Consequently, if the molecules were to stand still, the force on the molecules would average out over a full period of the switching cycle. However, due to these said focusing and defocusing forces, the molecules move. After half a period of focusing, any molecule will necessarily have moved towards the center of the trap (the position of the saddle point). When the defocusing starts, the molecule will therefore be closer to the center of the trap. Similarly, the defocusing force moves the molecule away from the center, so that it is further away from the



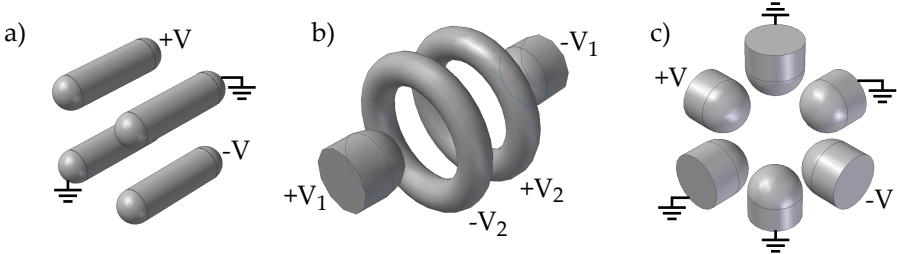


Figure 1.5: Three types of AC trap: a) a linear AC trap. b) a cylindrical AC trap. c) a three-phase AC trap.

center when the focusing starts. Consequently, although somewhat counterintuitive, the molecule is closer to the center of the trap during defocusing than during focusing. As the force on the molecules increases with distance from the center, the focusing force experienced by the molecules is larger than the defocusing force. As a result, instead of averaging out, a small net focusing force remains. The fast motion of the molecules in phase with the switching frequency is called micromotion. It is this motion that allows AC trapping to function and that accounts for the alternative term ‘dynamic trapping’, that is sometimes used.

When the previously explained principle is applied in two dimensions, it is called alternate gradient focusing (AG focusing). AG focusing was proposed as early as 1952, for use in particle accelerators [101, 102]. Later, in 1966, it was realized that the same principle can be applied to the focusing of molecular beams [103]. Soon afterwards, this was experimentally proven for a beam of ammonia [104, 105]. Recently, AG focusing was used for transversal focusing in a decelerator for molecules in high-field-seeking states (an AG decelerator) [106–108], and in a guide for high-field-seeking molecules [63].

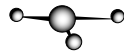
In the meantime, in 1985, a proposal had been made to use AG focusing in three dimensions for the trapping of hydrogen in high-field-seeking states, using magnetic fields [109]. In 1991, this trap was experimentally realized for Cs atoms [110]. The trap utilized a magnetic quadrupolar field, that was generated by two pairs of coils run at the 60 Hz mains frequency. This resulted in a trap with a depth of about  $12 \mu\text{K}$ . Shortly afterwards, several proposals for electric AC traps were published [111–114]. The different traps can be divided into three categories, schematically shown in figure 1.5 (see also section 5.3). The linear AC trap (figure 1.5(a)) consists of four rods, with a positive and negative voltage applied to two opposing rods, with the other two grounded. For trapping, the voltages on the two sets of opposing rods need to be exchanged. This trap is in fact an AG focuser, as dynamic confinement only occurs in the transversal plane. Longitudinally, the molecules are confined in an electric field strength maximum. The cylindrical AC trap is, as the name suggest, cylindri-

cally symmetric. Voltages are applied as shown in figure 1.5(b). Trapping takes place by appropriately changing the values of  $V_1$  and  $V_2$  (see section 5.3). The third category of AC traps consists of three-phase AC traps (see figure 1.5(c)). These traps are symmetric in three mutually perpendicular planes. A positive and negative voltage are applied to one of the three sets of opposing rods, while the other two sets are grounded. The voltages are interchanged between the three sets to start trapping.

In chapter 5, the first three-dimensional trapping of ground-state molecules in an AC trap is presented. The electrodynamic trap that is used has cylindrical symmetry and combines an oscillating hexapole field with a dipole field, as proposed by Peik [114]. The trap has a depth in the mK range and is used to trap high-field-seeking  $\text{ND}_3$  molecules. More recently, two linear electric AC traps were also realized. First, a linear AC trap on a chip was demonstrated for atoms [115, 116]. Later, a linear AC trap for molecules was used to trap Stark-decelerated ammonia molecules [117].

#### 1.2.4 This thesis

In this thesis, we show some of the advantages of cold (Stark-decelerated) molecules over warm ones and we demonstrate an AC trap for high-field-seeking molecules. In both experiments, the primary molecule that is used is deuterated ammonia. In chapter 2, both  $^{14}\text{ND}_3$  and  $^{15}\text{ND}_3$  are studied in some detail. Specifically, we show a spectroscopic experiment on the pure inversion transition of the  $|J, K\rangle = |1, 1\rangle$  state. Incidentally, this transition transfers molecules from a low-field-seeking to the high-field-seeking ground state of para-ammonia, which is exploited later on in the experiments on AC trapping of high-field seekers. Using this same transition, in chapter 3 we illustrate the advantages of Stark deceleration by demonstrating the improved resolution that can be gained by performing spectroscopy on a slow beam of molecules. This was the main motivation for the development of Stark deceleration and is experimentally demonstrated here for the first time. In the second part of this thesis, in chapters 4 and 5, one single electrode geometry is used to form different kinds of traps. In chapter 4, several traps for low-field-seeking molecules are demonstrated, by varying the voltages applied to the electrodes. The four main shapes that are shown are a quadrupolar, hexapolar, donut-shaped and double-well trap. Apart from illustrating the versatility of electrostatic traps, in this chapter we also discuss the specific merits of the double-well trap, which is particularly well suited for the study of collisions at well-defined kinetic energies. In the last chapter, we use the same electrode geometry to trap both low- and high-field-seeking molecules in an AC trap. This is the first demonstration of an electric AC trap, and the first time an AC trap was demonstrated for molecules. The features of the trap are studied in great detail, both experimentally and theoretically and some comparison is made to other kinds of AC trap.





# Chapter 2

## The hyperfine structure of ND<sub>3</sub>

### 2.1 Introduction

Ranging from dubious to beneficial, the applications of ammonia are rather diverse. For instance, ammonia played a key role in the First World War, because of its use in the production of explosives. In 1909, it had been discovered how to produce ammonia on an industrial scale by Fritz Haber and Carl Bosch. In the Haber-Bosch process, the requisite nitrogen is collected from the air, instead of from natural deposits, which allowed Germany to produce its explosives independently. Fritz Haber received the Nobel prize in chemistry for his work on ammonia in 1918, mainly due to one of the more beneficial applications of ammonia: the production of fertilizers that could help solve the world food problem. Incidentally, from 1912 to 1933, Fritz Haber directed the institute that housed some of the experiments shown in chapter 3 (trace c of figure 3.6 on page 58) and all experiments shown in chapters 4 and 5. This institute, called the “Kaiser-Wilhelm-Institut für Physikalische Chemie und Elektrochemie” during Haber’s reign, was renamed after its first director in 1953 to the Fritz-Haber-Institut.

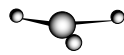
Ammonia takes a first place in many areas of research. Ammonia was the first molecule to be observed with microwave spectroscopy [118], and was the molecule on which the first maser was demonstrated [119, 120]. The first polyatomic molecule to be observed in space was ammonia [121] and its deuterated sibling, ND<sub>3</sub>, was the first triply deuterated molecule to be observed in the

---

Adapted from:

*Hyperfine structure of ND<sub>3</sub>*

Jacqueline van Veldhoven, Rienk T. Jongma, Boris Sartakov, Waldo A. Bongers, and Gerard Meijer, *Phys. Rev. A* **66**, 032501 (2002)



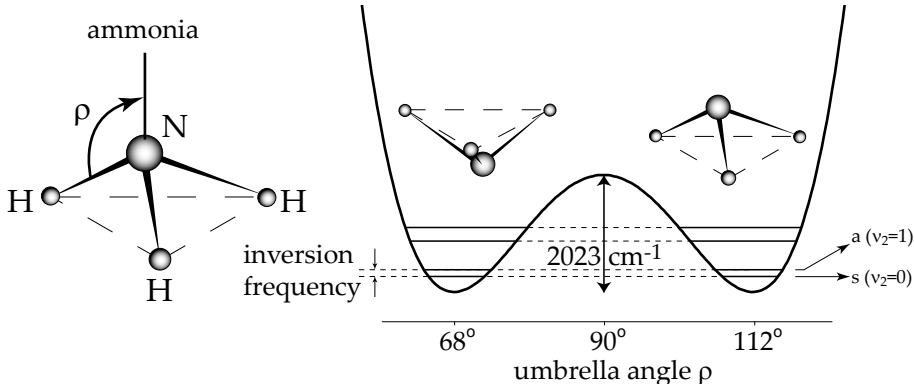


Figure 2.1: The ammonia molecule, consisting of one nitrogen atom and three hydrogen atoms. On the right-hand side, the potential energy of ammonia as a function of the umbrella angle  $\rho$  is shown, along with the two vibrational levels that are split due to the potential barrier.

interstellar medium. Ammonia has proven to be invaluable to the study of interstellar space ever since [122].

Apart from the historical and physical interest of ammonia already discussed, deuterated ammonia in particular has several properties that make it a prime test molecule for all the experiments performed in this thesis. Due to its relatively large dipole moment-to-mass ratio ( $\mu \approx 1.5$  D and  $m = 20$  amu for <sup>14</sup>ND<sub>3</sub> and  $m = 21$  amu for <sup>15</sup>ND<sub>3</sub>), ND<sub>3</sub> can easily be manipulated using electric fields. In this thesis, this is used both to cool down a packet of molecules, which facilitates the high-resolution spectroscopy shown in chapter 3, and more directly in the trapping experiments shown later on in this thesis (chapters 4 and 5). In this chapter, we will take a closer look at ammonia itself, and at the transition used in the proof-of-principle spectroscopy experiment of chapter 3.

Ammonia is a pyramid-shaped molecule, consisting of one nitrogen atom and three hydrogen, or, in the deuterated case, three deuterium atoms (see the left-hand side of figure 2.1). The angle between the vertical axis passing through the nitrogen atom and one of the lines N-D (or N-H) is called the umbrella angle  $\rho$ . The potential energy of ammonia is lowest when  $\rho$  is around 68°, or 112° (see the right-hand side of figure 2.1). These two values correspond to two equivalent positions of the N atom, on either side of the hydrogen or deuterium plane. The barrier between these two positions is about 2023 cm<sup>-1</sup> high, as can be seen from the right-hand side of figure 2.1. As it is not infinitely high, the ammonia molecule can tunnel through the barrier, which leads to a splitting of all rovibrational levels that are lower in energy than the barrier. The two ensuing levels have opposite parity (symmetric and antisymmetric). They therefore repel one another when induced to mix by an electric field, as

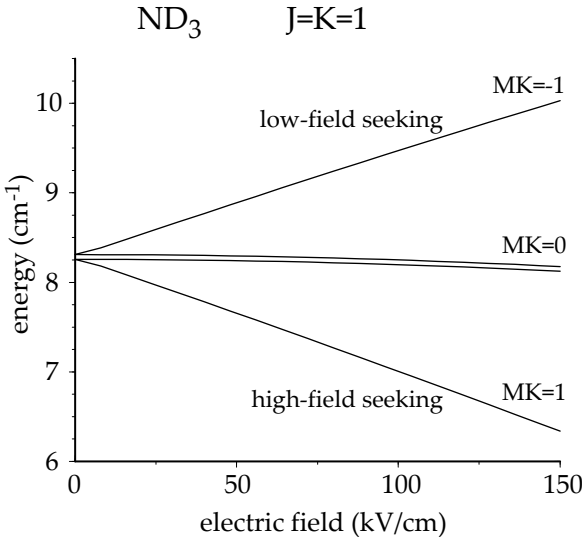
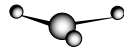


Figure 2.2: The Stark effect of  $\text{ND}_3$  in the  $|J, K\rangle = |1, 1\rangle$  state of the electronic and vibrational ground state.

can be seen from figure 2.2. This shift as a result of an electric field is called the Stark effect. The upper, antisymmetric level is called low-field seeking, as in an inhomogeneous electric field the force  $F = -dW/dx$  is pointed towards the lowest electric field. Analogously, the lower symmetric level is called high-field seeking (see also sections 1.2 and 1.2.2). The smaller the inversion splitting, the stronger the mixing of the inversion doublet components, and also the more linear the Stark effect. As the magnitude of the inversion splitting depends on the mass of the atoms (see also figure 1.2 on page 4), it follows that  $\text{ND}_3$ , with its more linear Stark effect, is the more suitable candidate for our experiments.

In  $\text{NH}_3$ , rovibrational levels are usually labelled according to the symmetry of their nuclear-spin wavefunctions, namely ortho for  $A_2$  symmetry and para for  $E$  symmetry. This notation is only strictly correct when a molecule has two nuclear spin species. In  $\text{ND}_3$ , there are three nuclear spin species, with  $E$ ,  $A_1$ , and  $A_2$  symmetry. Nevertheless, for historic reasons rovibrational levels with  $E$  symmetry are labelled as para levels and levels with either one of the other two symmetries are labelled ortho levels in  $\text{ND}_3$ .

In this chapter, the pure inversion spectra of the ground state of para-ammonia, the  $|J, K\rangle = |1, 1\rangle$  level, are measured and discussed theoretically for  $^{14}\text{ND}_3$  and  $^{15}\text{ND}_3$ . Although the hyperfine structure of  $^{14}\text{NH}_3$  has been studied in the utmost detail [24, 120, 123–129] and its inversion doubling is often being used as a textbook example, the inversion spectra of the deuterated



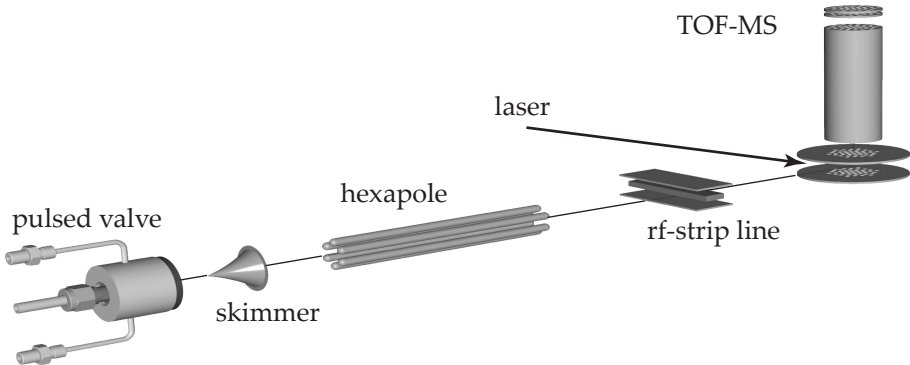


Figure 2.3: Scheme of the pulsed molecular beam spectrometer. ND<sub>3</sub> seeded in xenon is expanded from a pulsed valve. After passage through the skimmer, the ammonia molecules fly through a (pulsed) hexapole lens which focuses (defocuses) the molecules that are in the upper (lower) component of the inversion doublet. Population inversion between these components therefore exists when the molecules enter the approximately 3 cm long rf-interaction region behind the hexapole. There, radiation is applied that is resonant with the  $|J, K\rangle = |1, 1\rangle a \rightarrow s$  transition. By selectively probing the population in the  $s$  component of the inversion doublet via UV laser ionization as a function of the rf-frequency, the pure inversion spectrum is recorded (almost) background-free.

isotopomers of ammonia have received considerably less attention [69, 130–135]. Surprisingly, it seems the hyperfine structure for the deuterated isotopomers have not been resolved nor analyzed at all so far. In the experiments reported here, the inversion spectra in the 1.4–1.6 GHz region are recorded at a 10 kHz resolution using a molecular-beam microwave-UV double-resonance spectrometer. The observed spectra are quantitatively understood, and the energies of all  $|J, K\rangle = |1, 1\rangle$  hyperfine levels of both deuterated ammonia isotopomers are obtained. Implications of the behaviour of the manifold of hyperfine levels in electric fields, both for deceleration and for trapping experiments, are discussed.

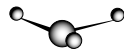
## 2.2 Experiment

The experiments are performed in a pulsed molecular beam spectrometer, schematically shown in figure 2.3. A pulsed valve (modified General Valve, Series 9) expands a 150  $\mu$ s duration gas pulse containing typically 5% of <sup>14</sup>ND<sub>3</sub> or <sup>15</sup>ND<sub>3</sub> seeded in xenon into the source chamber. The most intense part of the beam, which has a mean velocity of around 365 m/s, enters the second vacuum chamber via a skimmer with a 1.5 mm diameter opening. Both

vacuum chambers are pumped by 500 l/s turbo molecular pumps. In the second chamber, the beam passes through a 15 cm long hexapole state-selector, the entrance of which is mounted 15.8 cm downstream from the nozzle. The hexapole consists of 4 mm diameter electrodes, positioned on the outside of a circle with a 4 mm radius. In the molecular beam, about 60% of all the  $\text{ND}_3$  molecules will reside in the  $|J, K\rangle = |1, 1\rangle$  inversion doublet, as this is the ground state for para-ammonia molecules. Further internal relaxation would require nuclear-spin conversion, which does not occur on the time scale of the expansion. In the hexapole, molecules in quantum states with a positive Stark effect (the upper component of the inversion doublet; *a*-symmetry) are focused, whereas molecules in quantum states with a negative Stark effect (the lower component of the inversion doublet; *s*-symmetry) are defocused. This results, therefore, in population inversion between many hyperfine levels of the two inversion doublet components close to the molecular beam axis, downstream from the hexapole.

At a distance of 21 cm from the end of the hexapole, the molecular beam passes through an rf stripline. There, rf-radiation that is resonant with transitions between hyperfine levels in the upper and lower component of the inversion doublet can be applied to the molecules. For  $^{14}\text{ND}_3$  molecules, radiation around 1.6 GHz is required [69], while the corresponding transition for  $^{15}\text{ND}_3$  is around 1.4 GHz [135]. The stripline is impedance matched [136] to the rf-source (50 Ohm) and consists of three aluminum electrodes. The outer two electrodes, both at ground potential, have a width of 40 mm. These electrodes are separated by 19 mm. The middle electrode, connected to the rf-source, is 20 mm wide and 3 mm thick. With this geometry, the reflected power is below 1% over the entire frequency range used in the experiments, while the transmitted power is typically 85%. The molecular beam passes along the center of the 8 mm opening between the lower two electrodes. The field that the molecules experience is fairly homogeneous over the 20 mm width of the middle electrode, and gradually decreases on either side over a typical distance of 5 mm. An rf-synthesizer (Hewlett Packard, HP8657B), providing radiation throughout the 0.1-2060 MHz range with a maximum output power of 50 mW, is used as radiation source. Both the frequency and the output power of the rf-source can be computer-controlled. Calibration of the frequency of the radiation of the rf-source to about  $10^{-8}$  is achieved by connecting the output to a frequency counter, stabilized by an atomic-clock reference signal.

The hexapole is set such that the molecular beam is focused in the laser detection region, some 15 cm downstream from the rf-interaction region. There, the molecules are ionized via a (2+1)-Resonance Enhanced Multi-Photon Ionization (REMPI) process [137]. The required laser radiation of around 317 nm is obtained by frequency doubling the output of a dye laser, that is pumped by a Nd:YAG laser (Spectra Physics, GCR-190/Radiant, Narrowscan combination). Typically, about 10 mJ/pulse in a  $0.05 \text{ cm}^{-1}$  spectral bandwidth, is focused into the detection region by a lens with a focal length of 50 cm, inter-



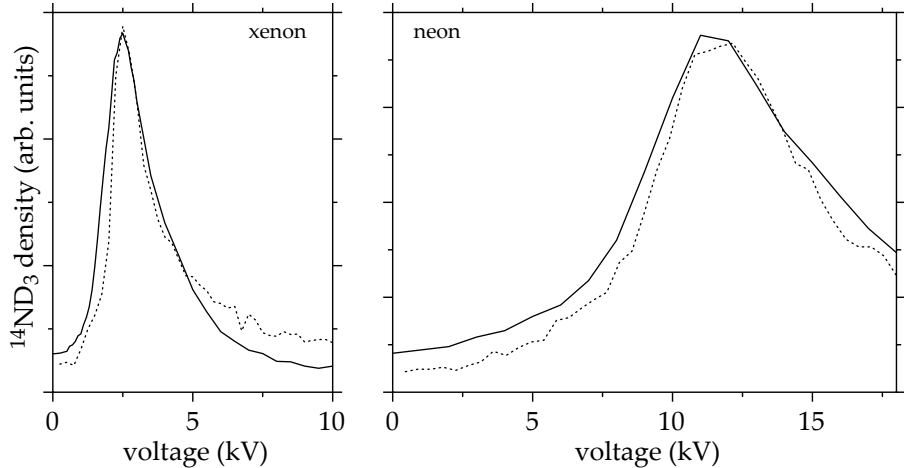


Figure 2.4: Focusing curves (solid lines) for  $^{14}\text{ND}_3$  seeded in xenon (left-hand side) and in neon (right-hand side). The dotted lines result from Monte Carlo calculations.

secting the molecular beam at right angles. The ions produced in the focus of the laser are extracted into a short time-of-flight mass spectrometer and are mass selectively detected.

In figure 2.4, two hexapole focusing curves are shown (solid lines). The density of low-field-seeking  $^{14}\text{ND}_3$  molecules is measured as a function of voltage on the hexapole. On the left-hand side, the ammonia beam is seeded in xenon, whereas on the right-hand side, it is seeded in neon, resulting in a higher average velocity of the beam of around 830 m/s. The higher the applied hexapole voltage, the closer the spatial focus of the ammonia beam moves towards the hexapole. When the beam is seeded in xenon, the ammonia density at the position of the laser focus reaches a maximum at a voltage of around 2.5 kV, indicating that the focus of the ammonia beam has reached the laser. At higher voltages, the beam is overfocused, resulting in a lower density at the detection point. The same measurement for a  $^{14}\text{ND}_3$  beam seeded in neon results in a higher voltage of around 11 kV for optimal focusing. As the neon-seeded beam has a higher velocity, the focusing force acts on the molecules for a smaller amount of time, which necessitates the use of a higher force, i.e., a higher applied voltage, to achieve focusing on the same position. The dotted lines in figure 2.4 are the result of Monte Carlo calculations.

Figure 2.5 shows the ionization spectra of  $^{14}\text{ND}_3$  and  $^{15}\text{ND}_3$ , that were measured simultaneously by expanding a combined mixture of both ND<sub>3</sub> isotopes in xenon from the pulsed valve. The frequency of the ionizing laser was scanned and both isotopes were ionized and detected in the time-of-flight mass

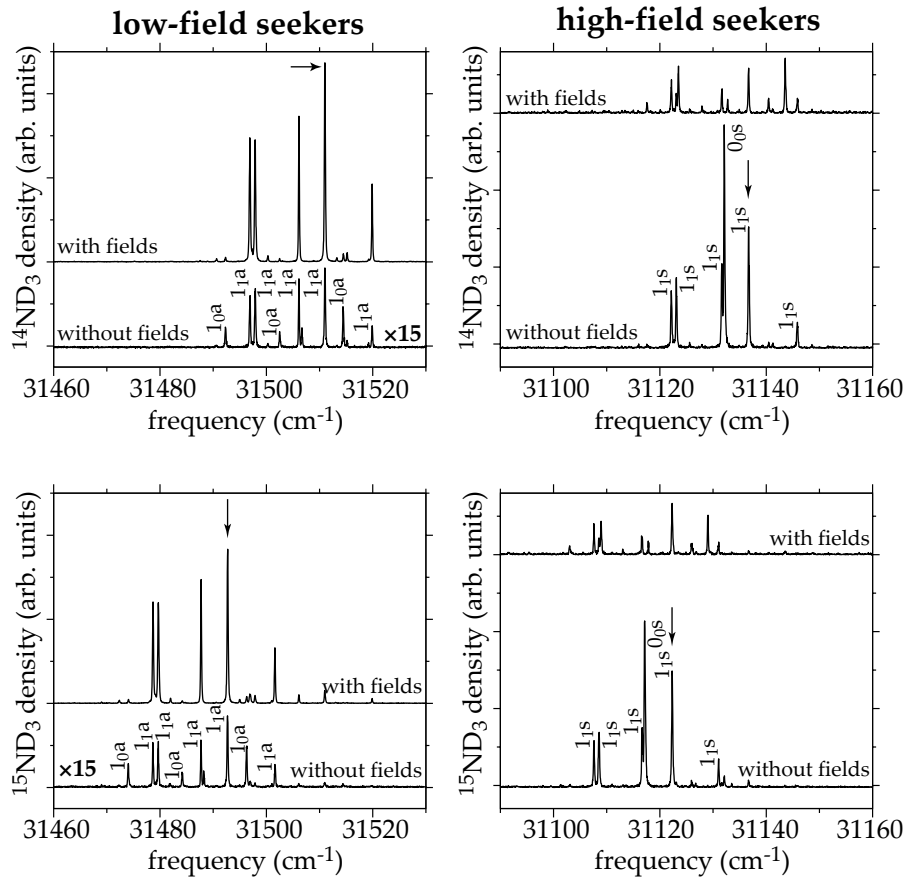


Figure 2.5: The ionization spectra of both  $^{14}\text{ND}_3$  (upper graphs) and  $^{15}\text{ND}_3$  (lower graphs). The left graphs show the ionization of molecules in the upper component of the  $|J, K\rangle = |1, 1\rangle$  inversion doublet (including the low-field-seeking states), whereas the right graphs show the ionization of molecules in the lower component of the inversion doublet (including the high-field-seeking states). The particular  $J_K$  level the molecules originate from is indicated for those levels that are most pronounced. All measurements have been performed both with a focusing or defocusing electric field on, and off. The arrows indicate the transitions used in the experiments to detect ammonia ( $^{14}\text{ND}_3$  or  $^{15}\text{ND}_3$ ) in the low- or high-field-seeking state.



spectrometer. During ionization, only a small field was present ( $\approx 0.4$  kV/cm) to accelerate the ions towards the detector. The resonant levels in the (2+1)-REMPI process, the vibrational states in the B-level, each have their own symmetry. Two-photon transitions are only allowed from symmetric to symmetric levels, or from antisymmetric to antisymmetric levels. Therefore, the low- and high-field-seeking states, that have *a* and *s* symmetry, respectively, can be detected state-selectively. To detect molecules in the symmetric  $|J, K\rangle = |1, 1\rangle$  state, the symmetric B(4) state is used, whereas the B(5) state, which is antisymmetric, is used to detect molecule in the antisymmetric  $|J, K\rangle = |1, 1\rangle$  state.

In both upper graphs in figure 2.5  $^{14}\text{ND}_3$  measurements are shown, while  $^{15}\text{ND}_3$  measurements are shown in both lower graphs. On the left-hand side, the ionizing laser was tuned around the  $B(5) \leftarrow X(\nu_2 = 1)$  transition, to detect low-field-seeking molecules. Without any fields, a multitude of lines can be seen, that originate from different  $J_K$  levels, as indicated in the figure (note the multiplication factor of 15). Only molecules in the  $|J, K\rangle = |1, 1\rangle$  state are low-field seeking, and as these levels are focused when the electric fields are on, the upper spectra result, with the  $|J, K\rangle = |1, 1\rangle$  lines much more pronounced. The measurements were taken in a somewhat different setup than the one already described. In this setup, to be discussed later in chapters 4 and 5, the focusing electric fields did not originate from a hexapole only, but also from a Stark decelerator (see also section 3.2). As a result, the ratio of the intensities of the focused and unfocused lines is about 30, rather than about 10 for the hexapole only (see figure 2.4).

On the right-hand side, the ionizing laser was tuned around the  $B(4) \leftarrow X(\nu_2 = 0)$  transition, for detection of high-field-seeking molecules. Turning the fields on now results in defocusing, and the intensity of most lines is seen to decrease. A notable exception is the line at  $31143.6\text{ cm}^{-1}$  for  $^{14}\text{ND}_3$  ( $31129.0\text{ cm}^{-1}$  for  $^{15}\text{ND}_3$ ), which is actually seen to increase. As the Stark behavior of this line is identical to the behavior of the known low-field-seeking  $|J, K\rangle = |1, 1\rangle$  lines, both in magnitude and as a function of electric field strength, it is believed that this line originates from the antisymmetric  $|J, K\rangle = |1, 1\rangle$  level as well, but uses a different resonant level in the REMPI process. Overall, the transition frequencies of  $^{15}\text{ND}_3$  are red-shifted over about  $10\text{ cm}^{-1}$  with respect to the  $^{14}\text{ND}_3$  transitions. The transitions that are used in the double-resonance experiments to detect either isotope of ammonia in the low- or high-field-seeking state are indicated by arrows. In each case, the  $\Delta K = +1$ ,  $\Delta J = +2$  transition is used (at  $31511\text{ cm}^{-1}$  for the *a*-level and at  $31136.7\text{ cm}^{-1}$  for the *s*-level of  $^{14}\text{ND}_3$  in the  $|J, K\rangle = |1, 1\rangle$  state [137]).

Returning to the original setup, microwave spectra are obtained by scanning the rf-frequency while keeping the detection laser fixed on the resonances discussed in the previous paragraph (indicated by arrows in figure 2.5). When the *a*-level is probed, a microwave transition is observed as a decrease in the ion signal, whereas an increase in the ion signal is observed when the *s*-level

is probed. The best signal-to-noise ratio for the inversion spectra is obtained in the latter situation, as rf-transitions are then measured as an increase in ion signal against a strongly reduced background signal. The remaining background signal stems from ammonia molecules originally already residing in the lower component of the inversion doublet that travel close to the hexapole axis and that are hardly deflected. The insertion of a 1 mm diameter beamstop directly behind the hexapole reduces this background signal to about 70% of its original value and thereby further increases the detection sensitivity.

To focus ammonia molecules in low-field-seeking states in the laser detection region, a constant voltage difference of about 2.5 kV can be applied to neighboring rods of the hexapole (see also figure 2.4). As the electric field near the entrance and the exit of the hexapole drops off to zero on a typical distance of about 5 mm, the molecules then experience an increasing and decreasing electric field on the tens of  $\mu\text{s}$  time scale. This is slow enough that the molecules will follow the Stark curves adiabatically. This results, however, in a complicated population distribution over the various hyperfine levels for those molecules that enter the rf-interaction region; hyperfine levels composed of (at least some)  $M_F$  sub-levels that are low-field seeking will be predominantly populated. Molecules in some hyperfine levels will not be focused at all, in which case microwave transitions originating from these levels are absent in the spectra, complicating the spectral assignment. Therefore, in most of the experiments reported below an 8.5 kV voltage difference that can rapidly be switched on and off is applied to neighboring hexapole rods for a 110  $\mu\text{s}$  duration when the gas pulse is completely inside the hexapole. The high-voltage is switched on and off on a 200 ns time scale, which is sufficiently fast to break the adiabatic following as the hyperfine levels are all within a few MHz from each other (*vide infra*). This leads to a re-distribution of the population over various hyperfine levels within a component of the inversion doublet, obeying the  $\Delta M_F = 0$  selection rule. As the switching off of the electric field does not affect the velocity of the molecules, molecules eventually residing in hyperfine levels of the upper inversion doublet component which almost experience no Stark effect will now be focused in the detection region as well. In the simulation of the spectra it is assumed that upon entering the rf-transition region, all hyperfine levels of the upper inversion doublet component are equally populated, which appears to describe the experimental situation rather well.

## 2.3 Results and Discussion

### 2.3.1 Inversion spectra of $^{14}\text{ND}_3$

In figure 2.6 an overview spectrum is shown of the  $|J, K\rangle = |1, 1\rangle$  inversion spectrum of  $^{14}\text{ND}_3$  as obtained by probing the population in the upper component (top trace) and in the lower component (bottom trace) of the inversion doublet



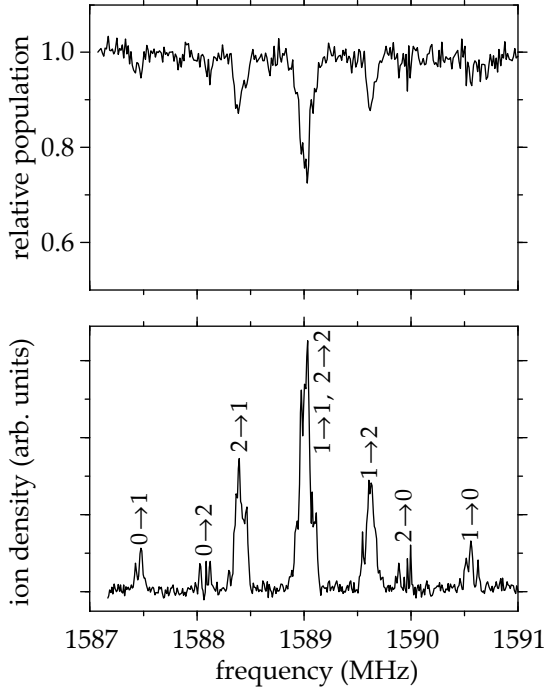


Figure 2.6: Pure inversion spectrum of  $^{14}\text{ND}_3$  ( $|J, K\rangle = |1, 1\rangle$ ), measured by probing both the upper component (upper trace) and the lower component (lower trace) of the inversion doublet. The spectra are recorded at high microwave powers (1 mW) and are power broadened. Assignment of the main  $F'_1 \rightarrow F''_1$  features is given in the spectrum.

under otherwise identical conditions. It is clear that the lower spectrum has the better signal-to-noise ratio. To be able to also observe the weaker spectral features, a relatively high rf-power of 1 mW is used for these measurements. Under these conditions many of the transitions observed in the spectrum are saturated and the observed linewidth for those transitions is mainly determined by power broadening. From the measurements presented in the upper trace it is seen that up to 30% of the molecules originally distributed over hyperfine levels of the *a*-symmetry component are optically pumped to a selected subset of hyperfine levels in the *s*-symmetry component.

The main structure observed in these spectra can be understood by taking into account the quadrupole interaction of the  $^{14}\text{N}$  nucleus only. This is the dominant interaction term, and leads to a splitting of each component of the inversion doublet in three (groups of) levels. Each of these (groups of) levels can be labeled by the quantum number  $F_1$ , where  $\vec{F}_1 = \vec{J} + \vec{I}_N$ ,  $\vec{I}_N$  being the

nitrogen nuclear spin vector (see also figure 2.9). The  $F'_1 \rightarrow F''_1$  assignment of the main groups of lines is indicated in the lower spectrum of figure 2.6. It should be noted that the  $0 \rightarrow 1$  and  $0 \rightarrow 2$  transitions, as well as some other lines originating from  $F'_1 = 2$  levels, are only observed when the hexapole is rapidly switched off, as is done here, i.e., when re-distribution of the population over the hyperfine levels occurs. As  $F_1$  is almost a good quantum-number, the  $\Delta F_1 = \pm 2$  transitions are only weakly allowed, and are therefore considerably less power broadened.

In figure 2.7 experimental high-resolution inversion spectra of the spectral regions around the five strongest  $F'_1 \rightarrow F''_1$  transitions are shown. All five spectra are plotted on the same intensity scale, and are recorded under identical conditions. For these measurements the rf-power is reduced to  $5 \mu\text{W}$  to stay sufficiently far away from saturation. For all  $F'_1 \rightarrow F''_1$  transitions a rich substructure is observed. The width of isolated spectral lines is observed to be about 10 kHz, in good agreement with the linewidth expected for transit-time broadening of the (relatively slow) molecules passing through the effectively 30 mm wide rf-interaction region. The lower trace in each of the graphs is a simulation based on the best fit to the experimentally determined transition frequencies, as will be discussed in more detail below. In the simulation, a Gaussian line-shape with a 10 kHz linewidth (full width at half maximum) is used. Both the peak position and the relative intensities of most features in the less condensed frequency regions are well reproduced. It can be seen though, that especially in the region around 1589.0 MHz the match is less than perfect.

In figure 2.8, the corresponding high-resolution spectra for the weaker  $\Delta F_1 = \pm 2$  transitions, recorded with higher rf-powers, are shown. The spectra in the upper panel are well reproduced by simulations based on the results of the best fit, shown as the lower trace in the graph. Although the spectra in the lower panel do not show such a perfect match for the relative intensities, the line positions do have a good match with the simulations.

It should be emphasized that for all high-resolution microwave spectra presented here, no significant changes are observed when the ionization laser is tuned to a different transition, i.e., when a different intermediate state is used to probe the population in the same component of the inversion doublet; apparently there is no significant hyperfine-level selectivity in the UV-laser based detection process.

### 2.3.2 Energy levels, fitting parameters and Stark effect for $^{14}\text{ND}_3$

To assign and simulate the experimental spectra, a general formalism to describe the Hamiltonian for the four different symmetric-top ammonia isotopomers ( $^{14}\text{NH}_3$ ,  $^{15}\text{NH}_3$ ,  $^{14}\text{ND}_3$  and  $^{15}\text{ND}_3$ ) is used. The generalized tensor coupling scheme that is set up allows the Hamiltonian to be tested on the experimentally well characterized  $^{14}\text{NH}_3$  system [24], prior to being applied to



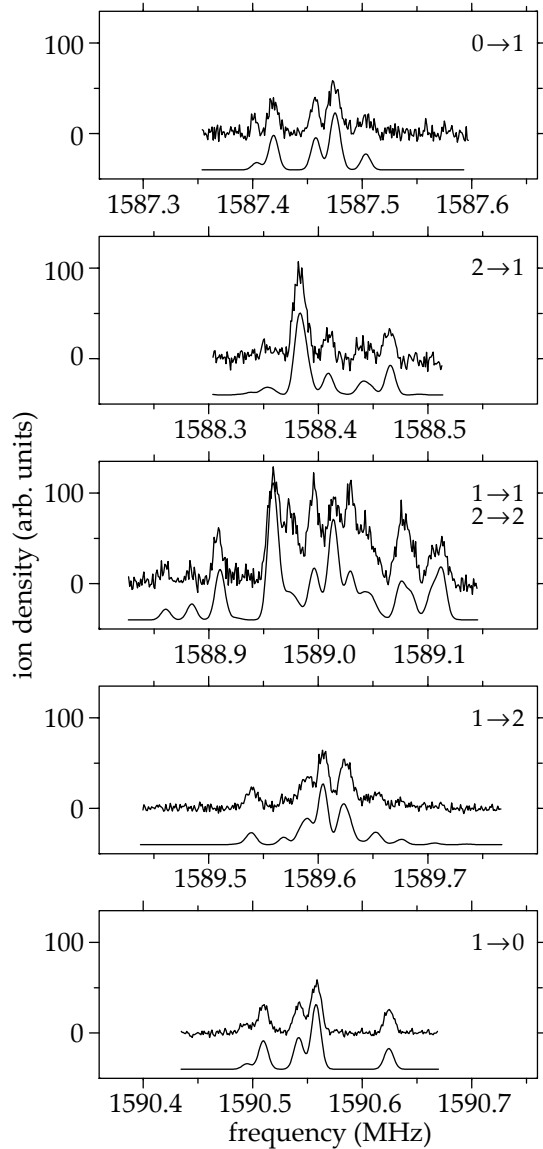


Figure 2.7: The five main  $F'_1 \rightarrow F''_1$  transitions in the microwave spectrum of  $^{14}\text{ND}_3$ , recorded with a spectral resolution of 10 kHz. The upper trace in each of the graphs shows the experimental spectrum while the lower trace is the simulated spectrum, using the parameters in the Hamiltonian as obtained from the best fit.

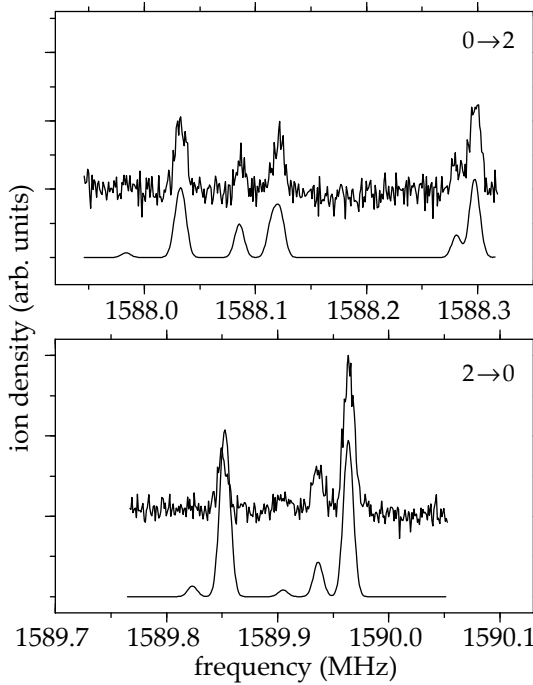
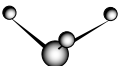


Figure 2.8: The weak  $F'_1 = 0 \rightarrow F''_1 = 2$  and  $F'_1 = 2 \rightarrow F''_1 = 0$  transitions for  $^{14}\text{ND}_3$ , recorded at increased rf-powers of 0.25 mW and 0.13 mW, respectively. Underneath the experimental spectra, the simulated spectra are shown.

the more complex deuterated ammonia isotopomers.

To describe the hyperfine structure in the required detail, all the spin-spin and spin-rotation terms off-diagonal in  $F_1$  need to be taken into account [24].  $\vec{F}_1$  is arrived at by adding the nuclear spin  $\vec{I}_N$  of the N atom to the rotational angular momentum  $\vec{J}$  (see figure 2.9). As the three deuterium atoms are in equivalent positions, their nuclear spins are coupled to give the overall deuterium nuclear-spin angular-momentum vector  $\vec{I}_D$ . This vector couples to  $\vec{F}_1$ , which results in  $\vec{F}$ , providing the (only) good quantum numbers  $F$  and  $M_F$ , the projection of  $F$  on the electric field vector. Note that, as the formalism is generalized to describe all isotopomers mentioned above, any time that deuterium is mentioned, one can read hydrogen instead as well. The total wave function of the molecule is represented via the coupling of vibration (inversion tunneling), rotation and spin wave functions, all of them being treated as tensors. Both the wave functions and the Hamiltonian are reduced to the irreducible symmetry representation. A detailed description of this formalism is given elsewhere [138].



Symmetry group formalism	Ref. [24]	Parameters [MHz] for			
		<sup>14</sup> NH <sub>3</sub> <sup>a</sup>	<sup>15</sup> NH <sub>3</sub> <sup>b</sup>	<sup>14</sup> ND <sub>3</sub>	<sup>15</sup> ND <sub>3</sub>
$c_t^c$	$\Omega_t$	23694.4955	22613.4955	1589.0094 (3)	1430.3400 (6)
$c_{QN}$	$\sqrt{15/8} eQq_s$	-5.6025	0	-5.591 (2)	0
$\delta c_{QN}$	$\sqrt{15/8} (eQq_a - eQq_s)$	0.0038	0	0.0000	0
$c_{JN1}$	$-(2a+b)/\sqrt{3}$	-0.0117	0.0165	-0.0062 (4)	0.0082
$c_{JN2}$	$-\sqrt{10/3}(a-b)$	-0.0002	0.0003	-0.00018	0.00013
$c_{JD1}$	$-(3A+C)$	0.0549	0.0549	0.005 (1)	0.004 (1)
$c_{JD2}$	$\sqrt{10} C$	-0.0030	-0.0030	-0.0002	-0.0002
$c_{JD3}$	$\sqrt{30} B$	0.0802	0.0802	0.0062	0.0062
$c_{ND1}^d$	$-3\sqrt{10} D_1$	0.0231	-0.0323	0.0035	-0.0050
$c_{ND2}^d$	$\sqrt{30} D_2$	-0.0575	0.0806	-0.009 (2)	0.017 (6)
$c_{DD1}^d$	$3\sqrt{5/2} D_3$	0.1289	0.1289	0.003	0.003
$c_{DD2}^d$	-	0.2233	0.2233	0.005	0.005
$c_{QD1}$	-	0	0	-0.221 (9)	-0.221 (8)
$c_{QD2}$	-	0	0	0.429 (3)	0.434 (3)

Table 2.1: Adjustable parameters in the Hamiltonian, together with their correspondence to parameters in the more commonly used notation. Their values as obtained from the best fit to the experimentally observed <sup>14</sup>ND<sub>3</sub> and <sup>15</sup>ND<sub>3</sub> transition frequencies are given. The standard deviation of the fit is about 2 kHz, both for <sup>14</sup>ND<sub>3</sub> and for <sup>15</sup>ND<sub>3</sub>.

<sup>a</sup>Values taken from Ref. [24].

<sup>b</sup>Values scaled to parameters from <sup>14</sup>NH<sub>3</sub>.

<sup>c</sup>Only the statistical error is indicated. Electric field components along the molecular beam axis can cause a maximum Doppler shift of 1.8 kHz. As the field is directed mainly perpendicular to the molecular beam axis, this effect will be small, however.

<sup>d</sup>Initial approximate values for these parameters can be calculated from the geometry ( $R_{ND} \simeq 1.02 \text{ \AA}$ , and  $\beta \simeq 68^\circ 53'$ ) of the molecule via the following formulas:  $c_{ND1} \simeq 3\sqrt{10} \cdot (g_N/I_N) (g_D/I_D) \mu_0^2 ((3/2) \sin^2 \beta - 1)/R_{ND}^3$ ,  $c_{ND2} \simeq -3\sqrt{15/2} \cdot (g_N/I_N) (g_D/I_D) \mu_0^2 \sin^2 \beta/R_{ND}^3$ ,  $c_{DD1} \simeq 3\sqrt{5/2} \cdot ((g_D/I_D) \mu_0)^2/R_{DD}^3$ ,  $c_{DD2} \simeq \sqrt{3} c_{DD1}$ , in which  $\mu_0$  is the nuclear magneton. In the fitting procedure only the largest parameter ( $c_{ND2}$ ) could be further refined.

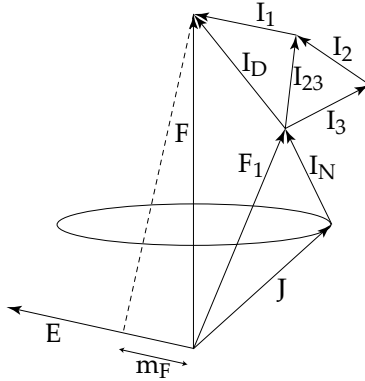


Figure 2.9: The vector coupling scheme of nuclear spin and angular momentum operators.

The parameters used in the Hamiltonian are given in the first column of table 2.1. Here we will just briefly indicate the physical meaning of the various parameters, in order of their appearance in the table. The parameter  $c_t$  describes the magnitude of the inversion splitting. The parameter  $c_{QN}$  represents the strength of the quadrupole interaction of the nitrogen atom, while  $\delta c_{QN}$  is a correction to that term for the upper inversion doublet component only, probably due to a slight difference in the internal electric field [24]. The parameters  $c_{JN1}$  and  $c_{JN2}$  determine the coupling strength of the rotational angular momentum  $\vec{J}$  and the nuclear spin of the nitrogen atom  $\vec{I}_N$ . This requires two parameters, because of the difference in the interaction between rotation that is either perpendicular or parallel to the symmetry axis of ammonia. The next three parameters,  $c_{JD1}$ ,  $c_{JD2}$ , and  $c_{JD3}$  describe the interaction of the rotational angular momentum with the total nuclear spin of the deuterium atoms. This time, three parameters are needed due to the fact that the deuterium atoms are not located on the symmetry axis. The parameters  $c_{ND1}$  and  $c_{ND2}$  describe the spin-spin interaction between the nitrogen and deuterium atoms, while  $c_{DD1}$  and  $c_{DD2}$  describe the spin-spin interaction between two deuterium atoms. Finally,  $c_{QD1}$  and  $c_{QD2}$  describe the quadrupole interaction of the deuterium atoms. The corresponding parameters in the more conventional representation of the Hamiltonian [24, 124] are given in table 2.1 as well.

An approximate initial value for most parameters in the Hamiltonian for  $^{14}\text{ND}_3$  is obtained by an appropriate scaling of the corresponding (known) parameters for  $^{14}\text{NH}_3$ , given in the third column of table 2.1. To do so, the formula for the nuclear magnetic moment as given in reference [139] is used. It is noted that the nuclear magnetic moment has to be scaled to the absolute value of the nuclear spin, which is actually not done in most textbooks and



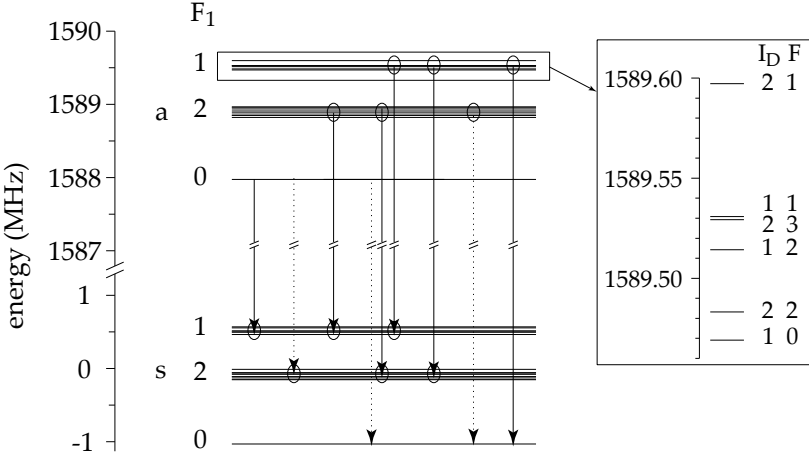


Figure 2.10: Energy level structure of  $^{14}\text{ND}_3$  ( $|J, K\rangle = |1, 1\rangle$ ). The quadrupole interaction of the  $^{14}\text{N}$  atom causes the main splitting of both the upper and the lower component of the inversion doublet in three levels, labeled with the quantum number  $F_1$ . The nuclear spins of the deuterium atoms cause additional splittings, shown enlarged for the  $F_1 = 1$  component at the right-hand side of the figure. The strong (weak)  $F'_1 \rightarrow F''_1$  transitions observed in the experimental spectra are indicated by solid (dashed) arrows.

which is the (trivial) explanation for the apparent discrepancy discussed at length in the paper of Kukolich<sup>1</sup>. The parameters in the Hamiltonian that best describe the experimental data for  $^{14}\text{ND}_3$ , as obtained by fitting the observed transition frequencies of 33 more or less isolated lines, are listed in the fifth column of table 2.1. For each parameter the standard deviation from the fit is indicated between brackets. Those parameters that are listed without standard deviation are kept fixed in the fitting procedure at the values obtained from direct scaling from  $^{14}\text{NH}_3$  as these parameters can not be further refined, i.e., as standard deviations larger than the actual value of the parameters are obtained when attempting to fit these parameters.

In figure 2.10 the energy level structure of  $^{14}\text{ND}_3$  ( $|J, K\rangle = |1, 1\rangle$ ), as obtained from the best fit to the experimental data, is shown. Zero energy is chosen as the position of the lower inversion doublet component when all interactions are switched off, i.e., when all parameters in the first column of table 2.1 except  $c_t$  are equal to zero. The main splitting in three sets of levels, labeled by the quantum number  $F_1$ , in each of the components of the inversion dou-

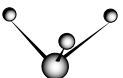
<sup>1</sup>In reference [24] every time that  $g_{H,N}$  appears it should be replaced by  $g_{H,N}/I_{H,N}$ . This leads to a  $2^{1/3}$  larger N–H bondlength than determined in Ref. [24], in good agreement with literature values.

s-level					a-level				
$F_1$	$I_D$	$F$	energy (MHz)	levels shifted	$F_1$	$I_D$	$F$	energy (MHz)	levels shifted
0	2	2	-1.0322	all	0	1	1	1587.9758	0
0	1	1	-1.0312	all	0	2	2	1587.9758	0
2	2	3	-0.1506	all	2	2	0	1588.8262	0
2	1	1	-0.1431	all	2	2	1	1588.8532	0
2	2	2	-0.1138	all	2	1	2	1588.8566	0
2	1	3	-0.1107	all	2	2	4	1588.8839	2
2	2	4	-0.0780	all	2	1	3	1588.9069	all
2	2	1	-0.0625	all	2	2	2	1588.9387	all
2	1	2	-0.0576	all	2	1	1	1588.9651	all
2	2	0	-0.0118	all	2	2	3	1588.9665	all
1	2	1	0.4684	0	1	1	0	1589.4678	all
1	1	1	0.4938	0	1	2	2	1589.4819	all
1	2	3	0.4976	0	1	1	2	1589.5150	all
1	1	2	0.5141	0	1	2	3	1589.5301	all
1	2	2	0.5526	0	1	1	1	1589.5302	all
1	1	0	0.5680	0	1	2	1	1589.5968	all

Table 2.2: Hyperfine energy levels for  $^{14}\text{ND}_3$  ( $|J, K\rangle = |1, 1\rangle$ ) as obtained from the best fit to the experimental data. For each hyperfine level, the number of  $M_F$  components that is shifted (up in the *a*-symmetry level or down in the *s*-symmetry level) is indicated.

blet is caused by the quadrupole interaction of the  $^{14}\text{N}$  nucleus, as discussed before. The nuclear spins of the deuterium atoms cause additional splittings, shown enlarged for the  $F_1 = 1$  component at the right-hand side of the figure. Within each component of the inversion doublet all hyperfine levels are within an approximate 1.5 MHz energy range. In the figure, the (groups of) transitions observed in the spectra shown in figure 2.6 are schematically indicated. The energies of the 32 hyperfine levels (16 levels for each component of the inversion doublet) are given in table 2.2, together with the quantum numbers  $F_1$ ,  $I_D$ , and  $F$ .

With all the hyperfine levels of the  $|J, K\rangle = |1, 1\rangle$  state in  $^{14}\text{ND}_3$  known, the splitting and shifting of the individual hyperfine levels in external electric fields can be calculated, using the same tensor coupling scheme. For this, the block-matrices describing the levels in the *s*-symmetry and the *a*-symmetry components are coupled via the appropriate  $\vec{E} \cdot \vec{d}$  coupling terms, and the full matrix is diagonalized. In figure 2.11 the calculated Stark shift for the manifold of hyperfine levels is shown in electric fields up to 100 V/cm. It is seen from this figure that none of the  $M_F$  components of the two  $F_1 = 0$  hyperfine-levels in the *a*-symmetry component of the inversion doublet is low-field seeking. Molecules



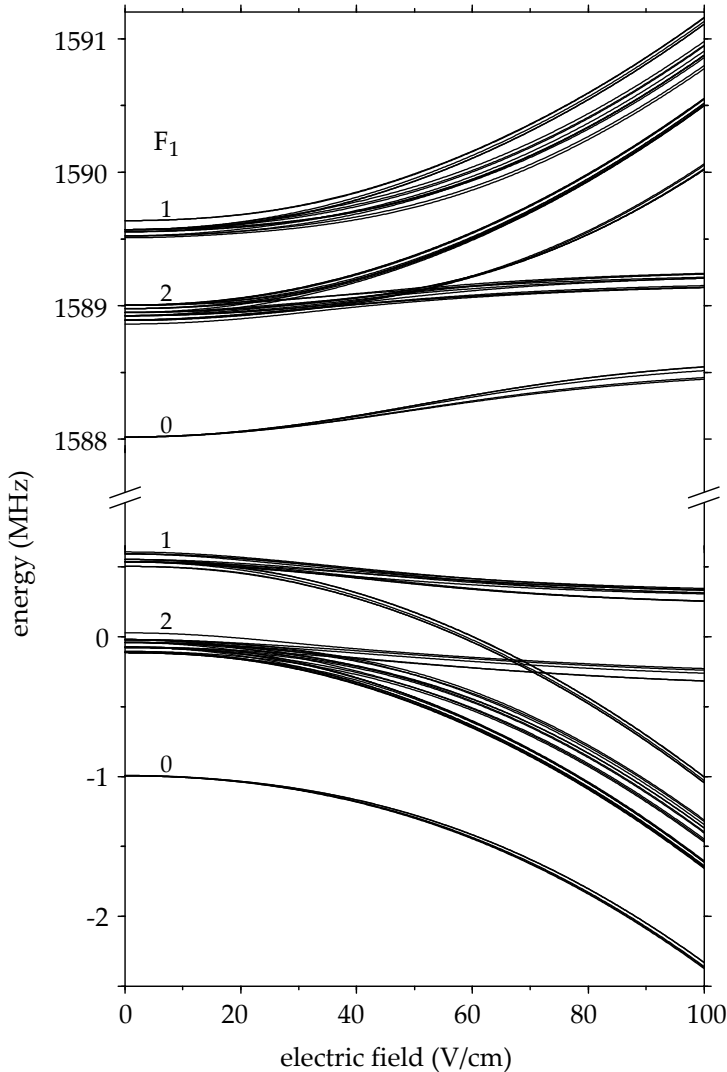
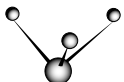


Figure 2.11: Calculated Stark shift for the manifold of hyperfine levels of  $^{14}\text{ND}_3$  in electric fields up to 100 V/cm.

in these two levels will therefore not be focused, explaining the absence of the transitions originating from these levels in spectra that are recorded when the hexapole is operated with constant voltages, as discussed earlier. Only the  $F = 4$  level of the central group of  $F_1 = 2$  hyperfine levels in the upper component of the inversion doublet has both  $M_F$  components that are low-field seeking and  $M_F$  components that are hardly shifted in energy in an electric field. The most interesting, and *a priori* not expected, feature of the Stark curves shown in figure 2.11 is that four hyperfine levels of the  $F_1 = 2$  group of levels, as well as all hyperfine levels belonging to the highest energy  $F_1 = 1$  group of levels in the upper component of the inversion doublet are exclusively low-field seeking. For each hyperfine level the number of  $M_F$  components that is shifted in an electric field (up for the *a*-symmetry component and down for the *s*-symmetry component) is summarized in table 2.2.

When different  $M_F$  components are degenerate in zero electric field, Majorana transitions can occur. In the Stark decelerator, for instance, the molecules pass through an array of electric field sections that are switched a large number of times from high field to low field. In that case, ‘low fields’ are typically still a few kV/cm, i.e., (very) far from zero electric field, preventing Majorana transitions that would otherwise lead to beam loss. The rapid switching of the field in the decelerator will lead to scrambling between the various low-field-seeking  $M_F$  components, as these stay within a few MHz from each other almost independent of the strength of the electric field, but this does not lead to beam loss. In the quadrupolar and hexapolar electrostatic trapping geometry that we have used thus far for trapping of the  $\text{ND}_3$  molecules, however, the electric field is really zero at the trap center (see chapter 4). Here, the trapped ammonia molecules, i.e., the ammonia molecules in low-field-seeking  $M_F$  levels, can undergo Majorana transitions, possibly leading to trap loss. As preferentially the coldest molecules are removed via those Majorana transitions, this leads to heating of the remaining sample of trapped molecules in thermalizing collisions as well. Majorana transitions can be avoided in an electrostatic trapping geometry with a non-zero electric field at the trapping center, and design studies for such a trap, the analog of the Ioffe-Pritchard magnetic trap, have been made [64, 65].

For those hyperfine levels of ammonia that are exclusively low-field seeking, trap loss due to Majorana transitions can simply not occur, enabling the stable confinement of these molecules in a trapping geometry with a true zero electric-field region inside. This property is highly relevant and can for instance be exploited in future high-resolution spectroscopy studies. In the quadrupole electrostatic trap, the trapped  $^{14}\text{ND}_3$  molecules are initially equally distributed over the various low-field-seeking  $M_F$  states. Even if Majorana transitions are efficient, only molecules in the low-field-seeking  $M_F$  components of the  $F_1 = 2$ ,  $F = 4$  hyperfine level (2 out of 48 populated  $M_F$  components) can be lost from the trap in the absence of collisions.



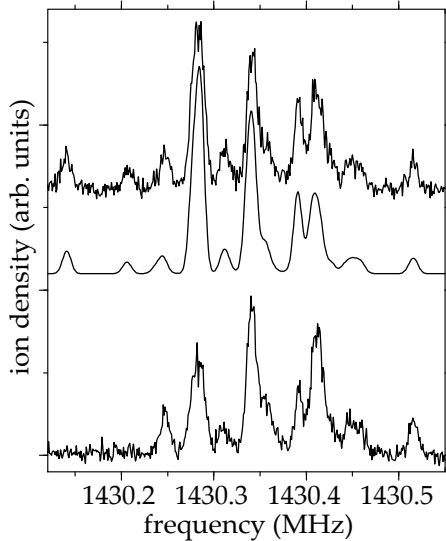


Figure 2.12: High-resolution pure inversion spectra of  $^{15}\text{ND}_3$  ( $|J, K\rangle = |1, 1\rangle$ ), measured by probing the lower inversion level. The upper experimental spectrum is recorded while operating the hexapole in the pulsed mode, and is shown together with the theoretical spectrum obtained from the best fit to the experimental data. The lower experimental spectrum is recorded while the molecules leave the hexapole adiabatically.

### 2.3.3 Energy levels, fitting parameters and Stark effect for $^{15}\text{ND}_3$

The high-resolution inversion spectrum has been recorded for the  $|J, K\rangle = |1, 1\rangle$  level in  $^{15}\text{ND}_3$  as well, and the full spectrum is shown in figure 2.12. As the  $^{15}\text{N}$  nucleus has no quadrupole moment, the main splitting pattern that could immediately be recognized in the spectrum of  $^{14}\text{ND}_3$  is now absent, and the whole spectrum covers less than 400 kHz. The upper part shows the spectrum obtained when the hexapole is operated in the pulsed mode, together with the simulated spectrum. The lower part shows the spectrum obtained when a constant voltage is applied to the hexapole. Clearly, several lines are absent, and relative line intensities of other lines are different compared to the upper spectrum. From the good match of the simulated spectrum to the upper experimental spectrum, it can be concluded that the re-distribution amongst the various hyperfine levels of the upper component of the inversion doublet is nearly complete when the voltages on the hexapole are rapidly switched on and off.

The parameters in the Hamiltonian that are obtained from a fit to the

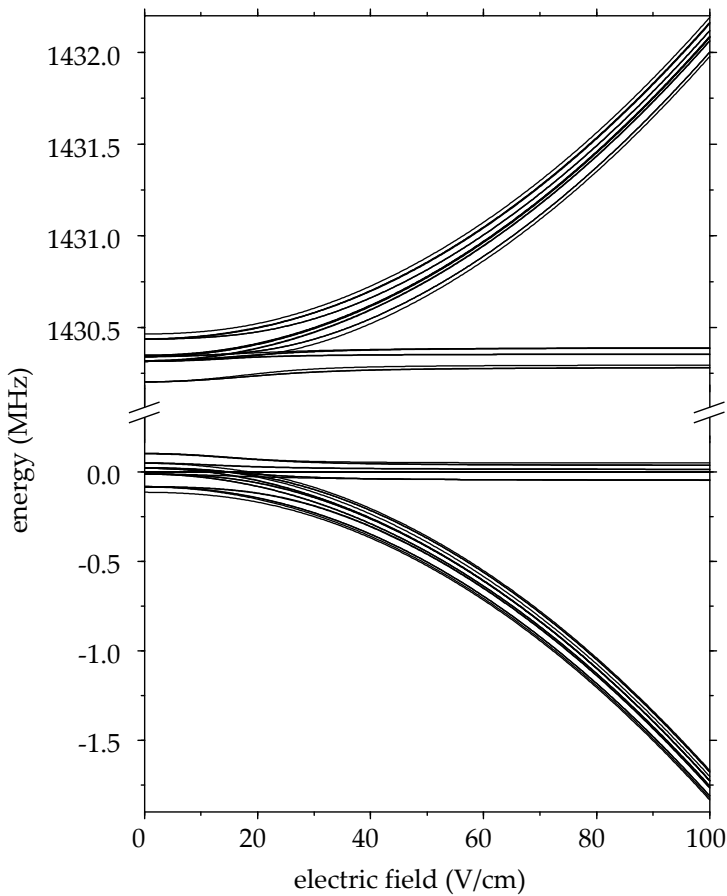
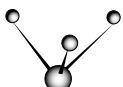


Figure 2.13: Calculated Stark shift for the manifold of hyperfine levels of  $^{15}\text{ND}_3$  in electric fields up to 100 V/cm.



s-level					a-level				
$F_1$	$I_D$	$F$	energy (MHz)	levels shifted	$F_1$	$I_D$	$F$	energy (MHz)	levels shifted
3/2	1	1/2	-0.1179	all	3/2	1	3/2	1430.1952	0
3/2	2	5/2	-0.0846	all	3/2	2	1/2	1430.1958	0
3/2	2	3/2	-0.0816	all	3/2	2	7/2	1430.3059	2
3/2	1	5/2	-0.0141	all	1/2	2	5/2	1430.3120	2
1/2	1	3/2	-0.0090	all	3/2	1	5/2	1430.3300	all
3/2	2	7/2	0.0192	all	3/2	1	3/2	1430.3340	all
1/2	2	5/2	0.0245	2	3/2	2	1/2	1430.3393	all
3/2	1	3/2	0.0527	0	1/2	1	3/2	1430.3432	all
1/2	1	1/2	0.0562	0	1/2	2	3/2	1430.4332	all
3/2	2	1/2	0.0921	0	3/2	2	5/2	1430.4335	all
1/2	2	3/2	0.0955	0	3/2	1	1/2	1430.4598	all

Table 2.3: Hyperfine energy levels for  $^{15}\text{ND}_3$  ( $|J, K\rangle = |1, 1\rangle$ ) as obtained from the best fit to the experimental data. For each hyperfine level, the number of  $M_F$  components that is shifted (up in the *a*-symmetry level or down in the *s*-symmetry level) is indicated.

transition frequencies of 13 more or less isolated lines in the spectrum of  $^{15}\text{ND}_3$  are listed in the last column of table 2.1. An approximate initial value for these parameters is now obtained by scaling the parameters found for  $^{14}\text{ND}_3$ . The energies of the 22 hyperfine levels (11 levels for each component of the inversion doublet) are given in table 2.3, together with the quantum numbers  $F_1$ ,  $I_D$ , and  $F$ , and the number of  $M_F$  components that is shifted when an electric field is applied.

In figure 2.13 the calculated Stark shift for the manifold of hyperfine levels of  $^{15}\text{ND}_3$  is shown in electric fields up to 100 V/cm. It is seen that in this case as well, 7 out of 11 hyperfine levels in the upper component of the inversion doublet are exclusively low-field seeking, and no Majorana transitions are possible for these levels. As the hyperfine levels in each component of the inversion doublet are within 300 kHz from each other, it is clear that the re-distribution of the population over the various hyperfine levels by rapidly switching the fields in the hexapole is rather efficient.

## 2.4 Conclusions

In this chapter, high-resolution pure inversion spectra have been obtained for  $^{14}\text{ND}_3$  and  $^{15}\text{ND}_3$  para-ammonia molecules in their ground state, using a molecular-beam microwave-UV double-resonance spectrometer. A detailed analysis of the spectra has provided the hyperfine energy levels with their

quantum number assignment for both these ammonia isotopomers, thereby completing the data set for the symmetric-top ammonia isotopomers, as shown in table 2.1. The behaviour of the manifold of hyperfine levels in external electric fields is calculated, and its implications for molecular beam deceleration and electrostatic trapping experiments are discussed. In particular, it is noted that most hyperfine levels in the upper component of the inversion doublet are exclusively low-field seeking. Molecules in these hyperfine levels can be trapped in regions with a true zero electric field, as potential experimental loss processes due to Majorana transitions are avoided. It is difficult to more generally predict if a certain molecule will have this property in electric fields. A necessary requirement is that the quadratic Stark effect dominates over the linear Stark effect and that at least one of the atoms in the molecule has a nuclear spin. All symmetric-top ammonia isotopomers share this property.

In the present experiments, we have rapidly switched the electric field in the hexapole on and off to achieve a near complete re-distribution of the ammonia molecules over the various hyperfine levels prior to entering the rf-interaction region. This was mainly done to have better defined initial conditions in the microwave experiment, to simplify the interpretation of the experimental data, and to get additional spectroscopic information. By implementing a separate electric field section with time-varying homogeneous electric fields in between the hexapole and the rf-interaction region, transitions between hyperfine levels can be induced in a more controlled way. From the calculated Stark curves it can be deduced which field strengths and switching times are required to optimize or minimize the population re-distribution. It is expected that in this case the re-distribution of the molecules over the various hyperfine levels can be quantitatively understood and controlled. Preparation of a beam of ammonia molecules in selected (subsets of) hyperfine levels, either via controlled re-distribution or via rf-transitions, will be important for future scattering and trapping experiments.

The resolution in the microwave spectra shown in this chapter can still be significantly improved by lengthening the interaction time of the molecules with the rf-radiation. This can be achieved by enlarging the rf-interaction region and/or by reducing the average velocity of the molecular beam. In the next chapter the latter possibility is demonstrated by using a Stark-decelerated beam to study the hyperfine structure of  $^{15}\text{ND}_3$ .





# Chapter 3

## Decelerated molecular beams for high-resolution spectroscopy

### 3.1 Introduction

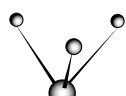
Ultimately, the achievable resolution in any spectroscopic experiment is limited by the interaction time of the particle that is being investigated with the radiation field. This interaction time is determined by the limited size of the interaction region, in combination with the non-zero velocity of the examined particles (see also section 1.1.2). Obviously, the only two ways to increase the interaction time are to either increase the size of the interaction region or to decelerate, or even trap, the particles. The former has been most successfully implemented in Ramsey-type experiments [140]. The obtainable resolution in these experiments is practically only limited by the requirements on the divergence of the (molecular) beams. For atoms, the merits of the second option, i.e., the use of slow particles, have also been shown already. Both samples of trapped atoms, either confined “mechanically” [140] or by electro-magnetic fields [141], and atomic fountains [142, 143] have been used for high-resolution spectroscopy. High-resolution spectroscopic experiments on slow molecules have been performed in the past as well, for instance by selectively probing the slowest sub-set of molecules in a thermal gas-phase sample using Doppler-free two-photon spectroscopy [144, 145]. In this chapter, experiments are described

---

Adapted from:

*Decelerated molecular beams for high-resolution spectroscopy; The hyperfine structure of  $^{15}\text{ND}_3$*

Jacqueline van Veldhoven, Jochen Küpper, Hendrick L. Bethlem, Boris Sartakov, André J. A. van Roij, and Gerard Meijer, *Eur. Phys. J. D* **31**, 337 (2004)



in which molecular beams are actively decelerated for high-resolution spectroscopy for the first time, using a Stark decelerator. Over the last years, our group has developed the Stark-deceleration technique and we have used this to produce cold samples of slow polar molecules [146]. The versatility of the Stark-deceleration technique and the relatively large densities of quantum-state selected slow molecules obtainable with this technique make it a prime method for the preparation of molecular samples for precision spectroscopy. Recently, spectroscopic measurements were performed on Stark-decelerated OH radicals, resulting in the most precise values for the measured transitions so far [17]. Moreover, experiments are currently underway to use Stark-decelerated beams of ground-state YbF molecules for sensitive EDM measurements [107].

In the work presented in this chapter, a beam of  $^{15}\text{ND}_3$  is used that is decelerated to about 52 m/s. For maximum beam intensity in the laser detection region, transverse focusing and spatial re-bunching (longitudinal focusing) of the decelerated beam is applied. Instead of using a specifically designed separate buncher, as was done before [147], bunching is achieved here with the help of the last stages of the Stark decelerator. Together, these improvements have enabled us to completely resolve the hyperfine structure and to determine the energies of all individual hyperfine levels of the  $|J, K\rangle = |1, 1\rangle$  state of  $^{15}\text{ND}_3$  to an absolute accuracy of better than 100 Hz. Before discussing the experimental setup and the measurements, a short description of the operating principle of the Stark decelerator will be given.

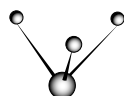
## 3.2 Stark decelerator

Stark decelerators utilize the Stark effect to decelerate polar molecules. The Stark effect is a shift of the energy levels of a molecule as a result of the interaction of its dipole moment with an electric field. The molecule will either lose or gain potential energy with increasing electric field, depending on its initial internal state. Molecules that lose energy are called low-field seekers, as they will always experience a force towards the lowest electric field. Analogously, molecules that gain energy are called high-field seekers, and these molecules experience a force towards the highest electric field (see also figure 2.2 on page 23).

If a low-field-seeking molecule enters a region of increasing electric field, it gains potential energy at the cost of kinetic energy, and the molecule will slow down. This is the effect that is exploited in the Stark decelerator. The region of increasing electric field is generated by a voltage difference between two parallel rods. The rods are oriented perpendicular to the path of the molecule. Along this path, the electric field strength displays a maximum in between the two rods, and a low-field-seeking molecule will therefore decelerate when approaching them. To prevent the molecule from regaining its kinetic energy once it has passed through the rods, the voltages on the rods are abruptly switched off. The maximum attainable electric field strength in between the

rods is on the order of 100 kV/cm. As can be seen from figure 2.2 (page 23), one deceleration stage therefore removes about  $1 \text{ cm}^{-1}$  of energy. As the energy of molecules in a supersonic beam greatly exceeds this value ( $\approx 100 \text{ cm}^{-1}$ ), the process needs to be repeated to be effective. The Stark decelerator consists of an array of electric field stages, as is shown in figure 3.1. Because in the transversal direction the electric field strength is highest at the rods, in one direction molecules are focused towards the central axis of the decelerator. To achieve focusing in both directions, each stage is rotated over  $90^\circ$  with respect to its neighbors (not visible in the figure). All odd stages are electrically connected, as are all even stages. As soon as the voltages on either set of stages are turned off, the voltages on the other set of stages are turned on. This way, the molecules climb the potential hill continuously. In figure 3.1, the potential energy of a molecule in the electric field of the decelerator is shown for both configurations. The most kinetic energy is removed if the molecule is allowed to fly all the way up to the top of the potential hill, before the configurations are switched. It is also possible to switch earlier and remove less energy. In this way, the end velocity of the molecule can be varied. The voltages are switched each time the molecule reaches a certain position with respect to the next set of rods. As a result, the amount of energy that is taken from the molecule is the same for each stage. The position of the molecule at the moment the configurations are switched is indicated by the phase angle, which is defined as  $-90^\circ$  in the middle of two grounded rods and  $90^\circ$  in the middle of the next pair of rods (see also figure 3.1). Using a phase angle of  $53^\circ$ , the thicker parts of the Stark curves in figure 3.1 indicate the regions the molecule traverses in each configuration, before switching to the other configuration. As the molecule slows down throughout its journey through the decelerator, it takes more and more time to reach the next switching point. An entire switching sequence, therefore, looks like is shown in the lower part of figure 3.2. In the upper part, the time intervals between switching can be seen.

Of course, more than one molecule is present in a supersonic beam, which is used as the source of molecules for the decelerator, and each has its own initial position and velocity. The molecule discussed in the previous paragraph is called the synchronous molecule, and is defined as that molecule that loses the same amount of energy in each stage. Molecules with a higher initial velocity than this molecule will fly higher up the potential hill in each deceleration stage and will lose more kinetic energy. They will therefore slow down with respect to the synchronous molecule. Eventually they will be slower, will lose less energy in each deceleration stage, and will speed up with respect to the synchronous molecule again. From these arguments, it can be seen that the velocity of such a molecule oscillates around the velocity of the synchronous molecule. A similar argument can be made for molecules with a position close to that of the synchronous molecule. This principle is called phase stability. The initial position or velocity of the molecule needs to be close enough to that of the synchronous molecule, however. The higher the phase angle (more de-



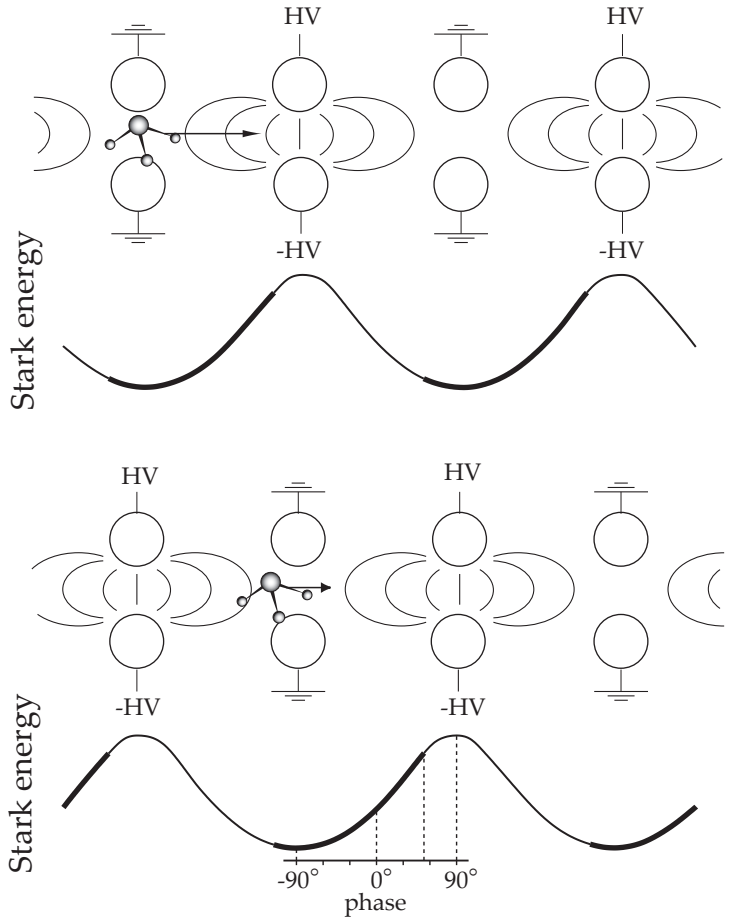


Figure 3.1: A molecule flying through the decelerator. The array of rods that comprise the decelerator is shown twice, once with voltage applied to the odd sets of rods, and once to the even sets. Between the rods a few lines of constant electric field strength are indicated. Below the decelerators, the Stark energy of a molecule flying through is given. If a time sequence with a phase angle of  $53^\circ$  is used to determine the switching times, the synchronous molecule traverses the regions indicated by the thicker lines during the time each configuration is turned on.

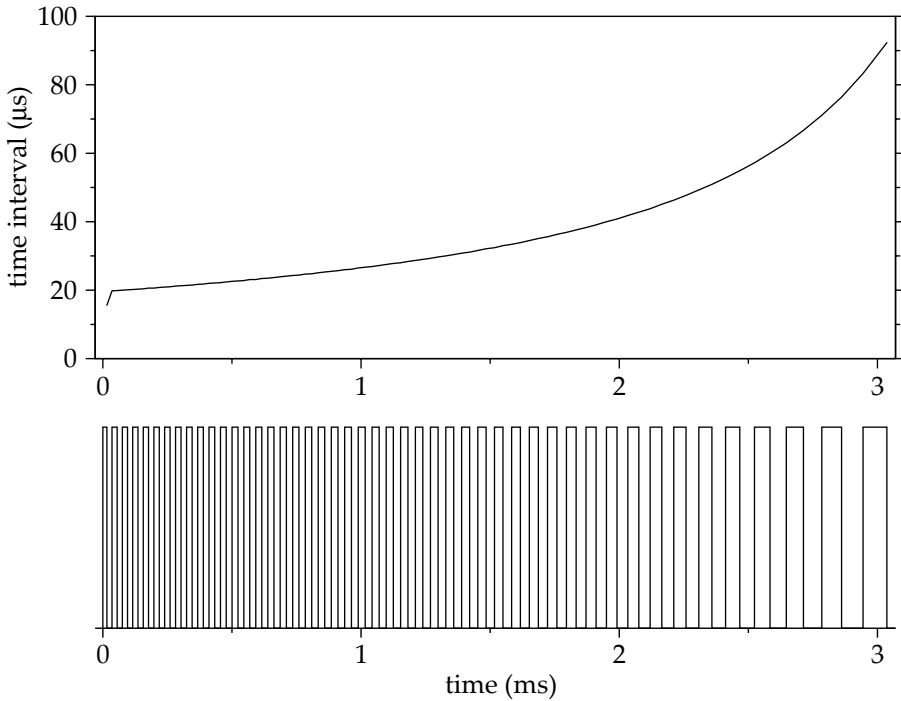
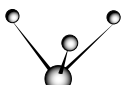


Figure 3.2: In the lower part of the graph, a schematic view of an actual time sequence is shown. This time sequence can be used to decelerate a beam of  $^{14}\text{ND}_3$  molecules from 280 to 46 m/s ( $\phi = 53^\circ$ ). Whenever the line moves from high to low, or vice versa, the voltages are switched. In the upper part of the graph, the time intervals between switching are shown. At later times, the intervals become longer, as the molecules slow down, and therefore take more time to reach the next deceleration stage.

celeration), the smaller the region in position-velocity space (phase space) that is phase-stable. Choosing a phase angle is therefore always a trade-off between deceleration to the lowest velocities and deceleration of the most molecules. For a more detailed description of the Stark decelerator in general, see [146], and of Stark deceleration of a pulsed molecular beam of ammonia in particular, see [148].

### 3.3 Experimental

The experiments are performed in a differentially pumped pulsed molecular beam setup, operated at a 10 Hz repetition frequency, depicted in figure 3.3.



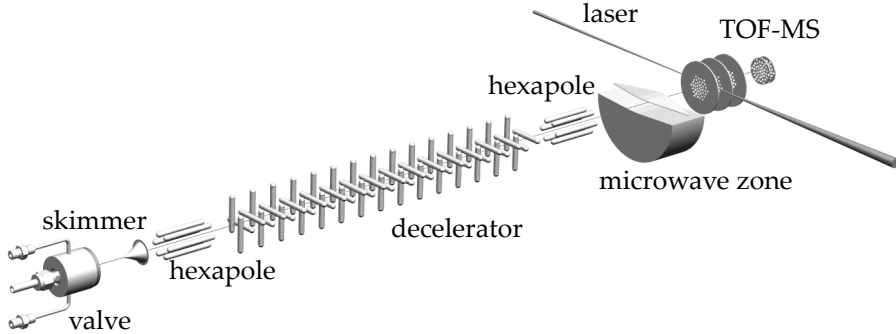


Figure 3.3: Experimental setup. The setup consists, from left to right, of a pulsed valve to produce a supersonic jet, a skimmer, a hexapole, the Stark decelerator, another hexapole, the microwave zone, and a laser-ionization/TOF-detector. The whole setup is mounted in a differentially pumped vacuum system.

In the source chamber a mixture of typically 5%  $^{14}\text{ND}_3$  or  $^{15}\text{ND}_3$  in xenon is expanded from 2 bar into vacuum through a pulsed valve (modified General Valve, Series 9) with a 0.8 mm diameter orifice, creating a  $\sim 100 \mu\text{s}$ -duration gas pulse. The source chamber is pumped by a 500 l/s turbo-molecular pump (Balzer TPU 500) backed by a rotary pump (Alcatel 2033) and the resulting operating pressure is typically  $2 \cdot 10^{-6}$  mbar. The nozzle is cooled to  $-70^\circ\text{C}$ , resulting in a beam with a mean velocity of about 280 m/s. In the molecular beam all para-ammonia molecules, i.e., about 60% of all  $\text{ND}_3$  molecules, reside in the  $|J, K\rangle = |1, 1\rangle$  inversion doublet, the ground state of para ammonia.

Some 35 mm downstream from the nozzle a 1.5 mm diameter skimmer separates the source chamber from the deceleration chamber. This second chamber is also pumped by a 500 l/s turbo-molecular pump (Balzer TPU 500) and is backed by the same rotary pump as the source chamber, resulting in an operating pressure of  $5 \cdot 10^{-8}$  mbar. After another 35 mm the beam passes through a 60 mm long hexapole consisting of six 3 mm-diameter rods placed equidistantly on the outside of a circle with a radius of 3 mm. Three alternating rods of this hexapole can be switched to high voltage, typically 10 kV, while the other set of three rods is connected to ground. The hexapole acts as a positive lens for ammonia molecules in the low-field-seeking hyperfine components in the upper level of the inversion doublet of the  $|J, K\rangle = |1, 1\rangle$  state.

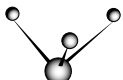
After exiting the hexapole, the molecules enter the decelerator; the first set of electrodes of the decelerator is positioned about 14 mm behind the hexapole. The decelerator used in these experiments consists of 95 sets of parallel electrodes, with a separation of 2 mm between the two electrodes in each set. Each electrode has a diameter of 3 mm and is mounted in the plane perpendicular

to the beam axis. The shortest distance between electrodes in adjacent sets is 2.5 mm and each set is rotated over 90° about the beam axis with respect to its neighbors. Within each set one electrode is switched to +10 kV, while the other one is switched to -10 kV.

In most deceleration experiments that have been performed thus far, the entire length of the decelerator is used to slow a packet of state-selected molecules from the initial velocity, normally the mean velocity of the incoming beam, to the desired final velocity. To increase the peak density in the detection region, here we use the last stages of the decelerator for spatial re-bunching, or longitudinal spatial focusing, instead. Thus, (part of) the pulsed ammonia beam is decelerated from 280 m/s to 52 m/s using only the first 86 stages of the decelerator. Subsequently, the packet is allowed to stretch along the molecular beam axis during a free-flight distance of 39.5 mm inside the decelerator; during free flight only a bias voltage of 300 V is applied to the positive electrodes, to prevent Majorana transitions. In the last stage of the decelerator the decelerated packet is then re-bunched to obtain a longitudinal spatial focus in the detection region. This type of re-bunching is very similar to the bunching reported by our group before [147], with the only important difference that in the present experiments the last stage of the decelerator is used, instead of a separate, dedicated buncher. Since the sets of electrodes in the decelerator are hardwired together, we use the same field-strength in the bunching section as in the deceleration stages. To nevertheless obtain the appropriate longitudinal focusing strength, the time during which the bunching section is on is varied, rather than the electric field strength, as was done before [147].

For transverse focusing of the decelerated molecular beam in the detection region, a second hexapole is mounted 10 mm downstream from the decelerator. This hexapole consists of six 4 mm-diameter, 30 mm long rods mounted on the outside of a circle with a radius of 4 mm. Here, alternating rods are switched to +10 kV and -10 kV. This hexapole is mechanically larger to accept more molecules from the decelerator. The use of both polarity high voltages allows to completely focus the decelerated beam even when the hexapole is only on for 40  $\mu$ s, corresponding to an effective thickness of the lens as experienced by the decelerated molecules of only 2 mm. By varying the time at which this hexapole is switched on and off, the position of this thin last focusing lens can be effectively moved along the molecular beam axis over almost the complete length of the hexapole.

In both hexapoles as well as in the decelerator, molecules with a positive Stark effect, which reside in the upper component of the inversion doublet (in  $MK = -1$  states), are transversally focused, whereas molecules in states with a negative Stark effect, which reside in the lower component of the inversion doublet (in  $MK = 1$  states), are defocused. Molecules in states with  $MK = 0$  (unshifted levels) have a small Stark shift and are not affected much by the electric fields. As a result, almost exclusively ammonia molecules that reside in low-field-seeking hyperfine states of the  $|J, K\rangle = |1, 1\rangle$  inversion doublet



exit the decelerator, and almost complete population inversion exists in the produced decelerated beam upon entering the microwave zone. The 100 mm long microwave zone, placed 10 mm behind the second hexapole, provides a nearly rectangular field strength distribution along the molecular beam axis with a width (FWHM) of about 65 mm. A cw signal generator (Rohde & Schwarz SMR20) is used to generate the radiation that is needed to induce the inversion tunneling transition of  $^{15}\text{ND}_3$  at 1.43 GHz. The synthesizer has a resolution of 0.1 Hz and a quoted stability of  $10^{-6}/\text{year}$ . The absolute frequency of the signal generator was tested against the 10 MHz signal of a DCF77 receiver several times during the measurement period by means of a frequency counter (Auerswald FZ-1310) and is found to be better than  $10^{-8}$ , the accuracy of the counter. For 0 dBm incoupling power the field strength on the molecular beam axis is 20 V/m. The experiments are typically performed at power-settings of -30 dBm (0.6 V/m) to -20 dBm (2 V/m) on the microwave synthesizer. Losses due to cabling and connectors are around 1 dBm.

About 50 mm downstream from the exit of the microwave zone molecules are detected using laser ionization and ion detection in a home-built time-of-flight mass spectrometer. A frequency doubled Nd:YAG laser (40% power of a Spectra-Physics Quanta-Ray Pro 230-10) is used to pump a dye laser (Radiant NarrowScan) operating with DCM. The output of the dye laser is frequency doubled in a KDP crystal, resulting in typical energies of 15 mJ/pulse at 317 nm with a linewidth of  $0.05 \text{ cm}^{-1}$ . The tunable UV light is focused into the detection region using a 500 mm focal length lens. The laser beam crosses the molecular beam perpendicularly, and the photoions are extracted coaxially with respect to the molecular beam. The UV-laser based (2+1)-Resonance Enhanced Multi-Photon Ionization (REMPI) scheme enables state-selective detection of the  $^{15}\text{ND}_3$  molecules [137] (see also figure 2.5 on page 27). In the microwave experiments, the UV-laser frequency is kept constant while the microwave frequency is scanned. If the UV laser is tuned to ionize molecules in the upper component of the inversion doublet, a resonance of the microwave radiation will result in a decrease in ion signal; if the laser is tuned to ionize molecules in the lower component of the inversion doublet, a resonance of the microwave radiation will result in an increase in ion signal. The latter detection scheme has the advantage that it is (almost) background free, and it is the detection scheme that is used for measuring the microwave spectra reported here.

## 3.4 Results and Discussion

### 3.4.1 Deceleration and bunching

In figure 3.4, time-of-flight profiles of  $^{14}\text{ND}_3$  are shown as obtained using the setup described above without the microwave zone, i.e., with the laser detection

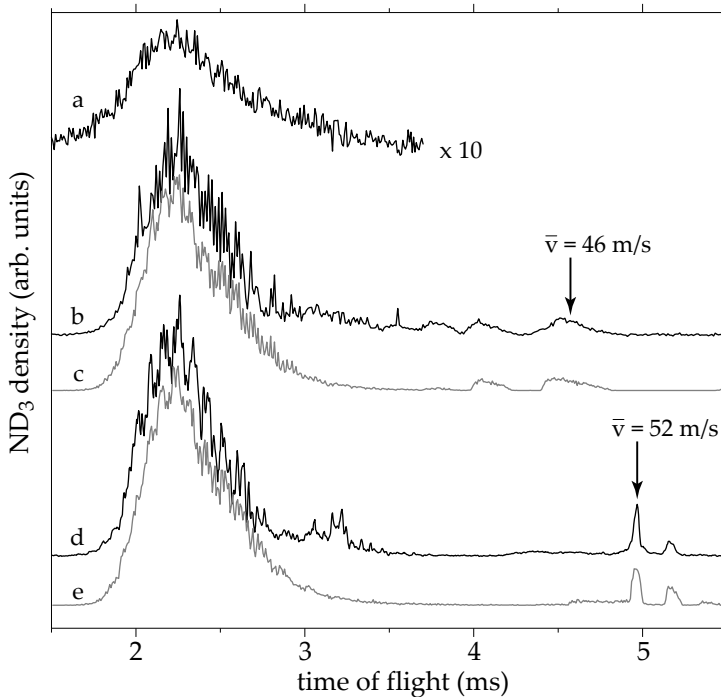
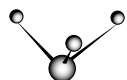


Figure 3.4: Observed and calculated time-of-flight distributions of ammonia; the different traces have been given an offset for clarity. (a) shows a measurement of the original molecular beam without electric fields. (b) gives a time profile for a deceleration experiment using all stages for deceleration while (c) shows the results of the corresponding trajectory simulation. (d) gives a time-profile for a deceleration experiment with longitudinal spatial focusing of the beam in the detection zone, (e) shows the results of the corresponding trajectory simulation.



region directly behind the second hexapole. Trace (a) shows a time-of-flight profile of  $^{14}\text{ND}_3$  obtained without any electric fields. The measurement shows a broad distribution around a mean arrival time of 2.3 ms, corresponding to an average forward velocity of 280 m/s. The full width at half maximum (FWHM) of the velocity distribution is seen to be around 60 m/s, corresponding to a translational temperature of about 1.6 K in the moving frame of the molecular beam. With the electric fields in the decelerator and hexapoles switched such as to decelerate the central part of the original beam from 280 m/s to about 46 m/s, the time-of-flight distribution shown in trace (b) is obtained. In this case, all stages of the decelerator are used for actual deceleration, i.e., a constant phase-angle of  $\phi = 53^\circ$  is used for deceleration throughout the decelerator, and in each of the 94 stages of the decelerator about  $0.68 \text{ cm}^{-1}$  of kinetic energy is removed from the accepted bunch of ammonia molecules. Due to the residual velocity spread of the packet leaving the decelerator, the arrival time distribution of the packet in the detection region is relatively broad. A one-dimensional simulation of the time-of-flight profile of this measurement is given in trace (c). A bunch of molecules captured one stable ‘bucket’ ahead of the main packet, containing the synchronous molecule, is visible as well. The relatively long opening time of the pulsed valve (100  $\mu\text{s}$ ) results in a packet of molecules at the entrance of the decelerator with a length of several centimeters. Therefore, some molecules from the original beam are already two stages (one period) ahead inside the decelerator at the time when the burst sequence for the synchronous molecules starts. When those molecules are in the right velocity interval around 280 m/s they are captured by the electric fields as well and are (phase-stably) transported through the decelerator while staying two stages ahead. Consequently, they leave the decelerator earlier, and do not experience the last two switching processes, since by then they are already outside the electrode array. Overall, this packet of molecules is 11 mm ahead of the synchronous packet and is traveling at a higher final velocity (around 61 m/s, instead of 46 m/s), resulting in a correspondingly earlier arrival time at the detection region. Similarly, there is also a packet traveling 11 mm behind the main bunch. Molecules in this packet were still in front of the decelerator when the burst sequence started, and they only entered the decelerator when the main bunch was already two stages (one period) further. In order to be captured by the decelerator, these molecules must have an initial velocity that is slightly slower, around 277 m/s, since by the time these molecules enter the decelerator the electric fields have already been switched twice for the main bunch. If the switching of the fields in the decelerator is stopped when the main bunch exits, the packet trailing by 11 mm is decelerated to the same final velocity as the main bunch and is detected at a time delay after the main bunch directly reflecting the 11 mm spatial lag. If the switching of the fields is continued after the main bunch has already exited the decelerator, as is done for the experiments shown in figure 3.4b, the packet lagging behind is decelerated further, resulting in it being so slow and with such a wide arrival-time

distribution that it is not observed at all. In addition, the second hexapole is switched such that it almost exclusively transversally focuses the main bunch.

To increase the peak density of the slow molecules in the detection region, one can perform re-bunching, or longitudinal spatial focusing, of the decelerated bunch [147]. In the experiments performed here the last stage of the decelerator is used as a buncher. For this, a time sequence is applied that decelerates the main bunch from 280 m/s to 52 m/s using only the first 86 stages of the decelerator. This means that the first 86 stages of the decelerator are operated at a constant (higher) phase-angle of  $\phi = 58^\circ$ , removing  $0.74 \text{ cm}^{-1}$  kinetic energy from the ammonia molecules per stage. After this, the decelerated packet is allowed to longitudinally stretch in free flight in the next 7 stages. The last stage of the decelerator is then switched on for a time duration of  $50 \mu\text{s}$ , to obtain a longitudinal spatial focus in the laser detection region. This last stage of the decelerator is switched such as to leave the velocity of the synchronous molecules unchanged, i.e., at phase-angle  $\phi = 0^\circ$ . The total free flight distance in the decelerator is then 39.5 mm, and during this free flight only a very weak electric field is present inside the decelerator to prevent Majorana transitions. The observed time-of-flight distribution for the decelerated and bunched ammonia molecules is shown in figure 3.4, in trace (d). The corresponding trajectory simulation is shown directly underneath, in trace (e). Due to the necessarily higher phase angle for deceleration in this combined deceleration and bunching scheme, effectively less molecules are captured in the decelerator. Additionally, there are some losses during free flight between deceleration and re-bunching due to the velocity spread and absence of transverse focusing. Nonetheless, the peak-intensity of the main bunch in the detection region is more than two times larger than in the normal deceleration experiment without re-bunching. As the microwave-UV double-resonance experiments reported here are performed at a fixed timing of the UV laser, the experiments are sensitive to the peak intensity and not to the time-integrated intensity, and this increase by a factor two in peak-intensity is very favorable. In this combined deceleration and bunching scheme as well, there are decelerated packets on either side of the main bunch. The packet running ahead is hardly visible because it is not re-bunched, as it had already left the decelerator at the time that the buncher was switched on. Due to its long free flight distance this packet becomes spread out considerably and is barely recognizable due to its very broad arrival time distribution. The packet running 11 mm behind is re-bunched analogously to the main packet and this results in a spatial focus 11 mm before the laser detection region. After this focus the packet of molecules starts to spread out again and in the detection region its arrival time distribution is already significantly wider, resulting in a reduced peak intensity.

In all the microwave-UV double-resonance experiments reported here a time sequence equivalent to the one used in trace (d) of figure 3.4 is employed. Laser ionization is performed at the peak of the arrival time distribution of the main bunch, thus always detecting ammonia molecules with a velocity of  $52 \pm 3.5 \text{ m/s}$ .



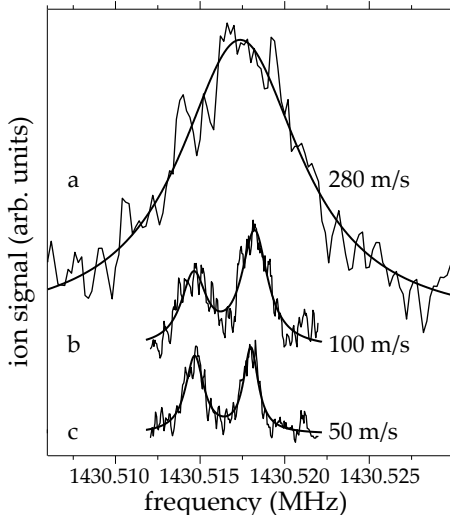


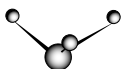
Figure 3.5: The  $20 \rightarrow 3$  and  $21 \rightarrow 2$  transition of  $^{15}\text{ND}_3$  recorded in a molecular beam with velocities as indicated. With reduced beam velocities the linewidth decreases from about 10 kHz to about 1 kHz, as determined from fitted Lorentzian line-profiles. The labeling of the lines refers to the numbering of the hyperfine levels as given in figure 3.7.

### 3.4.2 Microwave inversion spectrum

To demonstrate the transit-time limitation of the spectral resolution of the microwave inversion spectrum of  $^{15}\text{ND}_3$ , a sparse section of the spectrum is recorded using molecular beams with different velocities. In figure 3.5 the highest-frequency part of the microwave spectrum is shown for three different velocities. In the measured frequency range there are two transitions with considerable transition strength and a doublet of lines can therefore be expected. The upper trace in figure 3.5 is measured at 280 m/s, which is, as mentioned earlier, the slowest possible velocity for a molecular beam using ‘conventional’ means. The measurement is performed at sufficiently low microwave power (-25 dBm, 1 V/m) to avoid power-broadening. Only a single broad line with a spectral width of 8.7 kHz (FWHM) is observed. In the middle trace the same measurement (-30 dBm, 0.6 V/m) is performed for an ammonia beam that is decelerated to 100 m/s, resulting in a considerably decreased spectral width of approximately 2 kHz. The lowest trace then is the measurement for a beam with a mean velocity of 52 m/s (-30 dBm, 0.6 V/m), resulting in two baseline separated lines with a width of 1.3 and 1.0 kHz, respectively. These linewidths are deduced from fitting a Lorentzian line shape to the data, as is shown in figure 3.5. In the case of a rectangular microwave field with a width

of 65 mm a  $(\sin(x)/x)^2$  line shape with a width (FWHM) of 710 Hz is expected due to transit-time broadening [149]. Deviations from a rectangular field in combination with residual power broadening lead to the observed line profiles. It is under these conditions, under which the hyperfine structure can be fully resolved, that the whole inversion spectrum of  $^{15}\text{ND}_3$  in the  $|J, K\rangle = |1, 1\rangle$  state is measured.

In figure 3.6, the pure inversion spectrum of  $^{15}\text{ND}_3$  in its  $|J, K\rangle = |1, 1\rangle$  state is shown for different velocities and for different microwave powers. The spectra shown in traces (b) and (c) are obtained in steps of 100 Hz in the microwave frequency. At each step, the microwave frequency is held fixed to record the ion signal, which is determined as the average of 200 ion-count measurements obtained at the 10 Hz pulse rate of the ionization laser. The spectra shown in traces (b) and (c) of figure 3.5 are measured under the same conditions. Trace (a) shows the microwave spectrum as measured in a molecular beam with a mean velocity of 280 m/s, using -20 dBm (2 V/m) of microwave power. The linewidth is about 10 kHz, only slightly better than in the spectra reported in chapter 2. Although the sub-structure due to the hyperfine splitting can clearly be recognized in this spectrum and several distinct features can be observed, a further assignment based on this spectrum alone is not possible. In chapter 2 a tentative assignment of this spectrum is given, based on scaling the hyperfine interaction parameters deduced for  $^{14}\text{ND}_3$ . Contrary to the situation in  $^{14}\text{ND}_3$ , where the quadrupole moment of the  $^{14}\text{N}$  nucleus gives rise to readily recognizable splittings in the microwave spectrum, it is not possible to unambiguously identify groups of lines in the microwave spectrum of  $^{15}\text{ND}_3$  at this relatively low spectral resolution. Trace (b) shows the microwave spectrum as measured in a decelerated beam with a mean velocity of 52 m/s, using -20 dBm (2 V/m) of microwave power. It is evident that the spectral resolution of selected individual lines is largely improved relative to the spectrum shown in the upper trace, and many identifiable resonances appear in the spectrum. The strong lines in this spectrum are saturated, however, and, apart from power-broadening, this results in numerous extra lines in the spectrum due to multiple down-up-down Rabi-cycling transitions between hyperfine levels in the upper and lower components of the inversion doublet. This ‘high power’ spectrum of the decelerated beam is therefore mainly useful to identify the weak lines in the inversion spectrum. The central part of the microwave spectrum, which contains the strongest inversion transitions, is measured once more with a reduced microwave power. The measured spectrum as recorded with -30 dBm (0.6 V/m) of microwave power, under otherwise identical conditions, is shown in trace (c). In the spectrum several well-resolved strong lines with a linewidth of 1 kHz are observed. The weak lines in the wings of the spectral range shown in trace (b) together with the strong lines shown in trace (c) yield the complete hyperfine resolved microwave inversion spectrum of  $^{15}\text{ND}_3$  in the  $|J, K\rangle = |1, 1\rangle$  state. In trace (d), the best fitting simulated spectrum is shown, convoluted with a Lorentzian line shape function with a width (FWHM) of 1 kHz.



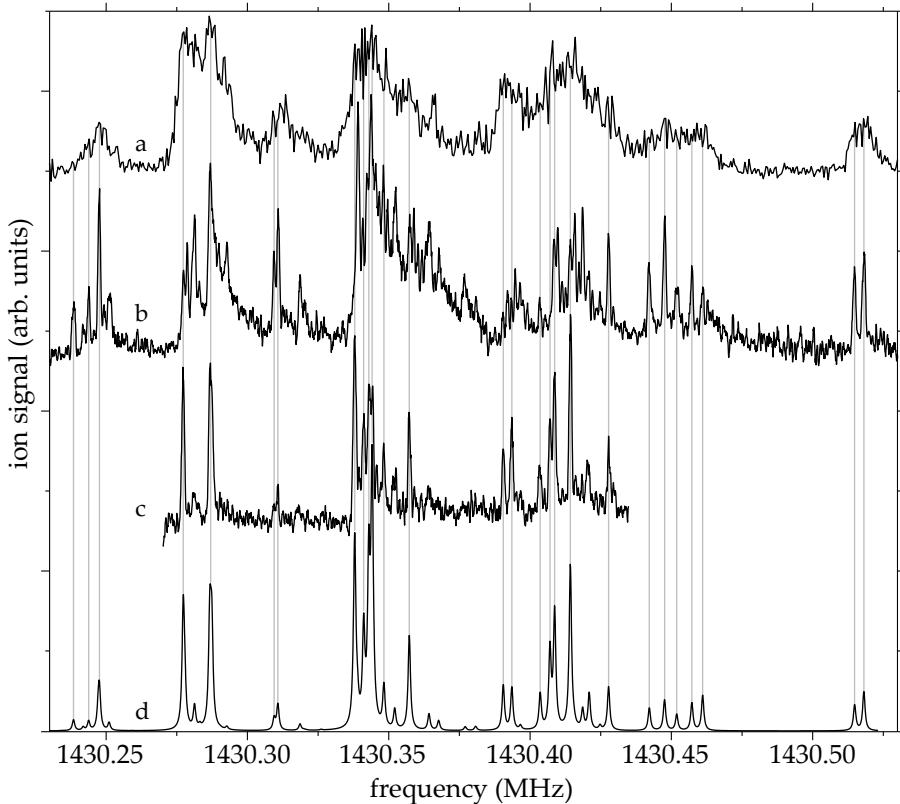


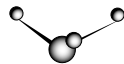
Figure 3.6: Microwave inversion spectrum of  $^{15}\text{ND}_3$  in the  $|J, K\rangle = |1, 1\rangle$  state. Trace (a) shows the spectrum as measured in a beam with a mean velocity of 280 m/s, using -20 dBm (2 V/m in the microwave zone) of microwave power. Trace (b) shows the corresponding measurement for a decelerated beam with a mean velocity of 52 m/s, using -20 dBm (2 V/m) of microwave power. In this spectrum many resonances appear due to multiple down-up-down Rabi-cycling transitions between the upper and lower inversion components. Trace (c) shows the measurement in the decelerated beam at reduced microwave power, -30 dBm (0.6 V/m), under otherwise identical conditions. In trace (d) the theoretically simulated spectrum, convoluted with a Lorentzian line shape function with a width (FWHM) of 1 kHz, is shown.

The simulation of the microwave spectrum covers all the symmetric-top isotopomers of ammonia ( $^{14}\text{NH}_3$ ,  $^{15}\text{NH}_3$ ,  $^{14}\text{ND}_3$ ,  $^{15}\text{ND}_3$ ) through a generalized tensor coupling scheme [150] (see also chapter 2). This enables testing of the simulations against the experimentally well characterized  $^{14}\text{NH}_3$  system [24]. A detailed description of the formalism that is used is given in the appendix of [138]. For the description of the hyperfine interaction twelve parameters are used. The overall tunneling splitting of the  $|J, K\rangle = |1, 1\rangle$  rotational state is given by the parameter  $c_t$ . The interaction between the overall rotation and the nuclear spin of  $^{15}\text{N}$  is described by the parameters  $c_{JN1}$  and  $c_{JN2}$ ; there are two parameters since the rotation around the parallel and the perpendicular axes of the symmetric top couple differently to the nuclear spin. The analogous interaction between the overall rotation and the nuclear spin of the deuterium nuclei is described by the parameters  $c_{JD1}$ ,  $c_{JD2}$ , and  $c_{JD3}$ ; in this case three parameters are required, since the deuterium atoms are located away from the symmetry axis of ammonia. The coupling between the nuclear spin of  $^{15}\text{N}$  and the nuclear spin of the deuterium nuclei is described by the parameters  $c_{ND1}$  and  $c_{ND2}$  and the coupling among the different nuclear spins of deuterium is described by the parameters  $c_{DD1}$  and  $c_{DD2}$ . Finally, the two parameters  $c_{QD1}$  and  $c_{QD2}$  describe the interaction between the molecule-fixed electronic wavefunction and the laboratory-frame fixed quadrupole moments of the deuterium atoms.

As we have obtained high-resolution microwave spectra for  $^{15}\text{ND}_3$  in a single rovibrational state only, the parameters  $c_{JN1}$  and  $c_{JN2}$  cannot be determined independently; one can only determine a line in  $c_{JN1}$ ,  $c_{JN2}$  space with an *a priori* known slope, and thus the value of  $c_{JN1} - c_{JN2}/(2\sqrt{10})$  is fitted. Different rotational states have different slopes for this line, i.e., different linear combinations can be fitted, from which then the absolute values of the individual parameters  $c_{JN1}$  and  $c_{JN2}$  can be determined. Similarly, we cannot determine the parameters  $c_{JD1}$  and  $c_{JD2}$  separately, but their linear combination  $c_{JD1} - c_{JD2}/(2\sqrt{10})$  can be extracted from the available data<sup>1</sup>. Therefore, in the fit to the experimental spectrum ten free (combinations of) parameters are adjusted.

The values obtained for these ten parameters from a least-squares fit of the Hamiltonian to the experimental transition frequencies are given in table 3.4.2 (for comparison, see table 2.1 on page 34). In the fit 27 experimental transition frequencies are included and the resulting  $1\sigma$  standard deviations are given in parentheses behind the parameter values. Parameters are given with the precision necessary to recalculate the line positions from the given data to within 10% of their standard deviation [151]. The assignment of these 27 transitions together with the experimentally observed and calculated transition frequencies are given in table 3.2. In this assignment the labeling of the hyperfine

<sup>1</sup>Note that in chapter 2, most of these parameters were not fitted, because of the lower resolution of the measured spectra. Instead, parameters were scaled to values from  $\text{NH}_3$ .



parameter	T.&S. [23]	$^{15}\text{ND}_3$ (kHz)
$c_t$	$\Omega_t$	1430335.66 (2)
$c_{JN1} - c_{JN2}/(2\sqrt{10})$	$-\frac{\sqrt{3}}{2}(a + b)$	8.16 (6)
$c_{JD1} - c_{JD2}/(2\sqrt{10})$	$-\frac{\sqrt{3}}{2}(2A + C)$	4.38 (3)
$c_{JD3}$	$\sqrt{30}B$	6.45 (10)
$c_{ND1}$	$-3\sqrt{10}D_1$	-4.74 (27)
$c_{ND2}$	$\sqrt{30}D_2$	11.62 (15)
$c_{DD1}$	$3\sqrt{5/2}D_3$	3.40 (22)
$c_{DD2}$	-	5.08 (11)
$c_{QD1}$	-	-227.28 (25)
$c_{QD2}$	-	432.72 (11)

Table 3.1: Adjustable parameters in the Hamiltonian, together with their correspondence to parameters in the more commonly used notation from Townes & Schawlow [23]. The values (in kHz) are obtained from the best fit to the experimentally observed transition frequencies. A total of 27 transitions are included in the fit and the overall standard deviation of the fit is 62 Hz. The number in parenthesis is the  $1\sigma$  standard deviation in the last digit(s). For comparison, see table 2.1 on page 34.

levels as given in figure 3.7 is used. The average difference between observed and calculated frequencies is 62 Hz.

The resulting energy-level structure of the inversion doublet of  $^{15}\text{ND}_3$  in the  $|J, K\rangle = |1, 1\rangle$  state and the Stark curves for these states are shown in figure 3.7. Zero energy is chosen at the energy of the lower inversion substate with all interactions switched off, i.e., with all parameters in table 3.4.2 except  $c_t$  set to zero. In zero electric field both the lower ( $s$ ) and the upper ( $a$ ) inversion substate, corresponding to the symmetric and antisymmetric linear combination of the infinite-barrier states, respectively, split up into eleven hyperfine levels, labeled 1-22 with increasing energy. Knowing the interaction parameters for  $^{15}\text{ND}_3$  in the  $|J, K\rangle = |1, 1\rangle$  state, the behavior of the hyperfine manifold in external fields can be calculated using the same tensor coupling scheme. The dipole moment of  $^{15}\text{ND}_3$  is taken as  $\mu = 1.48$  D [152]. The energies of all states in zero field are explicitly given in table 3.3, together with the number of  $M_F$ -components that are high-field seeking in the  $s$ -substate and low-field seeking in the  $a$ -substate; the remaining states are not much effected by the electric field.

It is noteworthy that most hyperfine-levels in the upper component of the inversion doublet are exclusively low-field seeking and molecules in these levels can therefore be trapped in field-free regions without potential losses due to Majorana transitions (see also section 2.3.3).

In the simulated spectrum shown in the lower trace in figure 3.6, the relative

transition	exp. (kHz)	calc. (kHz)	$\Delta$ (kHz)
17→ 11	1430238.50	1430238.46	0.039
18→ 11	1430243.85	1430243.82	0.032
19→ 11	1430247.57	1430247.64	-0.071
16→ 8	1430277.25	1430277.29	-0.039
19→ 9	1430287.06	1430286.99	0.072
17→ 7	1430309.39	1430309.44	-0.046
16→ 6	1430310.77	1430310.77	0.001
21→ 11	1430337.97	1430337.97	-0.005
20→ 10	1430341.16	1430341.13	0.031
17→ 5	1430343.09	1430342.94	0.153
16→ 4	1430344.24	1430344.12	0.123
18→ 5	1430348.25	1430348.29	-0.044
19→ 4	1430357.26	1430357.27	-0.014
14→ 2	1430390.56	1430390.53	0.033
15→ 3	1430393.52	1430393.56	-0.037
22→ 9	1430403.48	1430403.59	-0.108
22→ 8	1430407.07	1430407.05	0.025
20→ 7	1430408.65	1430408.69	-0.037
21→ 6	1430414.30	1430414.26	0.041
19→ 2	1430427.85	1430427.79	0.058
20→ 5	1430442.13	1430442.19	-0.057
21→ 4	1430447.63	1430447.61	0.023
17→ 1	1430451.99	1430451.89	0.096
18→ 1	1430457.27	1430457.25	0.019
19→ 1	1430460.97	1430461.07	-0.104
20→ 3	1430514.80	1430514.83	-0.026
21→ 2	1430518.14	1430518.13	0.014

Table 3.2: Experimentally observed and calculated transition frequencies. The labeling of the lines refers to the numbering of the hyperfine levels as given in figure 3.7. In the last column the difference  $\Delta$  between observed and calculated transition frequencies is given.



s-level						
label	$F_1$	$I_D$	$F$	energy (kHz)	levels shifted	
1	3/2	1	1/2	-117.92 (4)	all	
2	3/2	2	5/2	-84.64 (3)	all	
3	3/2	2	3/2	-81.60 (3)	all	
4	3/2	1	5/2	-14.12 (2)	all	
5	1/2	1	3/2	-8.96 (3)	all	
6	3/2	2	7/2	19.23 (2)	all	
7	1/2	2	5/2	24.55 (3)	2	
8	3/2	1	3/2	52.71 (4)	0	
9	1/2	1	1/2	56.17 (5)	0	
10	3/2	2	1/2	92.10 (3)	0	
11	1/2	2	3/2	95.51 (3)	0	
a-level						
12	3/2	1	3/2	1430195.18 (12)	0	
13	3/2	2	1/2	1430195.80 (12)	0	
14	3/2	2	7/2	1430305.89 (3)	2	
15	1/2	2	5/2	1430311.96 (3)	2	
16	3/2	1	5/2	1430330.00 (3)	all	
17	3/2	1	3/2	1430333.97 (2)	all	
18	3/2	2	1/2	1430339.33 (3)	all	
19	1/2	1	3/2	1430343.15 (3)	all	
20	1/2	2	3/2	1430433.23 (4)	all	
21	3/2	2	5/2	1430433.49 (3)	all	
22	3/2	1	1/2	1430459.76 (6)	all	

Table 3.3: Hyperfine energy levels for  $^{15}\text{ND}_3$  ( $|J, K\rangle = |1, 1\rangle$ ) as obtained from the best fit to the experimental data; in parentheses the  $1\sigma$  standard deviation of the relative energy is given.  $F_1$  is the vectorial sum of the overall rotation and the nitrogen nuclear spin,  $I_D$  is the angular momentum due to deuterium nuclear spin, and  $F$  is the overall angular momentum. For each hyperfine level, the number of  $M_F$  components that is shifted – downwards in the *s*-symmetry level and upwards in the *a*-symmetry level – is indicated.

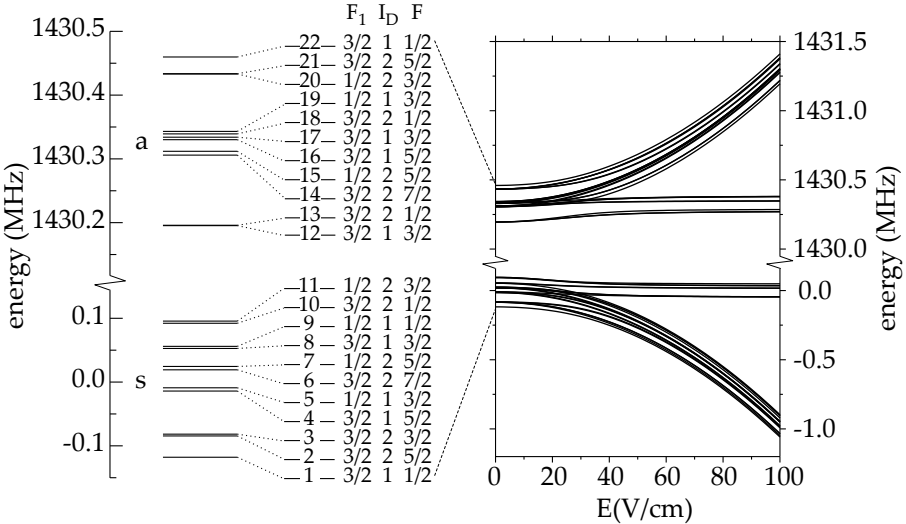


Figure 3.7: Labeling and quantum-number assignment of the 22 hyperfine levels in the  $|J, K\rangle = |1, 1\rangle$  state of  $^{15}\text{ND}_3$ .  $F_1$  is the vectorial sum of the overall rotation and the nitrogen nuclear spin,  $I_D$  is the angular momentum due to deuterium nuclear spin, and  $F$  is the overall angular momentum. On the right-hand side the Stark-shifted hyperfine levels of  $^{15}\text{ND}_3$  in the  $|J, K\rangle = |1, 1\rangle$  state are shown in electric fields up to 100 V/cm. Note that the scale is broken between the two groups of levels, i.e., that the inversion splitting is not drawn to scale.

line intensities are calculated under the assumption that upon entering the microwave zone, the population is equally distributed over all the low-field-seeking hyperfine levels in the  $|J, K\rangle = |1, 1\rangle$  state of  $^{15}\text{ND}_3$ , and that no population is present in any of the other hyperfine levels. This is substantiated by the experiments, as at the predicted microwave frequencies no transitions are observed from the hyperfine levels 12 and 13, which both hardly shift when an electric field is applied (see table 3.3). For the hyperfine levels 14 and 15, of which only some  $M_F$  components are high-field seeking, the zero-field population is taken to be equal to the fraction of low-field-seeking  $M_F$  components, i.e., the population is taken to be 0.25 for level 14 (2 out of 8  $M_F$  components are low-field seeking) and 0.33 for level 15 (2 out of 6  $M_F$  components are low-field seeking). The excellent agreement that is obtained between the observed spectrum and the calculated spectrum, both in line positions and in line intensities, positively demonstrates that there is apparently no further scrambling of the hyperfine levels of the molecules that are focused in the microwave zone. It also demonstrates that there is no observable dependence of the UV-laser based ionization



detection scheme on the hyperfine levels of  $^{15}\text{ND}_3$ , and that the observed relative ion intensities on the various microwave transitions directly reproduce the microwave transition intensities.

### 3.5 Conclusions

In this chapter, the use of a decelerated and transversally and longitudinally focused molecular beam has been demonstrated for high-resolution spectroscopy. In a pulsed beam of  $^{15}\text{ND}_3$ , decelerated to 52 m/s, the hyperfine structure of the inversion doubling transition in the  $|J, K\rangle = |1, 1\rangle$  state around 1.43 GHz is completely resolved. The transit-time limited linewidths in the microwave-UV double-resonance experiments are about 1 kHz, and the standard deviation from the best-fitting simulated spectrum is 62 Hz. All 22 individual hyperfine levels of  $^{15}\text{ND}_3$  in the  $|J, K\rangle = |1, 1\rangle$  state are assigned and their absolute energies are determined to an accuracy of better than 100 Hz. The experimental approach shown in this chapter is generally applicable to high-resolution spectroscopy of polar molecules, and the obtainable spectral resolution can still be readily improved if longer interaction zones and/or slower molecular beams, in particular molecular fountains, would be employed.

# Chapter 4

## A versatile electrostatic trap

### 4.1 Introduction

As was discussed in chapter 1, trapped cold molecules offer unique benefits for many fields of research. Electrostatic traps in particular are highly versatile. They are rather deep (on the order of 1 K) and by changing electrode geometries, many different trapping potentials can be formed (see section 1.2). In this chapter, an electrode geometry is demonstrated that is used to form different trapping fields by changing the voltage applied to the electrodes. In the trap a predominantly dipolar, quadrupolar, or hexapolar field can be created. When implementing the latter two, a pure quadrupole or a pure hexapole trapping potential is generated. Combining a dipole field with a hexapole field gives rise to two additional trapping potentials, a double-well or a ring-shaped potential, depending on the sign of the dipole term. As voltages can be switched on relatively short time scales, rapid changing between these trapping fields is feasible as well.

A double-well trap in particular has proven to be fruitful in atomic physics experiments. For instance, double-well potentials have been used in interference experiments to study coherence properties of BECs [153] and to visualize phase singularities associated with vortices in a Na BEC [154]. Furthermore, two weakly coupled BECs in a double-well potential have been shown to form a Josephson junction [155], and collision studies have been performed in a double-well interferometer, enabling the determination of the *s*- and *d*-wave scattering

---

Adapted from:

*Versatile electrostatic trap*

Jacqueline van Veldhoven, Hendrick L. Bethlem, Melanie Schnell, and Gerard Meijer, *Phys. Rev. A* **73**, 063408 (2006)



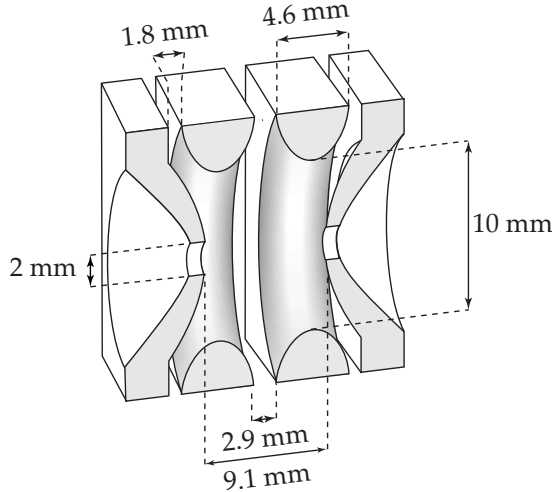


Figure 4.1: Scheme of the trap. The trap is cylindrically symmetric and consists of two parallel rings in the middle and two end caps at the sides.

amplitudes of  $^{87}\text{Rb}$  [156].

In electrostatic traps the formation of a double-well potential with variable barrier height and well separation is relatively straightforward. Along with the possibility of rapid switching to other types of trapping fields, this creates favorable conditions for the study of cold collisions. Molecules trapped in either of the two wells of a double-well trap will gain potential energy when switching to a single-well trap, resulting in two packets of molecules that are accelerated towards each other. As they reach the center of the trap, they will collide with a velocity that is dependent on the shape of both the single- and double-well potential. As these shapes can be readily varied, the velocity of the molecules is tunable. Combining this feature with an inherently low velocity spread of the trapped molecules makes rapid single- to double-well conversion an excellent starting point for studying collisions at low temperatures.

## 4.2 The various trapping configurations

In a cylindrically symmetric geometry, the electric potential  $\Phi(\rho, z)$  can be expressed as [47, 64, 65]:

$$\Phi(\rho, z) = \Phi_0 + \Phi_1 \frac{z}{z_0} + \Phi_2 \frac{(z^2 - \rho^2/2)}{z_0^2} + \Phi_3 \frac{(z^3 - 3\rho^2 z/2)}{z_0^3} \dots, \quad (4.1)$$

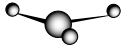
with  $z_0$  a characteristic length scale. Here, the first term is a constant voltage, the second term a constant electric field, the third a quadrupolar electric field, and the fourth a hexapolar electric field. A molecule with a quadratic Stark shift will experience a harmonic force in a quadrupolar electric field, whereas a hexapolar field is needed to form a harmonic trap for a molecule with a linear Stark shift. In our experiments we use  $^{15}\text{ND}_3$  molecules in the low-field-seeking hyperfine levels of the  $|J, K\rangle = |1, 1\rangle$  inversion doublet of the vibrational and electronic ground state. These molecules experience a quadratic Stark shift for small electric field strengths and a linear Stark shift for larger electric field strengths. The dependence of the Stark shift on the electric field strength  $E$  for  $^{15}\text{ND}_3$  in these levels is given by [23]:

$$W_{\text{Stark}}(E) = \sqrt{\left(\frac{W_{\text{inv}}}{2}\right)^2 + \left(\frac{1}{2}\mu E\right)^2} - \left(\frac{W_{\text{inv}}}{2}\right), \quad (4.2)$$

with  $W_{\text{inv}}$  the inversion splitting and  $\mu$  the dipole moment. For  $^{15}\text{ND}_3$  the inversion splitting is 1430.3 MHz (see chapter 3) and the dipole moment is taken to be the same as for  $^{14}\text{ND}_3$ , i.e., 1.48 D [152]. At even larger field strengths, the effect of mixing with higher rotational levels becomes more important and higher order terms have to be taken into account.

Using the four-electrode geometry shown in figure 4.1, it is possible to create a field with dominant dipolar, quadrupolar, or hexapolar contributions, by applying the appropriate voltages. The trap has a hexapole geometry consisting of two ring electrodes with an inner diameter of 10 mm and two end caps. The two rings have a width of 4.6 mm and are separated by 2.9 mm, whereas the two end caps are separated by  $2z_0 = 9.1$  mm. They each have a hole with a diameter of 2.0 mm, the first to allow molecules to enter and the second to extract the ions that are produced in the detection scheme.

In figure 4.2, the voltages needed for two different trapping fields are shown. When a voltage  $-U_2$  is applied to the two ring electrodes and a voltage  $U_2$  is applied to both end caps, such as shown on the left-hand side of the figure, a field is formed with a dominant quadrupole term. Using a commercially available finite difference program [157], the potential of this configuration is simulated. Below the trap cross section the electric field strength as a function of position is shown for both the  $\rho$  direction (solid line) and the  $z$  direction (dotted line). Fitting the corresponding potential to equation 4.1, we find that  $\Phi_0 \approx -0.43 U_2$ ,  $\Phi_2 \approx 1.05 U_2$ ,  $\Phi_4 \approx 0.35 U_2$ , and  $\Phi_6 \approx -0.04 U_2$  and that the uneven terms are zero due to symmetry. Beneath the electric field strength in figure 4.2 the Stark energy in mK ( $T = W_{\text{Stark}}/k$ , with  $k$  the Boltzmann constant) of a  $^{15}\text{ND}_3$  molecule in this field is shown. The electric field in the quadrupole trap increases linearly with distance, but, because of the nonlinear dependence of the Stark energy on the electric field, the potential is harmonic near the center of the trap. Further away from the center the potential is linear. The resulting trap is tight (the trapping frequency is  $\omega_z/2\pi = 1.7$  kHz at the center of the trap) and has a depth of 0.09 K for  $^{15}\text{ND}_3$ .



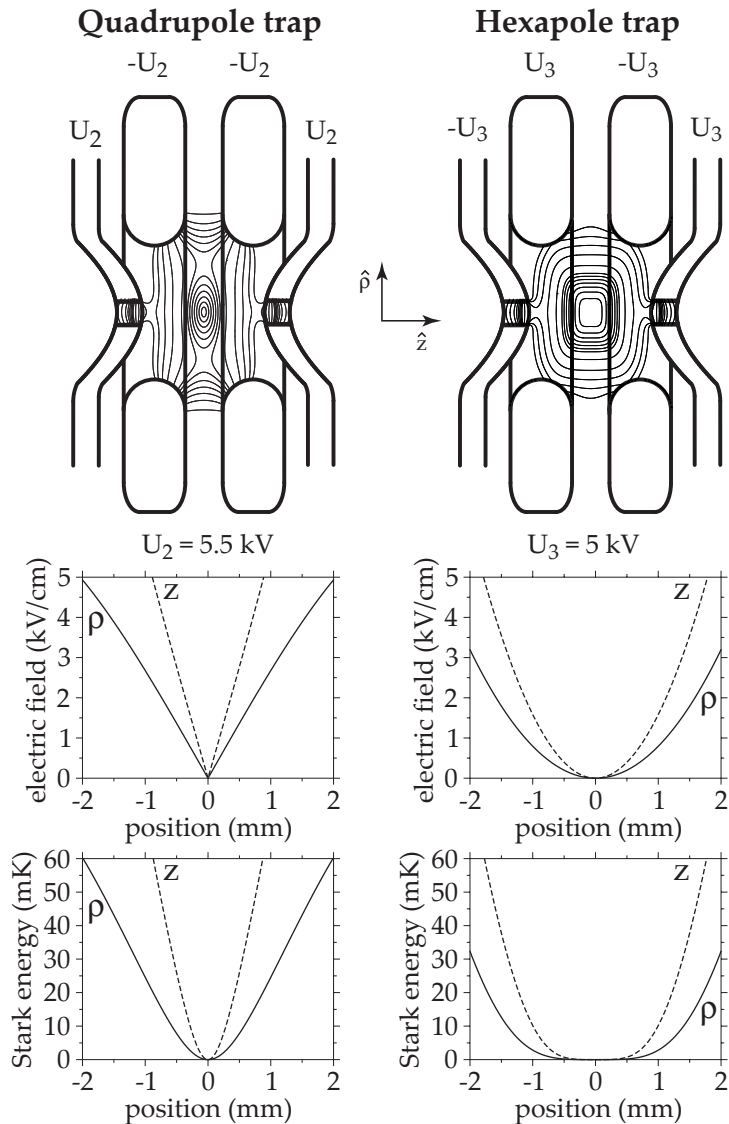


Figure 4.2: Two cross sections of the trap. On the left-hand side, the voltages that result in a quadrupole trap are shown, along with lines of constant electric field for electric field strengths of every  $\text{kV}/\text{cm}$  from 1 to  $7 \text{ kV}/\text{cm}$  and every  $5 \text{ kV}/\text{cm}$  from 10 to  $25 \text{ kV}/\text{cm}$ . On the right-hand side, the same is shown for a hexapole trap. Below the two cross sections, the electric field is shown along with the Stark energy of a  $^{15}\text{ND}_3$  molecule as a function of position in the  $\rho$  and  $z$  direction (solid line and dotted line, respectively).

A hexapole trap results when the voltages  $U_3$  and  $-U_3$  are applied alternately to the four electrodes of the trap as shown on the right-hand side of figure 4.2. A fit of the potential of this field to equation 4.1 yields  $\Phi_1 = 0$ ,  $\Phi_3 \approx U_3$  and  $\Phi_5 \approx -0.04 U_3$ , with the even terms being zero due to symmetry. Again, both the electric field strength along the  $\rho$  and  $z$  directions (solid and dotted line, respectively) and the Stark energy of a  $^{15}\text{ND}_3$  molecule in this field are shown below the cross sections of the trap. The electric field strength in this trap is quadratically dependent on the distance from the center. However, due to the nonlinear Stark effect the potential is essentially flat near the center of the trap. Away from the center the potential becomes harmonic. This trap is less tight (the trapping frequency is  $\omega_z/2\pi = 0$  at the center of the trap and goes to  $\omega_z/2\pi = 750$  Hz further away from the center) and has a depth of 0.35 K for  $^{15}\text{ND}_3$ .

When applying voltages of  $-U_1$ ,  $-0.6 U_1$ ,  $0.6 U_1$ , and  $U_1$  consecutively to the four electrodes of the trap, a dipolar field is formed. Fitting the potential of this field to equation 4.1 results in  $\Phi_1 \approx 0.88 U_1$ ,  $\Phi_3 = 0$ , and  $\Phi_5 \approx 0.09 U_1$ , with the even terms being zero due to symmetry. Adding a dipole field to a hexapole field results in either a double-well potential or a donut potential, depending on the relative sign of the dipole and hexapole term. In figure 4.3 both configurations are shown, along with the electric field strength and the Stark energy of a  $^{15}\text{ND}_3$  molecule in this field along the  $\rho$  and  $z$  directions (solid and dotted line, respectively). Both the distance between the two minima in the double-well trap and the diameter of the ring-shaped minimum in the donut trap are dependent on the ratio between the dipole and hexapole term. In the upper graph of figure 4.4, the distance between the two wells is shown as a function of the ratio  $|U_1/U_3|$  in the case of an ideal hexapole and dipole field (solid line). The dotted line shows the same for the diameter of the donut-shaped minimum. The crosses and triangles (double-well trap and donut trap, respectively) indicate the simulated value of this well separation, using the finite difference program with  $U_3 = 5$  kV and different values of  $U_1$ .

The height of the barrier between the two wells is shown in the lower graph of figure 4.4, given in mK for  $^{15}\text{ND}_3$ . In the case of an ideal hexapole and dipole field (solid line), this height is the same for the double-well and donut trap and is solely dependent on the value of  $|U_1|$ . Note that the barrier height is identical to the amount of potential energy gained by a  $^{15}\text{ND}_3$  molecule in the center of one of the wells when switching to the single-well configuration. This can be seen by realizing that in the center of the double-well trap, i.e., at the top of the barrier, the electric field strength is determined by the dipole term only, as the hexapole field is zero there. In the center of one of the wells the hexapole field is equal to the dipole field, although opposite in direction. Therefore, when switching the dipole field off to produce a single-well trap, molecules originally at the center of one of the two wells will now have a potential energy equal to the barrier height. Values for the barrier height were obtained using the finite difference program as well and are shown as crosses (double-well trap) and



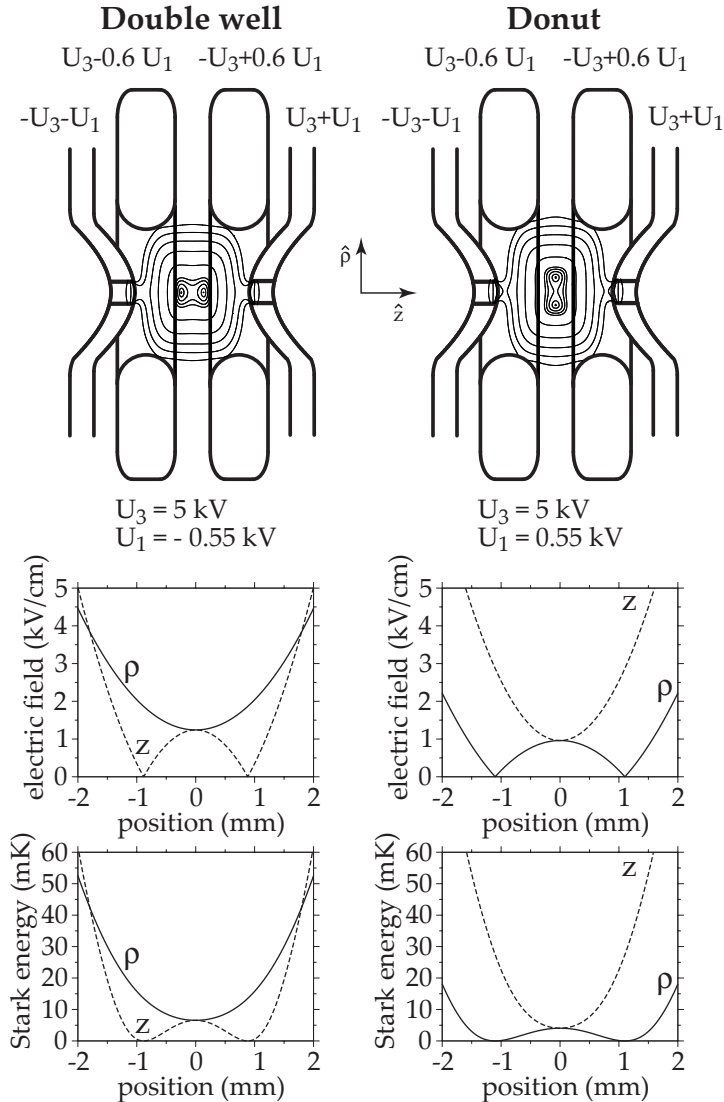


Figure 4.3: Two cross sections of the trap. On either side the voltages that are applied when a dipole field is added to a hexapole field are shown. Lines of constant electric field are shown for electric field strengths of 0.1 kV/cm, every 0.5 kV/cm from 0.5 to 2 kV/cm, and every 5 kV/cm from 5 to 25 kV/cm. On the left-hand side (right-hand side)  $U_1$  and  $U_3$  have the same (opposite) sign. In each case both the electric field and the Stark energy of a  $^{15}\text{ND}_3$  molecule as a function of position are shown in both the  $\rho$  and  $z$  direction (solid line and dotted line, respectively).

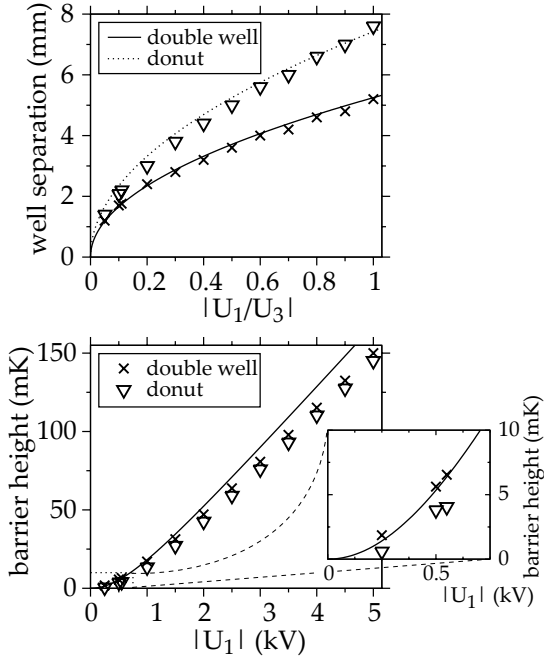
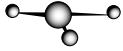


Figure 4.4: Well separation as a function of  $|U_1/U_3|$  and barrier height (for  $^{15}\text{ND}_3$ ) as a function of  $|U_1|$  in the ideal double-well (solid line) and donut trap (dotted line). In both graphs the crosses (double-well trap) and triangles (donut trap) show the same quantities obtained from electric field simulations of the actual trap geometry.

triangles (donut trap) in the lower graph of figure 4.4. From these two graphs it is clear that both the well separation and the barrier height, and therefore also the collision energy of the molecules upon double- to single-well conversion, can easily be changed by varying the voltages on the four electrodes. At the maximum value of  $|U_1|$  used in the experiment,  $|U_1| = 0.55 \text{ kV}$ , the barrier height is on the order of 5 mK. The separation between the wells is 1.8 mm in this case ( $U_3 = 5 \text{ kV}$ ), whereas the diameter of the donut-shaped minimum is 2.2 mm.

### 4.3 Experiment

In figure 4.5 the experimental setup is shown. In the experiments, the trap is loaded from a Stark-decelerated molecular beam. A mixture of 5%  $^{15}\text{ND}_3$  seeded in xenon is supersonically expanded from a pulsed valve at a 10 Hz rate.



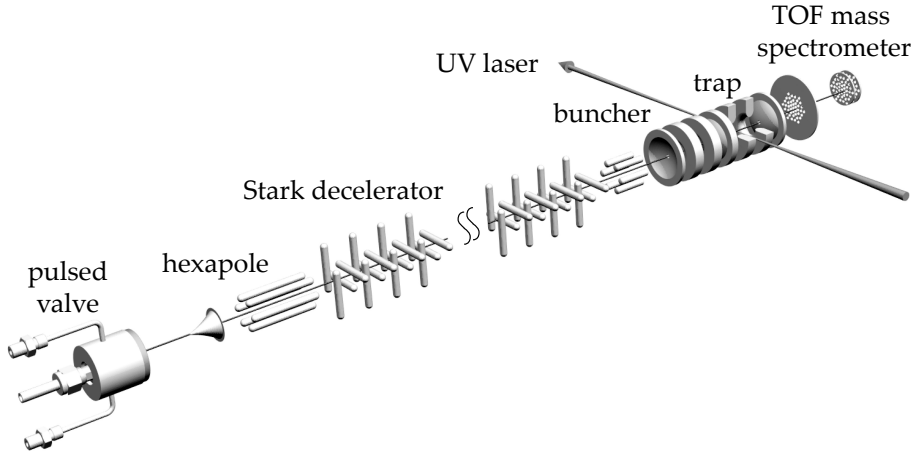


Figure 4.5: Experimental setup. A pulsed supersonic beam of  $^{15}\text{ND}_3$  molecules seeded in xenon exits a cooled valve with a velocity of 280 m/s. Ammonia molecules in the low-field-seeking hyperfine levels of the  $|J, K\rangle = |1, 1\rangle$  state are focused into the decelerator by a hexapole, decelerated, and then transversally and longitudinally focused into the trap by a hexapole and buncher, respectively. The molecules are detected in a TOF-mass spectrometer.

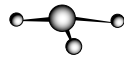
Due to cooling of the valve to  $-70^\circ\text{C}$ , the gas pulse has a velocity of 280 m/s. In the expansion, about 60% of the ammonia molecules are internally cooled to the ground state of para-ammonia, the  $|J, K\rangle = |1, 1\rangle$  inversion doublet in the electronic and vibrational ground state. After passing through a skimmer, those molecules that reside in the low-field-seeking hyperfine levels of the upper component of the inversion doublet are focused into the Stark decelerator by a 6 cm long hexapole. Molecules in high-field seeking levels are attracted by the high electric fields of both the hexapoles and the decelerator and will be lost from the beam. Molecules that reside in the remainder of the hyperfine levels of the inversion doublet, that only have a higher order Stark effect, will hardly be affected by the electric fields. The decelerator consists of 95 pairs of parallel 3 mm-diameter rods, with a closest distance of 2 mm between two rods and a closest distance of 2.5 mm between pairs of rods. Each consecutive pair of rods is rotated over  $90^\circ$  and within each pair, a positive voltage of 10 kV is applied to one electrode, whereas the same negative voltage is applied to the other. A more extensive description of this part of the setup, along with the operation principle of the decelerator can be found in chapter 3 and [148]. Using a phase angle of  $57.5^\circ$ , a subset of low-field-seeking molecules with an initial velocity of around 280 m/s is decelerated to about 15 m/s at the exit of the decelerator. After 5 mm the molecules are transversally focused into the trap

by a second (12.5 mm long) hexapole. Subsequently, they are longitudinally focused into the trap using a buncher that is placed another 5 mm downstream of the hexapole. The buncher has a geometry similar to that of the trap. Before the ammonia molecules enter the trap, voltages are applied to the trap such that a last electric field slope is formed. In gaining Stark energy when entering the trap, the low-field-seeking molecules lose their last kinetic energy and reach a stand-still in the middle of the trap. At this moment the voltages on the four electrodes are switched to generate a particular trapping potential, thereby confining the molecules in either a quadrupole, hexapole, double-well, or donut potential. After a certain trapping time, the trap is turned off and molecules in the upper component of the inversion doublet are ionized in a state-selective (2+1)-Resonance Enhanced Multi Photon Ionization (REMPI) scheme, using a pulsed UV laser around 317 nm [137] (see also figure 2.5 on page 27). The resulting ions are subsequently detected in a time-of-flight (TOF) mass spectrometer. Using a 75 cm lens, the ionization laser is focused into the trap passing through the 2.9 mm gap between the two ring electrodes. The laser focus is estimated to be about 200  $\mu\text{m}$  in diameter. Applying small bias voltages of 200, 150, -150, and -200 V to the four electrodes of the trap results in an electric field that accelerates the ions towards the detector. The ions are detected over a length of 2 mm along the laser beam, limited by the size of the hole in the end cap. Using a computer controlled translation stage, the focus of the laser beam can be moved along the beam axis, i.e., along the z direction, over about 2.5 mm. In this way, the spatial distribution of the trapped molecules can be measured.

## 4.4 Results and discussion

In figure 4.6, the density of trapped  $^{15}\text{ND}_3$  molecules is shown as a function of position in the z direction, both for hexapole and for quadrupole trapping voltages. The measurements are taken after the molecules have been trapped for about 72 ms. We found that in order to obtain a single-well profile for the molecules confined in the hexapole trap, a small dipole term had to be added. We attribute this to deviations of the distances between the electrodes from the ideal geometry. This compensating dipole term is added in all subsequent measurements. As the quadrupole trap is much tighter than the hexapole trap (see figure 4.2), a signal difference arises between the two traces. The peak density of molecules in the hexapole trap is about  $10^7 \text{cm}^{-3}$ , whereas it is about ten times higher in the quadrupole trap. The loading process is identical for both traps and is matched to the hexapole trap, resulting in a less than perfect match of the decelerated packet to the quadrupole trap. This gives rise to the peculiar shape of the measured distribution in the quadrupole trap, which seems to consist of two packets with different temperatures.

In figure 4.7 the density of  $^{15}\text{ND}_3$  molecules in the hexapole trap is shown



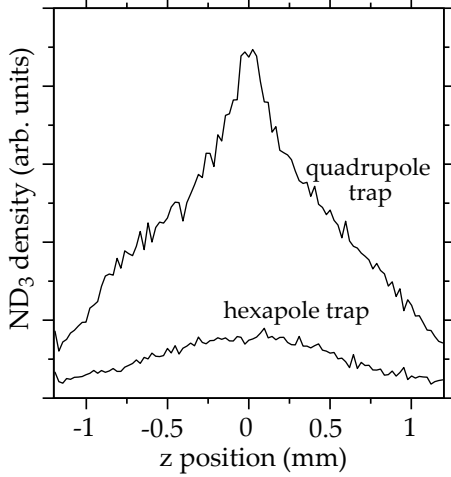


Figure 4.6: Density of trapped  $^{15}\text{ND}_3$  molecules as a function of position in the  $z$  direction for both the quadrupole trap (upper trace) and the hexapole trap (lower trace), after trapping for about 72 ms.

as a function of position in the  $z$  direction. By adding a dipole term to the hexapole term, the shape of the trap and thereby the profile of the trapped molecules can be changed significantly. Each trace in figure 4.7 corresponds to a different value of the added dipole term. When no dipole is added, the trap consists of only a single well. A single peak results, as trace (d) shows. Adding a negative dipole term transforms the single well to a double well, with a distance and barrier between the two wells that depend on the value of the dipole term. The upper three traces of figure 4.7 show two peaks that move closer together as the dipole term is increased from -0.55 kV (trace (a)) to -0.3 kV (trace (b)) to -0.15 kV (trace (c)). When a positive dipole term is added, the shape of the trap becomes that of a donut. As only molecules in the relatively small laser focus near the center of the trap are ionized in the detection scheme, this transformation to a donut-shaped trap leads to a reduction in signal only, as is shown by trace (e) and (f) ( $U_1 = 0.25$  kV and  $U_1 = 0.55$  kV, respectively).

At the densities that we have in the trap, no thermalizing collisions occur, and formally no temperature can be assigned. The distribution of the trapped sample is determined by the details of the loading process. To characterize this distribution in terms of a temperature, we fitted the density profile to the thermal density distribution [158]:

$$n(\rho, z) = n_0 e^{-W_{\text{Stark}}(\rho, z)/kT}, \quad (4.3)$$

with  $n_0$  the density at the trap minimum and  $W_{\text{Stark}}(\rho, z)$  the potential energy as a function of position. On the right-hand side of figure 4.7, the measurements

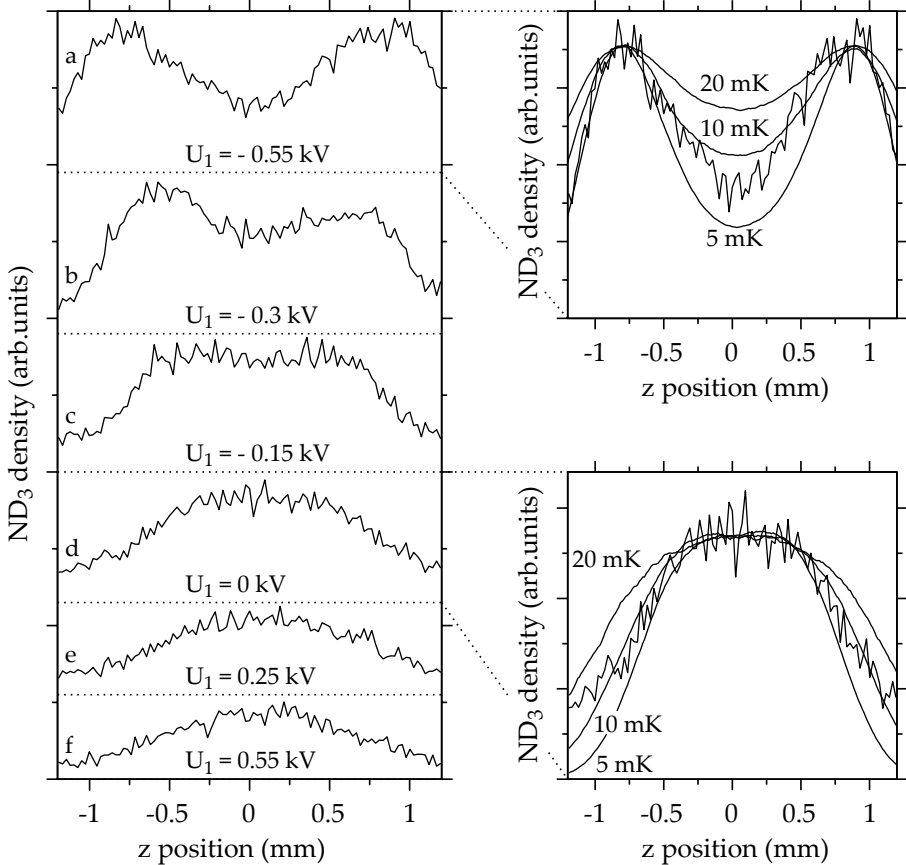
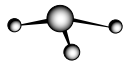


Figure 4.7: Density of  $^{15}\text{ND}_3$  molecules confined in a hexapole trap as a function of position in the  $z$  direction. A negative dipole term of  $-0.55$ ,  $-0.3$ , and  $-0.15$  kV is added to the hexapole term ( $U_3 = 5$  kV) in the upper three traces (a-c), resulting in a double-well potential. Trace (d) shows a packet in a purely single well. A positive dipole term of  $0.25$  and  $0.55$  kV is added for the lower two traces (e-f), thereby creating a donut potential. On the right-hand side, traces (a) and (d) are shown once more, along with simulations of the density distribution of the packet of molecules for temperatures of  $5$ ,  $10$ , and  $20$  mK.



with a dipole term of  $U_1 = -0.55$  kV and  $U_1 = 0$  kV are shown once more, along with the thermal density distribution as obtained from equation 4.3 for temperatures of 5, 10, and 20 mK. It can be seen that in either case the simulated distribution with a temperature of 10 mK matches the measurement best. This temperature is slightly higher than the barrier height at  $U_1 = -0.55$  kV ( $\sim 5$  mK). The same simulation has been performed for the spatial distribution of molecules confined in a quadrupole trap. Due to the seemingly double profile, it is more difficult to describe this distribution with a single temperature. A temperature of 75 mK seems to best describe the broad base, whereas the sharp center peak agrees best with a temperature of 5 mK. An alternative method to deduce a temperature is to measure the width of the packet of trapped molecules as a function of time after the trap has been turned off. Measurements of this type are shown in figure 4.8. On the left-hand side two profiles of  $^{15}\text{ND}_3$  molecules are seen, one after 20  $\mu\text{s}$  and one after 420  $\mu\text{s}$  after switching off the hexapole trap (upper and lower curve, respectively). In either case the molecules have been confined for about 72 ms. Due to the velocity spread of the molecules the packet spreads out after the trap has been turned off, resulting in less signal and an increased width. To obtain this width a Gaussian line shape is fitted to each profile. The acquired full width at half maximum (FWHM) is shown as a function of free-flight time on the right-hand side of the figure (solid line with crosses). To deduce a temperature, this curve is fitted to  $\sqrt{(\Delta z)^2 + (\Delta v_z \cdot t)^2}$  (dotted line with triangles), resulting in a velocity spread of 2.3 m/s and a position spread of 1.8 mm (both FWHM). Using  $\Delta v_z = \sqrt{8\ln 2} \cdot \sqrt{kT/m}$  [159], this gives a temperature of about 2.5 mK.

The different temperatures of 10 and 2.5 mK, obtained by the two different methods, are indicative of the limitations of either method. The first method relies on an accurate knowledge of the potential energy that the molecules have in the trap. Possible misalignments of the electrodes of the trap cause uncertainties in the actual electric field, and therefore in  $W_{\text{Stark}}(\rho, z)$ . These misalignments are most likely to result in a confining field that is less tight, leading to an overestimation of the temperature. In addition, both methods depend on the determination of the width of the spatial distribution of the packet. In our analysis, we assume the detection volume to be much smaller than the spatial spread of the trapped molecules. For a diffraction-limited laser focus this is certainly the case (in our experiment the waist of the laser beam would be less than 100  $\mu\text{m}$ ). However, the laser focus of our multimode laser is most certainly larger. Furthermore, due to a less than ideal pointing stability of the laser beam and a nonplanar entrance window of the vacuum system our effective detection volume is increased. In the first method, this leads to an overestimation of the temperature and in the second to an underestimation. It is therefore believed that the actual temperature lies in between the temperatures found using the two methods.

In figure 4.9 the density of ammonia molecules is shown in both the quadrupole and the hexapole trap as a function of time that the trap is on. The

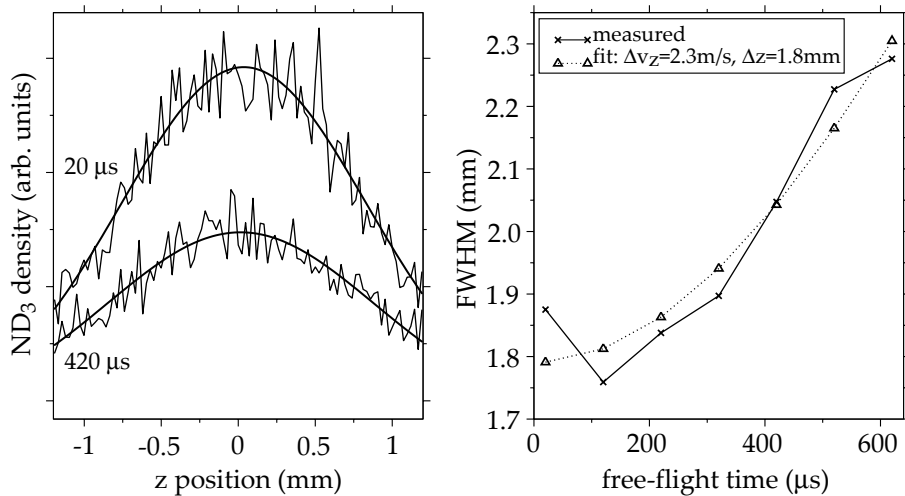


Figure 4.8: Determination of the temperature of a packet of  $^{15}\text{ND}_3$  molecules trapped in the hexapole trap. On the left, the profile of a packet is shown 20 and  $420\ \mu\text{s}$  after the trap is turned off (upper and lower trace, respectively). From a fit to a Gaussian lineshape the FWHM of the distribution is obtained, as shown as a function of free-flight time (solid line with crosses) on the right-hand side of the figure.

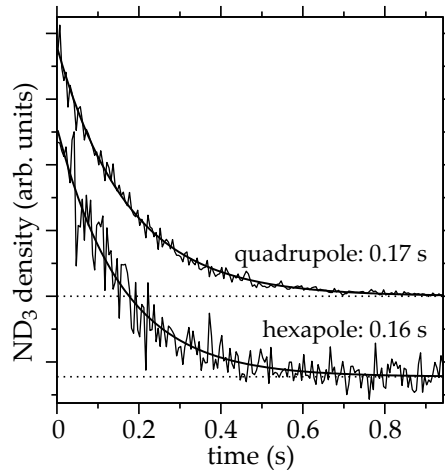
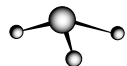


Figure 4.9: Density of  $^{15}\text{ND}_3$  molecules in the quadrupole (upper trace) and the hexapole (lower trace) trap as a function of time that the trap is on.



molecules are seen to leave the trap with a  $1/e$  time of 0.16 s for the hexapole trap and 0.17 s for the quadrupole trap, the same within error bars. The trapping lifetime is mainly limited by background collisions (background pressure  $4 \cdot 10^{-8}$  mbar)<sup>1</sup>.

## 4.5 Conclusions

In this chapter, a new electrostatic trapping geometry has been presented that illustrates the versatility of electric fields in forming tailored trapping potentials. By applying different voltages to a set of four electrodes, different trapping fields are created, between which rapid switching on a time scale of 100 ns is possible. Spatial distributions and lifetimes of a cold packet of  $^{15}\text{ND}_3$  molecules loaded into both a hexapole and a quadrupole trap are shown. Additionally, a hexapole trap is studied that transforms into a double-well or donut trap when different dipole terms are added. The barrier height and well separation of either one of these two traps depend on the strength of the dipolar and hexapolar electric field and are easily changed.

Rapid switching between, for instance, the double-well trap and a pure hexapole trap offers good prospects for measuring collision cross sections as a function of collision energy at low temperatures. The amount of energy gained by molecules trapped in one of the wells after switching to the single well depends solely on the strength of the electric dipole field, which can be easily varied.

---

<sup>1</sup>Optical pumping of  $\text{ND}_3$  by blackbody radiation is calculated to have a  $1/e$  time of 7 s at room temperature, and can therefore be neglected [160]. For  $\text{NH}_3$  this value is 4 s.

# Chapter 5

## An AC electric trap for ground-state molecules

### 5.1 Introduction

In the previous chapter, a trap was demonstrated that is capable of trapping cold molecules in low-field-seeking states. As was also discussed in section 1.2.2, however, for many applications of cold molecules [146, 161], trapping of molecules in high-field-seeking states is required. For one, the ground state of a system is always lowered by an external perturbation. Therefore, the ground state of any molecule is high-field seeking. In the ground state, trap loss due to inelastic collisions is absent, making it possible to cool these molecules further using evaporative or sympathetic cooling. This is particularly relevant as the dipole-dipole interaction for polar molecules in excited rovibrational states is predicted to lead to large cross sections for inelastic collisions [31]. Furthermore, molecules composed of heavy or of many atoms have small rotational constants. Consequently, all states of these molecules become high-field seeking in relatively small magnetic or electric fields (see also figure 1.3 on page 11).

Although Maxwell's equations allow for a minimum, they do not allow for a maximum of a static magnetic or electric field in free space (see the appendix), which is required for trapping of molecules in high-field-seeking states. It is possible, however, to create an electric field maximum using optical fields [95, 97] (see also section 1.2.3). Unfortunately, the trap depth and volume of optical

---

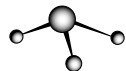
Adapted from:

*ac electric trap for ground-state molecules*

Jacqueline van Veldhoven, Hendrick L. Bethlem, and Gerard Meijer, *Phys. Rev. Lett.* **94**, 083001 (2005)

*Trapping polar molecules in an AC trap*

Hendrick L. Bethlem, Jacqueline van Veldhoven, Melanie Schnell, and Gerard Meijer (*submitted*)



traps are rather limited. In this chapter, we experimentally demonstrate an AC electric trap, a new trap for molecules in high-field-seeking states with a depth and a volume that is considerably larger than obtainable with an optical trap.

## 5.2 Trapping principles

As was also discussed in the introduction (section 1.2), for a force field  $\vec{F}(\vec{r})$  to keep a particle in static equilibrium around  $\vec{r} = 0$ , two conditions must be met. The applied force must vanish at  $\vec{r} = 0$ , and for small displacements the force field should tend to restore the particle towards  $\vec{r} = 0$ . To achieve the latter it is necessary that the divergence of the force be negative,  $\nabla \cdot \vec{F} < 0$  in a volume around  $\vec{r} = 0$ .

The force acting on a polar molecule in an inhomogeneous electric field  $\vec{E}(\vec{r})$  is given by

$$\vec{F}(\vec{r}) = -\nabla W(E), \quad (5.1)$$

with  $W(E)$  the Stark energy of a polar molecule in an electric field of magnitude  $E = |\vec{E}|$ . In most common cases the Stark shift of a molecule is either a linear or a quadratic function of the applied field. For molecules that experience a linear Stark shift in the applied field,  $W = -\mu_{\text{eff}} E$ , it can be shown that [103]

$$\begin{aligned} \nabla \cdot \vec{F} = \frac{\mu_{\text{eff}}}{E^3} \sum_{i,j,k=1}^3 & \left[ \left( \frac{\partial \Phi}{\partial x_k} \right)^2 \left( \frac{\partial^2 \Phi}{\partial x_i \partial x_j} \right)^2 - \right. \\ & \left. \left( \frac{\partial \Phi}{\partial x_i} \right) \left( \frac{\partial \Phi}{\partial x_k} \right) \left( \frac{\partial^2 \Phi}{\partial x_i \partial x_j} \right) \left( \frac{\partial^2 \Phi}{\partial x_k \partial x_j} \right) \right], \end{aligned} \quad (5.2)$$

where  $\Phi$  is the electrostatic potential and  $\mu_{\text{eff}}$  is an effective dipole moment which depends on the particular molecular state. Using Schwarz's inequality, it can be seen that the sum is always larger than, or equal to zero. Therefore, for molecules having a linear Stark shift, the sign of  $\nabla \cdot \vec{F}$  is determined solely by the sign of  $\mu_{\text{eff}}$ .

Similarly, for molecules that experience a quadratic Stark shift in the applied field,  $W = -1/2\alpha_{\text{eff}} E^2$ , it can be shown that [103]

$$\nabla \cdot \vec{F} = \alpha_{\text{eff}} \sum_{i,j=1}^3 \left( \frac{\partial^2 \Phi}{\partial x_i \partial x_j} \right)^2, \quad (5.3)$$

where  $\alpha_{\text{eff}}$  is the effective polarisability which depends on the particular molecular state. Again, it is seen that the sign of  $\nabla \cdot \vec{F}$  is only determined by the sign of  $\alpha_{\text{eff}}$ .

For molecules in low-field-seeking states, i.e., for molecules that have a negative  $\mu_{\text{eff}}$  or  $\alpha_{\text{eff}}$ , we conclude from equation 5.2 and equation 5.3 that

$\nabla \cdot \vec{F} \leq 0$ , and trapping is straightforward. This is equivalent to saying that it is possible to create an electric field minimum. For molecules in high-field-seeking states, i.e., for molecules that have a positive  $\mu_{\text{eff}}$  or  $\alpha_{\text{eff}}$ , we conclude from equation 5.2 and equation 5.3 that  $\nabla \cdot \vec{F} \geq 0$  and trapping is more problematic. This is equivalent to saying that it is *not* possible to create an electric field maximum (see also the appendix). Nevertheless it is possible to trap these molecules using the various methods that are described in the introduction (section 1.2.3). The AC traps that will be discussed in this chapter make use of the fact that it is possible to create a field for which  $\nabla \cdot \vec{F}$  is equal to zero at a certain position, irrespective of (the sign of) the Stark shift. As a consequence, at this position the focusing force along one direction is equal to the defocusing forces along the other directions, i.e, the electric field strength has a saddle point here. In some cases it is possible to reverse the focusing and defocusing directions by changing the voltages applied to the electrodes. If we switch the voltages between these two configurations, molecules will be alternately focused and defocused. As molecules tend to be further away from the saddle point along the focusing direction and closer to the saddle point along the defocusing direction, this leads to a net focusing. This principle is used in ion-traps [162] and alternate gradient synchrotrons [102].

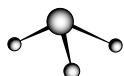
### 5.3 Electrode geometry

In figure 5.1 three electrode geometries are depicted that are suitable for AC trapping of polar molecules. These geometries have in common that the symmetry of the electrostatic potential is such that  $\nabla \cdot \vec{F} = 0$  at the center, and that the direction of  $\vec{F}$  can be reversed by changing the voltages applied to the electrodes<sup>1</sup>.

(a) *linear AC trap*; Consider the geometry shown in figure 5.1(a). The four identical electrodes are positioned on the corners of a square. A positive voltage is applied to the upper electrode, while an equal negative voltage is applied to the lower electrode. The other two electrodes are at ground potential<sup>2</sup>. Molecules in high-field-seeking states are focused towards the center along the x axis while they are defocused along the y axis. We will first assume the electrodes to be of infinite length, in which case  $\partial\Phi/\partial z = 0$  and  $\partial^2\Phi/\partial z^2 = 0$ . The electrostatic potential is symmetric under reflection in the y-z plane and therefore  $\partial\Phi/\partial x = 0$  everywhere on this plane. The electrostatic potential is

<sup>1</sup> As also discussed in the introduction (section 1.2.3), the three geometries presented in this section for trapping neutral atoms and molecules using time-varying electric fields all have their magnetic counterpart. A cylindrically symmetric magnetic AC trap was proposed for spin-polarized atomic hydrogen atoms by Lovelace et al. [109], and later demonstrated for cesium atoms by Cornell et al. [110]. Due to the technical difficulties associated with generating time-varying magnetic fields, the depth of these traps are limited to below 100  $\mu\text{K}$ .

<sup>2</sup> Alternatively, one may apply a positive voltage to two neighbouring electrodes while the other two electrodes are kept at a negative voltage [108].



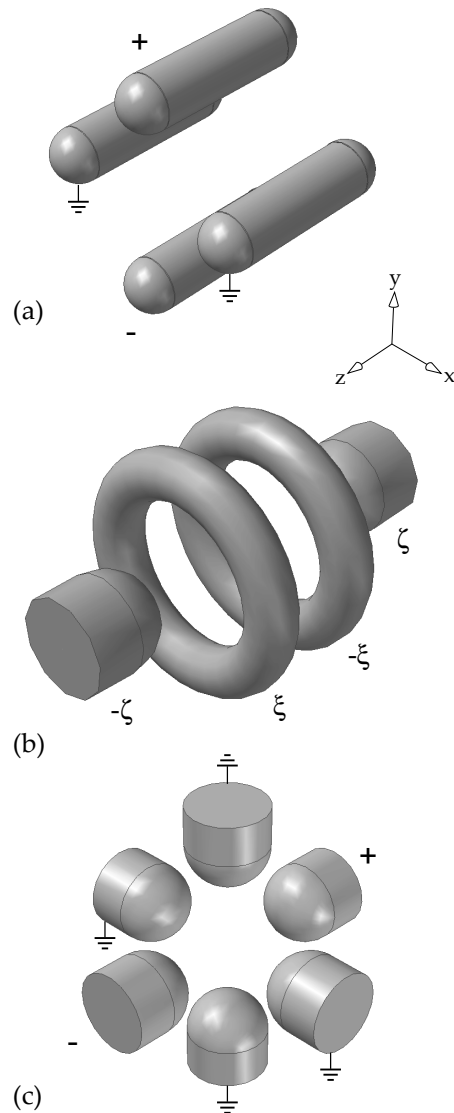


Figure 5.1: Three possible electrode geometries that can be used for AC trapping of polar molecules. (a) Linear AC trap. (b) Cylindrical AC trap. (c) Three-phase AC trap.

antisymmetric under reflection in the x-z plane, and therefore  $\partial^2\Phi/\partial y^2 = 0$  everywhere on this plane. At the intersection of the two planes, the z axis, both  $\partial^2\Phi/\partial y^2 = 0$  and  $\partial^2\Phi/\partial z^2 = 0$ . As the electrostatic potential obeys Laplace's equation,  $\nabla^2\Phi = 0$ , it follows that  $\partial^2\Phi/\partial x^2 = 0$  at the z axis. Using these relations we find from equation 5.2 and equation 5.3 that for molecules experiencing a linear or quadratic Stark shift  $\nabla \cdot \vec{F} = 0$  at the z axis. The force constants in the two transverse directions,  $k_x = -\partial F/\partial x$  and  $k_y = -\partial F/\partial y$ , are therefore equal and opposite,  $k_x = -k_y$ . The focus and defocus direction can be reversed by switching the voltage off on the upper and lower electrodes while applying a voltage difference to the two electrodes that were initially at ground potential. By alternating between these two configurations at the appropriate frequency, this geometry acts as 2D guide for polar molecules in both high-field and low-field-seeking states. This guide was first proposed by Auerbach, Bromberg and Wharton [103] and recently demonstrated by Junglen et al. [63]. By bending this guide into a torus it can be used as a storage ring [103, 163]. Let us now consider what happens if the electrodes are of finite size. Along the z axis the electric field will have a maximum at the center of the trap, therefore, molecules in high-field-seeking states will experience a (static) trapping potential along this direction. It is easily seen that at the center of the trap  $\nabla \cdot \vec{F} = 0$ . However, since  $k_z \neq 0$  the defocusing force will be larger than the focusing force. When  $k_z$  is not too big, this does not dramatically decrease the stability and molecules can be trapped in three dimensions. This trap is the neutral analog of the linear Paul trap for ions and was recently demonstrated for neutral molecules by Schnell et al. [117]. A microstructured version of this trap for neutral atoms was proposed and demonstrated by Katori et al. [115, 116].

(b) *Cylindrical AC trap*; Consider the geometry shown in figure 5.1(b). The structure consists of two ring electrodes and two cylindrically symmetric end caps. A negative voltage,  $-\zeta$ , is applied to the left end cap while an equal positive voltage,  $\zeta$  is applied to the right end cap. The left ring electrode is kept at a positive voltage,  $\xi$  while the right ring electrode is kept at an equal negative voltage  $-\xi$ . The electrostatic potential is antisymmetric about the x-y plane and therefore,  $\partial^2\Phi/\partial z^2 = 0$  everywhere on this plane. The electrostatic potential is symmetric about any plane containing the z axis, and therefore  $\partial\Phi/\partial x = 0$  and  $\partial\Phi/\partial y = 0$ . Due to symmetry,  $\partial^2\Phi/\partial x^2 = \partial^2\Phi/\partial y^2$  at the z axis, and from Laplace's equation both terms are zero at the point of intersection between the symmetry axis and the plane of antisymmetry, at the center of the trap. Again, in case of a linear or quadratic Stark shift,  $\nabla \cdot \vec{F} = 0$  at the center of the trap<sup>1</sup>. The force constant along the z axis is twice the force

<sup>1</sup>When  $\zeta$  and  $\xi$  are chosen such that  $E=0$  at the center of the trap, a hexapolar field results. An attempt to calculate  $\nabla \cdot \vec{F}$  by using equation 5.2 fails due to the  $1/E^3$  term. However, as the Stark effect of any molecule is quadratic in weak fields, we should use equation 5.3 instead. From equation 5.3,  $\nabla \cdot \vec{F}=0$  at the center of the trap. As both  $k_x$ ,  $k_y$  and  $k_z$  are equal to zero the trap volume is infinitely small.



constant along  $\rho$ ,  $k_z = -2k_\rho$ , where  $\rho = \sqrt{x^2 + y^2}$ . The size and direction of the force depend on the ratio of  $\zeta$  to  $\xi$ . This ratio can be chosen such that  $k_z = -2k_\rho = a$  or  $k_z = -2k_\rho = -a$ , with  $a$  a constant (see section 5.4). In this case the electric field at the center of the trap is equal in magnitude and direction for both configurations. This trap is the neutral analog of the Paul trap for ions [162] and was first proposed by Peik [114].

(c) *Three-phase AC trap*; Consider the geometry shown in figure 5.1(c). The structure consists of six hemispherically ended electrodes that point towards the center of the trap. A positive voltage is applied to the right electrode and a negative voltage to the left electrode while the other electrodes are kept at ground potential<sup>1</sup>. Although the cylindrical symmetry is lost, the field has essentially the same form as the cylindrical AC trap discussed before. The main difference lies in the way the voltages are being switched. In the three-phase trap the voltages are alternately applied to the electrodes at the x, y, or the z axis. In this way, molecules will experience a focusing force 2/3 of the time, while they experience a two times larger defocusing force 1/3 of the time. This trap is the neutral analog to three-phase trap for ions [164] and was proposed by Shimizu and Morinaga [111].

## 5.4 Optimal shape

In this section we will determine the optimal shape of the electrodes making up an AC trap. We will concentrate on the cylindrical AC trap which is used in the experiments to be described in section 5.6. The optimal shape of the electrodes of a linear or three-phase AC trap can be determined in a similar fashion (see also [108]).

As we will see later, an AC trap has the largest depth and volume if the molecules experience a harmonic interaction potential. For molecules that experience a linear Stark shift the ideal form for the field strength is therefore also harmonic;  $E(z, \rho) = E_0 + \eta(z^2 - \frac{1}{2}\rho^2)$ , where the sign of  $\eta$  can be reversed by switching the voltages.

We start by expanding the electric field in a Legendre series following [47]. In a region devoid of charges the electric field can be derived from the electric potential  $\Phi$ ;  $\vec{E} = -\nabla\Phi$ , with  $\nabla^2\Phi = 0$ .  $\Phi$  may be represented by a sum over spherical harmonics:

$$\Phi = \sum_{L,M} a_{LM} r^L Y_{LM}. \quad (5.4)$$

Of most interest to us are terms with  $M=0$ , as these have cylindrical symmetry.

---

<sup>1</sup> Again, one may also apply a positive voltage to two neighbouring electrodes while the two electrodes in the same plane are kept at a negative voltage and the remaining two electrodes are at ground.

Looking only at these terms, we write

$$\Phi = \Phi_0 + \Phi_1 \frac{z}{z_0} + \Phi_2 \frac{(z^2 - \rho^2/2)}{z_0^2} + \Phi_3 \frac{(z^3 - \frac{3}{2}z\rho^2)}{z_0^3} \dots, \quad (5.5)$$

with  $z_0$  a scaling factor that characterizes the size of the electrode structure. The first term in equation 5.5 represents a constant voltage, the second term represents a constant electric field and the third and fourth term represent a quadrupole and hexapole trap, respectively. The voltage at  $\rho = 0, z = z_0$ , is simply the sum over all coefficients, i.e.,  $\Phi(z = z_0, \rho = 0) = \sum \Phi_n$  with the subscript  $n$  denoting the different terms in equation 5.5. The electric field magnitude at the center is given by  $E_0 = \Phi_1/z_0$ . As discussed in section 5.2, we require the magnitude of the electric field to be non-zero at the center of the trap, and symmetric under reflection in the x-y plane and in any plane containing the z axis. To achieve this we retain only terms of odd  $n$ <sup>1</sup>. Anticipating the result that high-order terms introduce undesirable non-linearities in the force, we choose to retain only  $\Phi_1, \Phi_3$  and  $\Phi_5$ . Hence

$$\Phi = \Phi_0 + \Phi_1 \frac{z}{z_0} + \Phi_3 \frac{(z^3 - \frac{3}{2}z\rho^2)}{z_0^3} + \Phi_5 \frac{(z^5 - 5z^3\rho^2 + \frac{15}{8}z\rho^4)}{z_0^5}. \quad (5.6)$$

The electric field magnitude,  $E(z, \rho) = \sqrt{\left(\frac{\partial \Phi}{\partial z}\right)^2 + \left(\frac{\partial \Phi}{\partial \rho}\right)^2}$  can be obtained from this potential. Throughout the region  $z < z_0, \rho < z_0$  this can be expanded as a power series. For the case  $\Phi_5 \ll \Phi_3 \ll \Phi_1$  we obtain

$$E(z, \rho) = E_0 \left( 1 + 3 \left( \frac{\Phi_3}{\Phi_1} \right) \frac{(z^2 - \frac{1}{2}\rho^2)}{z_0^2} + \left( \frac{\Phi_3}{\Phi_1} \right)^2 \frac{(\frac{9}{2}z^2\rho^2)}{z_0^4} + 5 \left( \frac{\Phi_5}{\Phi_1} \right) \frac{(z^4 - 3z^2\rho^2 + \frac{3}{8}\rho^4)}{z_0^4} \dots \right). \quad (5.7)$$

The first two terms have the desired form and dominate the expansion. The other terms produce non-linearities in the force, that, as we will see in section 5.6, limit the trap-depth. The field ideally contains only a  $\Phi_1$  and  $\Phi_3$  term.

Before looking at how we can create such a field we will first turn our attention to atoms and molecules that experience a quadratic Stark shift. In

---

<sup>1</sup>Even terms will cause the force to be non-zero at the center of the trap. Peik [114] considered a small  $n=2$  term to compensate the gravitational force on the atoms. In the case of polar molecules, the trap depth is so large that gravity can be neglected.



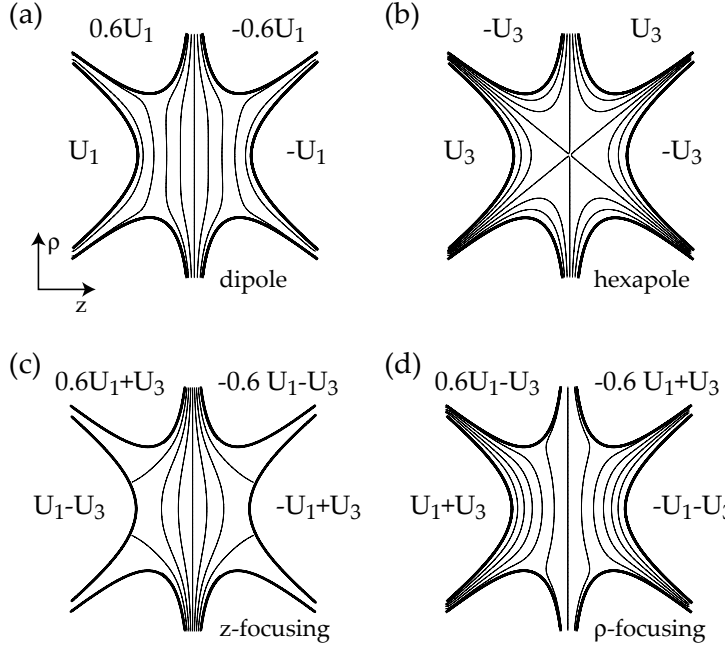


Figure 5.2: Electrostatic potential obtained by applying different voltages to the electrodes of a cylindrical hexapole trap. (a) Dipole field. (b) Hexapole field. (c)  $z$ -focusing, obtained by subtracting a hexapole field from a dipole field. (d)  $\rho$ -focusing, obtained by adding a hexapole field to a dipole field.  $U_1$  is taken to be equal to  $3U_3$ .

this case the electric field needs to be of the form  $E^2(z, \rho) = E_0^2 + \eta(z^2 - \frac{1}{2}\rho^2)$ . In a similar fashion we write  $E^2$  in a power series as:

$$\begin{aligned}
E^2(z, \rho) = & E_0^2 \left( 1 + 6 \left( \frac{\Phi_3}{\Phi_1} \right) \frac{(z^2 - \frac{1}{2}\rho^2)}{z_0^2} + \right. \\
& 2 \left( \frac{\Phi_3}{\Phi_1} \right)^2 \frac{(\frac{9}{2}z^2\rho^2)}{z_0^4} + 9 \left( \frac{\Phi_3}{\Phi_1} \right)^2 \frac{(z^2 - \frac{1}{2}\rho^2)^2}{z_0^4} + \\
& \left. 10 \left( \frac{\Phi_5}{\Phi_1} \right) \frac{(z^4 - 3z^2\rho^2 + \frac{3}{8}\rho^4)}{z_0^4} \dots \right). \tag{5.8}
\end{aligned}$$

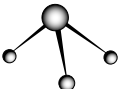
Again, we see that the field ideally contains only a  $\Phi_1$  and  $\Phi_3$  term. Compared to the case of a linear Stark shift, the potential contains extra terms in  $(\Phi_3/\Phi_1)^2$ , causing stronger deviations from a harmonic force.

In order to create the desired fields, we use the electrode configuration shown in figure 5.2. The surfaces of the electrodes, indicated by the bold curves in

figure 5.2, are mapped onto the equipotentials of a cylindrical hexapole field. Consequently, when voltages of  $U_3$  and  $-U_3$  are applied alternately to the four electrodes of the trap as shown in figure 5.2(b), a perfect hexapole field is obtained, i.e.,  $\Phi_3 = U_3$ , and  $\Phi_n = 0$ , for  $n \neq 3$ . In order to generate a dipole term we apply voltages of  $-U_1$ ,  $-0.6U_1$ ,  $0.6U_1$  and  $U_1$  to the electrodes as shown in figure 5.2(a). Fitting this field to equation 5.5 yields  $\Phi_1 = 0.88U_1$ ,  $\Phi_3 = 0$  and  $\Phi_5 = 0.11U_1$ , with even terms being zero due to symmetry. For AC trapping, we apply a large dipole term and add (or subtract) a small time-varying hexapole field. Figure 5.2(c) shows the electrostatic potential when we subtract the hexapole field from the dipole field, with  $U_1 = 3U_3$ . Along  $z$ , the electric field has a maximum at the center. Along  $\rho$ , the electric field has a minimum at the center. Molecules in high-field-seeking states will be focused along  $z$  and defocused along  $\rho$ , and we will refer to this configuration as ‘ $z$ -focusing’. Figure 5.2(d) shows the electrostatic potential when we add the hexapole field to the dipole field, again with  $U_1 = 3U_3$ . Along  $\rho$  the electric field has a maximum at the center. Along  $z$ , the electric field has a minimum at the center. Molecules in high-field-seeking states will be focused along  $\rho$  and defocused along  $z$ , and we will refer to this configuration as ‘ $\rho$ -focusing’.

The electric fields generated in this way contain a rather sizable  $\Phi_5$  term that makes the force more non-linear. Unfortunately, to decrease the  $\Phi_5$  term present in the  $z$ -focusing field, we need to bring the electrodes closer together and increase the radii of the ring electrodes, whereas to decrease the  $\Phi_5$  term present in the  $\rho$ -focusing field, we need to move the electrodes further apart and decrease the radii of the ring electrodes. Improving the linearity of one configuration thus unavoidably results in deteriorating the linearity of the other. The use of a hexapole trap is a compromise, forced by the need to adjust only the voltages when reversing the focusing and defocusing directions.

Figure 5.3(a) schematically shows the practical realization of our trap. The electrodes are truncated to avoid the distance between them becoming too small. The two end caps are placed a distance  $2z_0 = 9.1$  mm apart. The two ring electrodes have a radius equal to  $\sqrt{3/2}z_0 = 5$  mm. Both end-caps have been given a hole with a 2 mm diameter to allow molecules to enter the trap and to extract ions that are produced in our laser-based detection scheme. In our experiment we use  $U_1 = 8$  kV and  $U_3 = 3$  kV, resulting in voltages of 5, 7.5, -7.5, and -5kV ( $z$ -focusing) or 11, 1.6, -1.6, and -11kV ( $\rho$ -focusing) being applied to the electrodes. Fitting these fields to equation 5.5 yields  $\Phi_1 = 7.0$  kV,  $\Phi_3 = -3.0$  kV and  $\Phi_5 = 0.88$  kV ( $z$ -focusing) and  $\Phi_1 = 7.0$  kV,  $\Phi_3 = 3.0$  kV and  $\Phi_5 = 0.62$  kV ( $\rho$ -focusing). The resulting electric field magnitude as a function of the position along  $z$  and  $\rho$  is shown in figure 5.3(b) and (c), respectively. In the center of the trap the electric field magnitude is 16 kV/cm. Figure 5.3(d) and (e) show the corresponding force exerted on ammonia molecules in the high-field-seeking component of the  $|J, K\rangle = |1, 1\rangle$  level along the  $z$  and  $\rho$  axis, respectively. For ease of comparison the force in the  $\rho$ -focusing configuration in figure 5.3(d) and the force in the  $z$ -focusing



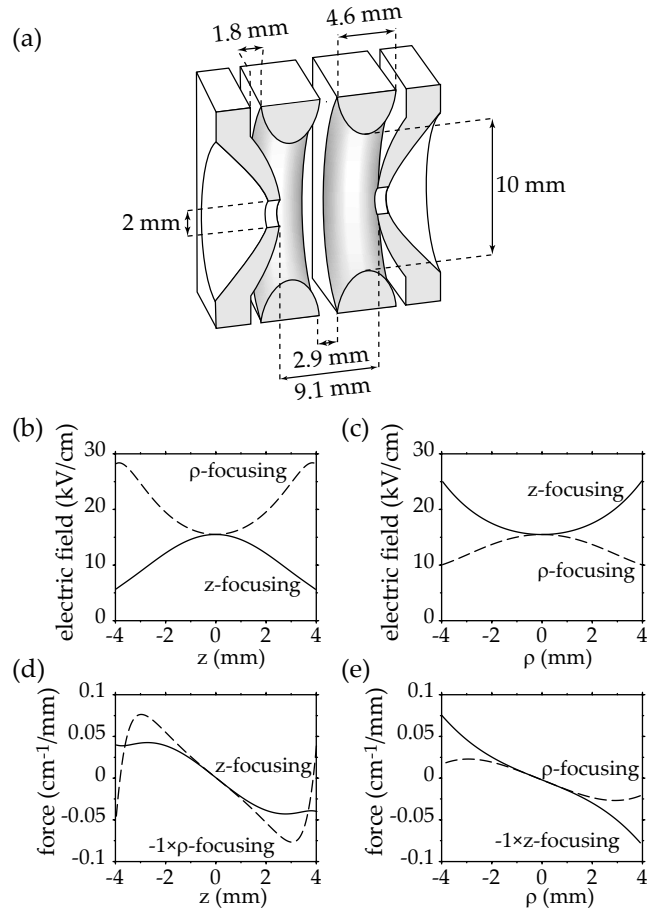


Figure 5.3: (a) Schematic view of the cylindrical symmetric AC trap used in our experiments. (b) and (c) Electric field magnitude as a function of the position along  $z$  (b) and  $\rho$  (c) when voltages of 5, 7.5, -7.5, and -5kV ( $z$ -focusing) or 11, 1.6, -1.6, and -11kV ( $\rho$ -focusing) are applied to the electrodes. (d) and (e) Force on ammonia molecules in the high-field-seeking component of the  $|J, K\rangle = |1, 1\rangle$  level along  $z$  (d) and  $\rho$  (e).

configuration in figure 5.3(e) are multiplied by -1. It is seen that the focusing and defocusing forces are equal at the center of the trap and that close to the center they are roughly linear, with the force constants given by

$$|k_\rho| = |k_z/2| = \frac{3\mu_{\text{eff}}\Phi_3}{z_0^3}. \quad (5.9)$$

With  $\mu_{\text{eff}}=0.0126 \text{ cm}^{-1}/\text{kV/cm}$  the effective dipole moment of  $^{15}\text{ND}_3$  we find  $|k_z|=0.024$  and  $|k_\rho|=0.012 \text{ cm}^{-1}/\text{mm}^2$ . Further away from the center, the non-linearity due to  $\Phi_5$  acts to strengthen the defocusing power whereas the focusing is weakened. We will see later that this non-linearity severely reduces the depth of the trap.

## 5.5 Motion in the trap

In this section, the motion of molecules in the trap is investigated and the trap depth is determined as a function of the applied frequency<sup>1</sup>. We start by assuming that the molecules experience a linear force that is alternately focusing and defocusing. Let us examine the motion along one of the principal axes of the trap, say the x axis. The equation of motion can be written as

$$m\partial^2 x/\partial t^2 + k(t)x = 0, \quad (5.10)$$

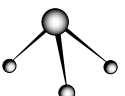
with  $m$  the mass of the molecule and  $k(t)$  the force constant. We will apply a square wave voltage to the trap such that  $k(t)$  is equal to  $k$  during the time interval  $(0, \frac{1}{2}T)$  and equal to  $-k$  during the time interval  $(\frac{1}{2}T, T)$ . In this case equation 5.10 has a piecewise solution and is known as Hill's equation [165]. When  $k$  is positive, the molecule will oscillate with a frequency  $\Omega_{\text{hex}} = \sqrt{|k|/m}$  around the center of the trap;  $x(t) = x(t_0) \cos \Omega_{\text{hex}}(t - t_0) + v_x(t_0) \Omega_{\text{hex}}^{-1} \sin \Omega_{\text{hex}}(t - t_0)$ , with  $x(t_0)$  and  $v_x(t_0)$  the initial position and velocity of the molecule, respectively. As the oscillation frequency is a function of the hexapole term we denote it with subscript 'hex'. When  $k$  is negative, the amplitude will grow exponentially;  $x(t) = x(t_0) \cosh \Omega_{\text{hex}}(t - t_0) + v_x(t_0) \Omega_{\text{hex}}^{-1} \sinh \Omega_{\text{hex}}(t - t_0)$ . The solution of the equation of motion is conveniently written in matrix form as

$$\begin{pmatrix} x(t) \\ v_x(t) \end{pmatrix} = M(t|t_0) \begin{pmatrix} x(t_0) \\ v_x(t_0) \end{pmatrix}. \quad (5.11)$$

with the transfer matrix  $M(t|t_0)$  given by

$$M(t|t_0) = \begin{cases} \begin{pmatrix} \cos \Omega_{\text{hex}}(t - t_0) & \Omega_{\text{hex}}^{-1} \sin \Omega_{\text{hex}}(t - t_0) \\ -\Omega_{\text{hex}} \sin \Omega_{\text{hex}}(t - t_0) & \cos \Omega_{\text{hex}}(t - t_0) \end{pmatrix} & F \\ \begin{pmatrix} \cosh \Omega_{\text{hex}}(t - t_0) & \Omega_{\text{hex}}^{-1} \sinh \Omega_{\text{hex}}(t - t_0) \\ \Omega_{\text{hex}} \sinh \Omega_{\text{hex}}(t - t_0) & \cosh \Omega_{\text{hex}}(t - t_0) \end{pmatrix} & D \end{cases} \quad (5.12)$$

<sup>1</sup> AC trapping of polar molecules is closely related to focusing beams of polar molecules using arrays of electrostatic lenses in alternating gradient (AG) configuration. For a description of the motion of molecules in an AG decelerator, see [108].



The transfer matrix is called  $F$  when the force is focusing and  $D$  when the force is defocusing.

The transfer matrix for any interval made up of subintervals is just the product of the transfer matrices of the subintervals:

$$M(t_2|t_0) = M(t_2|t_1)M(t_1|t_0). \quad (5.13)$$

The transfer matrix for a single cycle is  $F(T|\frac{1}{2}T) \cdot D(\frac{1}{2}T|0)$ . The transfer matrix for  $N$  cycles is simply  $M = (F(T|\frac{1}{2}T) \cdot D(\frac{1}{2}T|0))^N$ . In order for molecules to be stably trapped, it is necessary that all the elements of this transfer matrix remain bound when  $N$  increases indefinitely. This is the case when  $-1 < \frac{1}{2}Tr(M) < +1$  (see, for example, [166]).

It is useful to parametrize the transfer matrix for one cycle as [102]

$$M(t+T|t) = \begin{pmatrix} \cos \Phi + \alpha \sin \Phi & \beta \sin \Phi \\ -\gamma \sin \Phi & \cos \Phi - \alpha \sin \Phi \end{pmatrix}, \quad (5.14)$$

where  $\alpha(t)$ ,  $\beta(t)$  and  $\gamma(t)$  are the Courant-Snyder parameters. It can be shown that the distribution of the molecules in phase-space is given by the Courant-Snyder phase-space ellipse:

$$\gamma(t)x^2 + 2\alpha(t)xv_x + \beta(t)v_x^2 = \epsilon, \quad (5.15)$$

with  $\epsilon$  a constant which is called the emittance. The area enclosed by the Courant-Snyder ellipse is  $\pi\epsilon$ . The maximum position spread of a sample of trapped molecules with emittance  $\epsilon$  is  $\sqrt{\beta\epsilon}$ . The maximum velocity spread of the trapped sample is  $\sqrt{\gamma\epsilon}$ .  $\Phi$  is the phase advance per cycle, which is a measure for how far along the period a molecule has proceeded from its initial position. We see that the stability criterion is identical to requiring  $\Phi$  to be real.

In figure 5.4 some trajectories in the trap are plotted as a function of time for two different values of the frequency of the applied voltage,  $\Omega_{\text{driven}}$ . The time is given in units of  $T = 2\pi/\Omega_{\text{driven}}$ , and the position is given in units of  $d$ , the distance between the trap electrodes along  $x$ . For the trajectories shown in figure 5.5(a)  $\Omega_{\text{driven}}/\Omega_{\text{hex}} = 3.3$ , which corresponds to a phase-advance of  $\pi/6$ , implying that molecules return to their starting point after 12 cycles of the driving field. In the lower panel trajectories are shown for  $\Omega_{\text{driven}}/\Omega_{\text{hex}} = 2.0$ , which corresponds to a phase-advance of  $\pi/2$ , implying that molecules return to their starting point after 4 cycles of the driving field. The gray shaded area shows the size of the trapped cloud, bounded by  $\pm\sqrt{\beta\epsilon}$ . It can be seen that molecules are on average further away from the center of the trap when the force is focusing than when the force is defocusing. This is the origin of the stability of the trap. At any fixed position, the divergence of the force averaged over one cycle,  $(1/T)(\partial/\partial x) \int_0^T F(x)dt$ , is equal to zero. However, a molecule does not stay at a fixed position, but will move towards the center of the trap

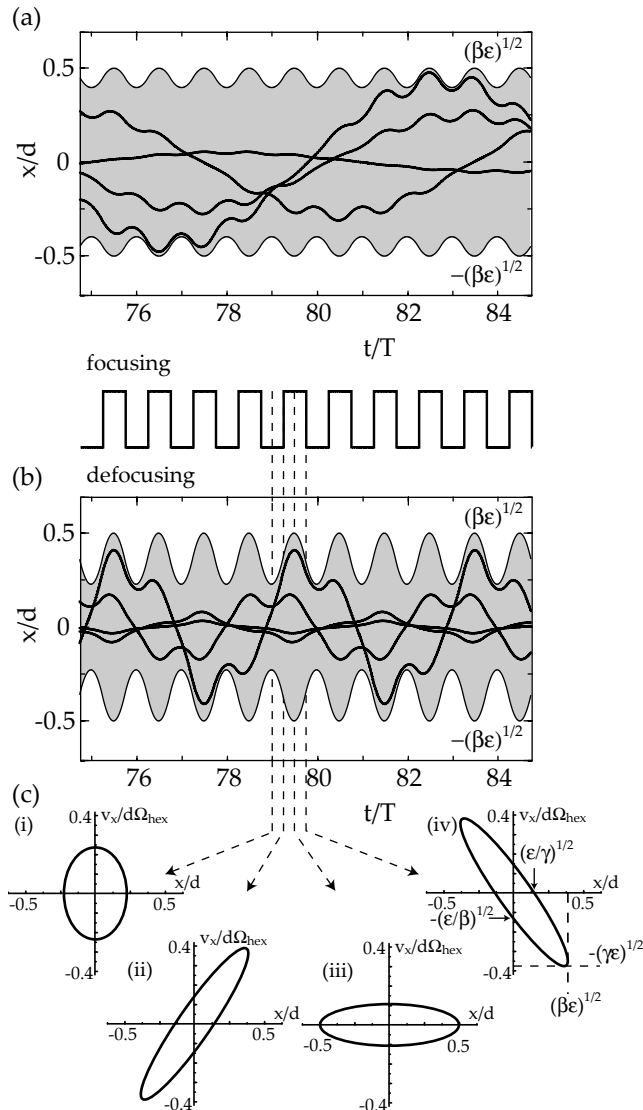
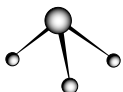


Figure 5.4: (a) Trajectories of ammonia molecules in an AC-trap for  $\Omega_{\text{driven}}/\Omega_{\text{hex}} = 3.3$  corresponding to a phase advance of  $\pi/6$ . The time is given in units of  $T = 2\pi/\Omega_{\text{driven}}$ , and the position is given in units of  $d$ , the distance between the trap electrodes along  $x$ . (b) As (a), but with  $\Omega_{\text{driven}}/\Omega_{\text{hex}} = 2$ , corresponding to a phase advance of  $\pi/2$ . (c) Phase-space area occupied by the trapped molecules at four times in a single cycle. The position is given in units of  $d$  and the velocity in units of  $d\Omega_{\text{hex}}$ .



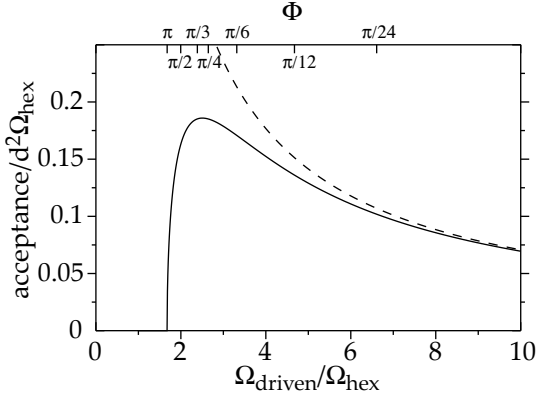


Figure 5.5: The acceptance of the trap in units of  $d^2\Omega_{\text{hex}}$  as a function of the applied frequency in units of  $\Omega_{\text{hex}}$  calculated using the matrix method (solid line), and using an effective potential (dashed line). On the top the phase advance corresponding to some values of  $\Omega_{\text{driven}}/\Omega_{\text{hex}}$  is shown.

under the influence of the focusing force. It will then be closer to the center, where the force is smaller, when the defocusing force is applied. This defocusing force will move the molecule further away from the center again, bringing it in a region of a larger force when the focusing force is applied. As a consequence, the divergence of the force averaged over the trajectory of the molecule over one cycle,  $(1/T)(\partial/\partial x) \int_0^T F(x(t))dt$ , is less than zero. As this is a result of the motion of the molecule, this is commonly referred to as ‘dynamic’ stability. For small values of  $\Phi$ , the motion can be separated in a rapid oscillation – analogous to the ‘micro motion’ in ion traps [162] – at  $\Omega_{\text{driven}}$ , the frequency of the applied fields, and a slower oscillation – analogous to the ‘macro’ or ‘secular’ motion in ion traps – at  $\Omega_{\text{driven}}\Phi/2\pi$ .

In figure 5.4(c) the phase-space area occupied by the trapped molecules is shown at four different phases of the driving field. This area is enclosed by the Courant-Snyder ellipse given by equation 5.15 and is equal to ( $\pi$  times) the emittance. The phase space ellipse rotates at the frequency of the applied field. Both the velocity spread and the position spread of the trapped cloud oscillate but the product of the two – the emittance – remains constant. We will use the largest emittance that can be accepted by the trap – the acceptance – as a measure for the trap depth.

The solid line in figure 5.5 shows the 1D acceptance calculated from the matrix model as a function of the frequency of the applied fields. The acceptance is given in units of  $d^2\Omega_{\text{hex}}$ . At low frequencies, the trajectories of the molecules are unstable ( $\Phi$  is imaginary) and the acceptance is zero. Above  $\Omega_{\text{driven}}/\Omega_{\text{hex}} = 1.67$ , corresponding to  $\Phi = \pi$ , the trap becomes abruptly sta-

ble. When the frequency is increased further, the molecules have less time to move in between switching times. Their amplitudes when the force is focusing and defocusing approach each other and the net force on the molecules averages out more (compare figure 5.4(a) and (b)). As a result, the acceptance decreases at higher frequencies. The highest acceptance is  $0.186d^2\Omega_{\text{driven}}$ , obtained when  $\Omega_{\text{driven}}/\Omega_{\text{hex}} = 2.5$ . This may be compared to a DC hexapole trap for low-field seekers which has an acceptance of  $(\pi/4)d^2\Omega_{\text{hex}}$ ; over four times larger.

It is instructive to compare the trap operated with a square wave to a trap operated with a sinusoidal function with the same amplitude ( $k(t) = k \sin \Omega_{\text{driven}} t$ ). In this case equation 5.10 reduces to the well-known Mathieu equation [114, 165]:

$$\frac{d^2x}{d\tau^2} + (a - 2q_x \cos 2\tau)x = 0, \quad (5.16)$$

with

$$a = 0; \quad q_x = \frac{2\Omega_{\text{hex}}^2}{\Omega_{\text{driven}}^2}; \quad \tau = \frac{\Omega_{\text{driven}}t}{2}. \quad (5.17)$$

When  $a = 0$ , solutions of the Mathieu equation are stable when  $|q_x| < 0.907$ ; i.e., when  $\Omega_{\text{driven}}/\Omega_{\text{hex}} > 1.48$ . By comparing the acceptance found by numerically integrating equation 5.16 to the acceptance of the trap operated with a square wave, we find that the two are identical when  $\Phi_3$  is multiplied by a factor 1.27, (and consequently  $\Omega_{\text{hex}}$  is multiplied by a factor 1.12) when operating the trap with a square wave. This factor is equal to  $4/\pi$  and can be understood by expanding the square wave in a Fourier series. Molecules will mainly interact with the first term in the expansion, which has a Fourier coefficient equal to  $4/\pi$  [167]. This is similar to the description of the longitudinal motion in a Stark decelerator in terms of traveling waves [168].

At high frequencies,  $\Omega_{\text{driven}}/\Omega_{\text{hex}} \gg 1$ , the micromotion is much faster than the secular motion. In this limit, it is possible to derive a static ‘pseudo’ potential,  $\bar{W}$  [114, 169, 170]. Again using the fact that for a square wave  $\Omega_{\text{hex}}$  should be multiplied by  $\sqrt{4/\pi}$ , we find:

$$\bar{W} = \frac{4}{\pi^2} m \frac{\Omega_{\text{hex}}^4}{\Omega_{\text{driven}}^2} x^2. \quad (5.18)$$

The secular motion in this pseudo potential is a harmonic oscillation with frequency

$$\omega_{\text{secular}} = \frac{2\sqrt{2}}{\pi} \frac{\Omega_{\text{hex}}^2}{\Omega_{\text{driven}}}. \quad (5.19)$$

The acceptance of the pseudo potential is given by:

$$\text{acceptance} = \frac{\pi}{4} d^2 \omega_{\text{secular}} = \frac{1}{\sqrt{2}} d^2 \frac{\Omega_{\text{hex}}^2}{\Omega_{\text{driven}}}. \quad (5.20)$$



Equation 5.20 is shown as the dotted line in figure 5.5. We see that the acceptance can be reasonably well estimated from the pseudo potential for  $\Omega_{\text{driven}}/\Omega_{\text{hex}} > 7$  ( $q < 0.04$ ).

In our cylindrical trap, shown in figure 5.3, the hexapole frequencies along  $z$  and  $\rho$  are  $\Omega_{\text{hex},z}/2\pi=590$  Hz and  $\Omega_{\text{hex},\rho}/2\pi=417$  Hz, respectively. As a consequence, the phase advance along  $z$  and  $\rho$  are different at a given frequency. The trap can be made isotropic by switching the fields such that the configuration which focuses molecules along the  $\rho$  direction is on for a longer time than the configuration that focuses molecules along the  $z$  direction. We will define a duty cycle that is equal to 0% when  $\rho$ -focusing is continuously on, and equal to 100% when  $z$ -focusing is continuously on. In order to obtain an isotropic trap, the duty cycle should be adjusted such that  $\Phi_z=\Phi_\rho$  at each frequency. In the experiments presented in section 5.6 the duty cycle is modified either in this fashion or by using an approximated formula.

## 5.6 Trapping ammonia molecules in a cylindrical AC trap

The experimental setup used for AC trapping of ammonia molecules is depicted schematically in figure 5.6. It consists of two differentially pumped vacuum chambers separated by a 1 mm diameter skimmer. In the first chamber a molecular beam is made by expanding a mixture of 5%  $^{15}\text{ND}_3$  molecules seeded in xenon. The molecular beam is then passed through a Stark decelerator consisting of 95 electrode pairs. Molecules in the low-field-seeking component of the  $|J, K\rangle = |1, 1\rangle$  level of  $^{15}\text{ND}_3$  are decelerated to around 15 m/s. This part of the set-up and the operation principle of the decelerator have been described in more detail in sections 3.2 and 3.3, and in reference [148]. The slow molecules exiting the decelerator are focused into the AC trap using a 12.5 mm long linear hexapole focuser and a cylindrical hexapole trap. The hexapole trap is almost identical to the AC trap depicted in figure 5.3. By applying a voltage of 5 kV to the first ring electrode and the last end cap while keeping the other electrodes at ground an electric field is created that is zero at the center, and increases quadratically away from the center. By switching this field on and off when the molecules fly through it, molecules are focused along  $\rho$  and bunched along the  $z$  direction [148]. Using the linear hexapole focuser and cylindrical hexapole trap we make a 3D image of the packet exiting the Stark decelerator at the center of the AC trap. For molecules having a linear Stark effect the force inside the linear and cylindrical hexapole is perfectly harmonic and the imaging can be performed without distortion. Due to the inversion splitting in  $^{15}\text{ND}_3$ , the force is non-linear, causing the image to be distorted. As the acceptance of the trap is smaller than the phase-space volume of the beam exiting the decelerator (the emittance) most of the molecules that are lost would not be trapped anyway. When the packet of slow ammonia molecules

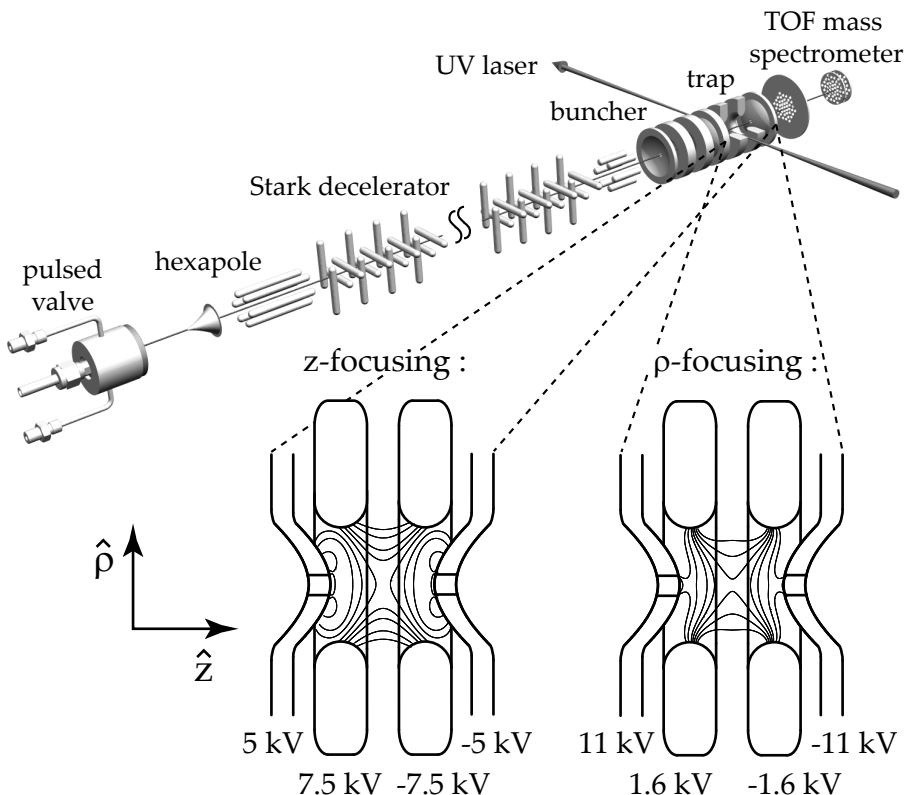


Figure 5.6: Experimental setup. A molecular beam of  $^{15}\text{ND}_3$  molecules in the low-field-seeking component of the  $|J, K\rangle = |1, 1\rangle$  level is decelerated and loaded in the AC electric trap. Using a microwave pulse, molecules are transferred to the high-field-seeking state and subsequently trapped. Below the setup, two cross sections of the trap are shown along with the voltages used in the experiment for both the  $z$ - and  $\rho$ -focusing configuration. The thinner lines indicate the field lines resulting from these voltages.



enters the trap, we apply voltages of 7.5, 5, 0, and -11 kV to the electrodes of the AC trap. This creates an electric field that is small at the entrance of the trap and increases towards the center of the trap. Molecules with a forward velocity of 15 m/s will come to a standstill at the center of the trap. At that time, the high voltages on the trap are switched off and only the voltages used for extracting the ions remain. Using a 20  $\mu$ s long microwave pulse, the transition from the low-field-seeking to the high-field-seeking hyperfine levels in the  $|J, K\rangle = |1, 1\rangle$  state of  $^{15}\text{ND}_3$  can be induced (see also chapters 2 and 3). In zero electric field this transition is centered at 1.43 GHz (see chapter 3). In the approximately 600 V/cm extraction field, this transition is shifted to 1.46 GHz. The microwave radiation is generated by a Rohde & Schwartz (SMR27) signal generator. Under optimum conditions, about 20% of the ammonia molecules are pumped to high-field-seeking levels. When the AC electric trap is switched on, the voltages on the trap are alternated at a frequency  $\Omega_{\text{driven}}$  between the two configurations shown in figure 5.3. The frequency is generated by a function generator (Agilent 33220A) that triggers a total of 8 high voltage switches (Behlke HTS201-03-GSM). The voltages are delivered by 8 FUG (HCK400-20000) high voltage power supplies. After a certain trapping time, the trap is switched off, and the molecules are detected using pulsed UV-laser ionization followed by mass-selective detection of the parent ions. The (2+1)-Resonance Enhanced Multi Photon Ionization (REMPI) scheme that is used selectively ionizes the  $^{15}\text{ND}_3$  molecules in the upper or lower component of the  $|J, K\rangle = |1, 1\rangle$  inversion doublet, containing the low-field-seeking or high-field-seeking levels, respectively (see also figure 2.5 at page 27).

In figure 5.7 the ion signal is shown as a function of the switching frequency for molecules in low-field-seeking and high-field-seeking states. For clarity, the signal for molecules in low-field-seeking states has been given an offset. The signal for the high-field seekers is scaled up by a factor of five, to correct for the 20% conversion efficiency in the microwave pumping process. The time the laser is fired is adjusted to be in phase with the switching frequency. Therefore, the time that the trap is on depends on the applied frequency but is always chosen to be close to 80 ms. The measurements agree with the qualitative description of the dependence of the stability of the trap on  $\Omega_{\text{driven}}$  as described in section 5.5. As we detect only molecules in the laser focus, our signal reflects the density at the center of the trap rather than the total number of molecules that are trapped. The signal is therefore not proportional to the acceptance but rather proportional to  $\sqrt{1/\beta_z} \cdot 1/\beta_\rho$ , with  $\beta$  the Courant-Snyder  $\beta$ -coefficient introduced in section 5.5 (see figure 5.4). This function is shown as the bold line in figure 5.7. The thin line, also shown in figure 5.7, results from a numerical simulation of the experiment using the true (non-linear) force on the molecules. In the simulation the phase-space in the trap is assumed to be homogeneously filled, i.e., it is assumed that the phase-space volume of the molecules exiting the decelerator is much larger than the acceptance of the trap. Both curves have been scaled to match the signal for high-field seekers at  $\Omega_{\text{driven}}/2\pi$ . The

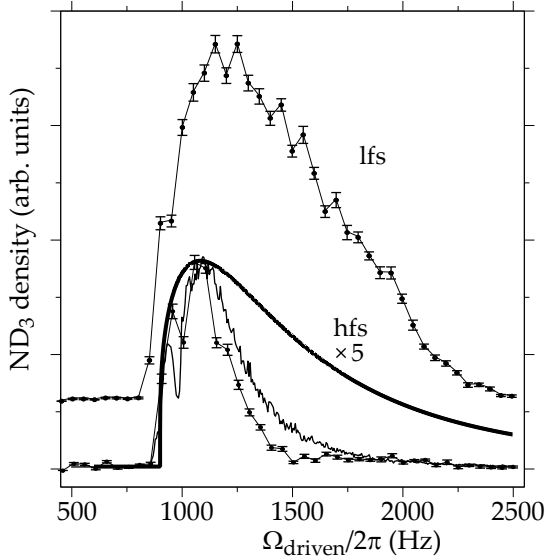
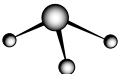


Figure 5.7: Density of  $^{15}\text{ND}_3$  molecules in low-field-seeking (lfs) and high-field-seeking levels (hfs) of the  $|J, K\rangle = |1, 1\rangle$  state at the center of the trap as a function of the switching frequency, after the trap has been on for about 80 ms. The signal of the high-field seekers is scaled up by a factor of 5. The solid line shows the result of a numerical simulation of the experiment.

experimentally found cut-off frequency is around 900 Hz, in good agreement with both the linear model and the simulation. Note that the cut-off frequency for the high-field seekers is slightly higher than for the low-field seekers due to an about 4% difference in the magnitude of  $\mu_{\text{eff}}$  in the electric field at the center of the trap. With the present settings, the highest density of trapped molecules is observed at a switching frequency of 1100 Hz, again in agreement with the calculations. At higher frequencies the signal decreases. The measured decrease is faster than predicted from the linear model. This is due to the higher order terms in equation 5.7 giving rise to a (frequency independent) potential that lowers the trap depth for molecules in high-field-seeking states and increases the trap depth for molecules in low-field-seeking states. As seen, the experimentally observed density drops more rapidly than expected from the numerical simulation using the true force. We believe that the remaining difference is caused by a slight misalignment of our trap electrodes (vide infra). This also explains the rapid decrease in signal of molecules in low-field seeking states at higher frequencies. Note the dip in the measured and simulated curves around 1000 Hz due to non-linear couplings that cause instabilities, also observed in ion traps [171].



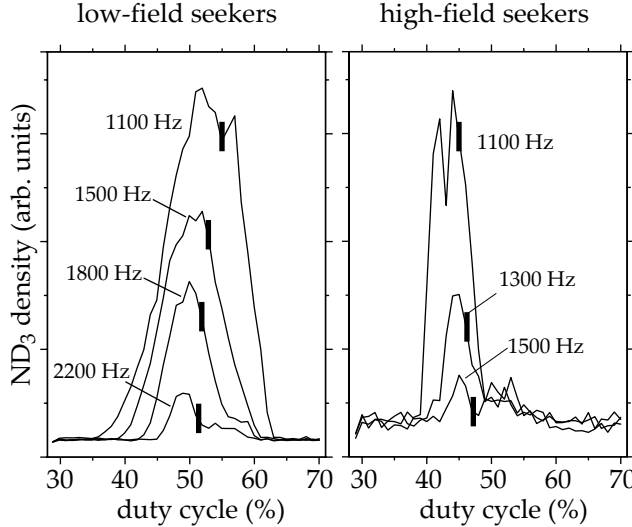


Figure 5.8: Density of  $^{15}\text{ND}_3$  molecules in the low-field-seeking (left column) and high-field-seeking state (right column) at the center of the trap as a function of the duty cycle for a number of different values of the applied frequency. The vertical lines show the value of the duty cycle for which the phase advance along  $z$  and  $\rho$  are equal.

Figure 5.8 shows the density at the center of the trap as a function of the duty cycle for a number of values of the frequency of the applied fields. The left column shows the measurements taken for molecules in low-field-seeking states and the right column those for molecules in high-field-seeking states. As expected, the density is increased when the trap depth along  $\rho$  is increased at the cost of a decrease of the trap depth along  $z$ . The vertical lines show the value of the duty cycle for which the phase advance along  $z$  and  $\rho$  are equal for the different frequencies. As can be seen, the vertical lines are always positioned at a duty cycle that is 3% higher than the maximum. We believe this is due to a slight misalignment of the electrodes which effectively adds an extra hexapole term – adding a force that is focusing along the  $z$  direction and defocusing along  $\rho$  for high-field-seeking states and vice versa for molecules in low-field-seeking states. This misalignment was also observed in an experiment on trapping molecules in a double-well potential performed in the same setup, as described in chapter 4.

In our experiment, we use a tightly focused laser beam for detecting the molecules. This allows us to measure the spatial profile of the trapped molecules by scanning the position of the laser focus. Figure 5.9 shows measurements of the spatial distribution along the  $z$  direction for molecules in high-field-seeking

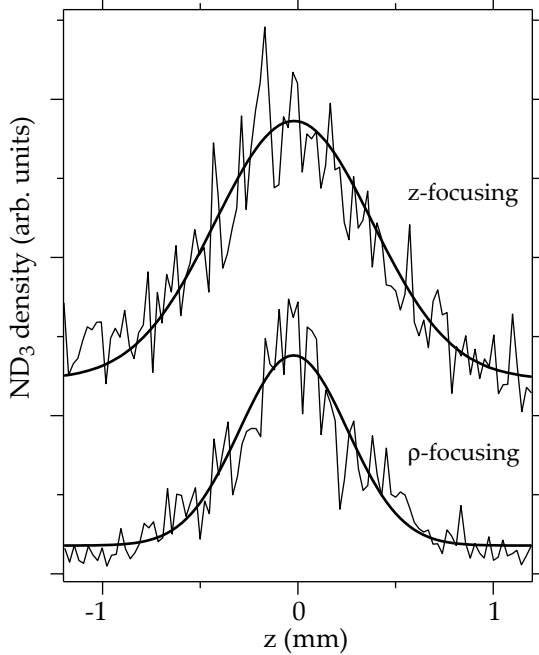
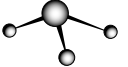


Figure 5.9: Spatial distribution along  $z$  of  $^{15}\text{ND}_3$  molecules in high-field-seeking states after 79 (lower) and  $79\frac{1}{2}$  (upper) cycles of the applied field with  $\Omega_{\text{driven}}/2\pi = 1100$  Hz and duty cycle = 45%. The bold line shows a Gaussian fit to the distribution.

states. The trap is operated with a frequency of  $\Omega_{\text{driven}}/2\pi = 1100$  Hz with a duty cycle equal to 45%. The spatial distribution is recorded after 79 (lower) and  $79\frac{1}{2}$  (upper) cycles of the applied field, corresponding to two of the vertical lines in figure 5.4(b). The bold line shows the result of a Gaussian fit to the distribution. As expected, the packet is larger when the force is focusing along  $z$  ( $z$ -focusing) than when the force along  $z$  is defocusing ( $\rho$ -focusing). Interestingly, the ion signal at  $z = 0$  is roughly equal in both cases. When the width of the packet along  $z$  is largest, the width along  $\rho$  is smallest, i.e., the cloud oscillates between a cigar shaped distribution and a pancake shaped distribution, while the density at the center stays approximately constant. Note that this depends on the duty cycle used in the experiment.

Figure 5.10 shows the full width at half maximum (FWHM) of the distribution of the trapped molecules as a function of the driving frequency. Shown are measurements after 79 ( $\nabla$ ) and  $79\frac{1}{2}$  ( $\Delta$ ) cycles of the applied field, corresponding to  $\rho$ -focusing and  $z$ -focusing, respectively. In the linear model, the width of the packet along  $z$  is proportional to  $\sqrt{\beta_z}$ , with  $\beta$  being the Courant-



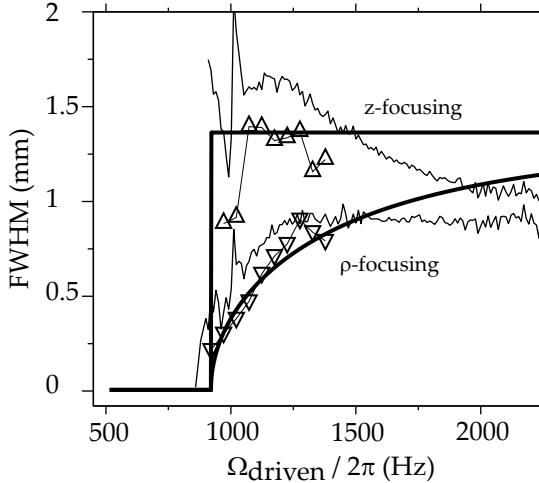


Figure 5.10: FWHM of the spatial distribution of the trapped molecules as a function of the drive frequency. The triangles show the measurements after 79 ( $\nabla$ ) and  $79\frac{1}{2}$  ( $\Delta$ ) cycles of the applied field. The bold curves show the result of the matrix model, the thin curves show the result from a numerical simulations including the true force.

Snyder  $\beta$ -coefficient introduced in section 5.5 (see figure 5.4). The bold curves in figure 5.10 show  $\sqrt{\beta_z}$  as a function of  $\Omega_{\text{driven}}$ . The curves have been scaled to match the experimentally found width at 1100 Hz. If the force is perfectly linear the width of the packet along  $z$  at  $z$ -focusing is limited by the physical dimensions of the trap and is constant over the whole frequency range over which the trap is stable. In contrast, the width along  $z$  at  $\rho$ -focusing depends strongly on the driving frequencies. At high frequency the width at  $\rho$ -focusing is equal to the width at  $z$ -focusing. At lower frequency the width of the packet along  $z$  at  $\rho$ -focusing decreases until it becomes zero at the cut-off frequency. In our trap the width of the packet is determined by the non-linearities in the force. The thin line in figure 5.10 results from a numerical simulation using the true force. The numerical simulation is seen to reproduce the measured widths – both the absolute value and the frequency dependence – rather well. We attribute the 20% difference between the measured and calculated width to the slight misalignment of the trap electrodes discussed earlier. Around  $\Omega_{\text{driven}}/2\pi = 1000$  Hz, the simulated width is seen to oscillate. This is caused by the non-linear resonance discussed earlier in connection to figure 5.7. At the resonance, the distribution of the trapped molecules at  $z$ -focusing is no longer correctly described by a single Gaussian profile. Rather, the distribution consists of a main peak with smaller side peaks.

At high frequency, we can use the effective well model for predicting the width of the packet. For molecules in high-field-seeking states the non-linear terms in equation 5.7 create a repulsive – frequency independent – potential. In order for molecules to stay trapped this potential must be balanced by the potential due to the AC force. Using equation 5.7 and 5.18, we find the resulting potential,  $W_{\text{secular}}$ :

$$W_{\text{secular}} = \frac{4}{\pi^2} m \frac{\Omega_{\text{hex},z}^4}{\Omega_{\text{driven}}^2} z^2 - \mu_{\text{eff}} E_0 \left( \frac{\Phi_5}{\Phi_1} \right) \frac{5z^4}{z_0^4}, \quad (5.21)$$

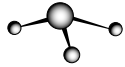
where the duty cycle is set at 50% and terms going beyond  $\Phi_5$  are ignored. The maximum extent of the packet is found by finding the position where the force on the molecules,  $-\partial W_{\text{secular}}/\partial z$ , becomes equal to zero:

$$z_{\max} = \sqrt{\frac{12}{5}} \frac{1}{\pi} \sqrt{\frac{\Phi_3}{\Phi_5}} \frac{\Omega_{\text{hex},z}}{\Omega_{\text{driven}}} z_0. \quad (5.22)$$

From equation 5.22, we find that the width of the spatial profile decreases as  $1/\Omega_{\text{driven}}$  in agreement with the numerical simulations shown in figure 5.10. At  $\Omega_{\text{driven}}/2\pi = 2000$  Hz, we find from equation 5.22  $z_{\max} = 1.2$  mm. When the duty cycle as used in the experiment is taken into account, we find  $z_{\max} = 0.9$  mm. This is the *maximum* extent of the packet and can therefore not be compared directly to the FWHM plotted in figure 5.10. From numerical simulation we find  $z_{\max} = 0.8$  mm.

We can determine the velocity distribution of the trapped molecules by measuring how rapidly the cloud expands after the trap has been switched off. In figure 5.11 the spatial distributions of  $^{15}\text{ND}_3$  molecules in high-field-seeking states are shown after an expansion time that is indicated in the figure. The molecules are released after 79 cycles of the applied field with  $\Omega_{\text{driven}}/2\pi = 1100$  Hz and duty cycle = 45%. The bold line shows the result of a Gaussian fit to the distribution. Similar measurements were taken for molecules released after  $79\frac{1}{4}$ ,  $79\frac{1}{2}$ , and  $79\frac{3}{4}$  cycles.

In figure 5.12 the FWHM that result from a Gaussian fit to the spatial distribution are shown as a function of the time after the molecules have been released from the trap. The trap is switched off after  $79$  ( $\nabla$ ),  $79\frac{1}{4}$  (+),  $79\frac{1}{2}$  ( $\Delta$ ) or  $79\frac{3}{4}$  ( $\times$ ) cycles of the applied field with  $\Omega_{\text{driven}}/2\pi = 1100$  Hz and duty cycle = 45%. These times correspond to those shown as the vertical lines in figure 5.4. As expected, if we release the molecules after 79 cycles of the applied field –when the field is focusing along  $\rho$ – the cloud starts off small, but expands rapidly. If we release the molecules after  $79\frac{1}{2}$  cycles of the applied field –when the field is focusing along  $z$ – the clouds starts off larger but expands less rapidly. After  $79\frac{1}{4}$  and  $79\frac{3}{4}$  cycles of the applied field the phase-space distribution is tilted with respect to the position and velocity axes. In both cases the velocity spread is larger than the velocity spread after 79 cycles of the applied field as is apparent from figure 5.4. Interestingly, after  $79\frac{3}{4}$  cycles the phase-space



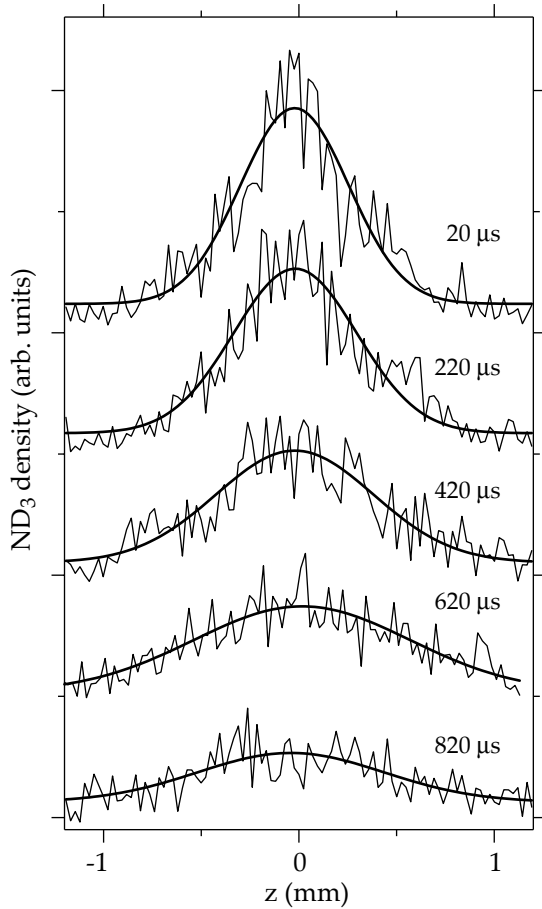


Figure 5.11: Spatial distributions of  $^{15}\text{ND}_3$  molecules in high-field-seeking states after having expanded for a time indicated in the figure. The molecules are released from the trap after 79 cycles of the applied field with  $\Omega_{\text{driven}}/2\pi = 1100$  Hz and duty cycle = 45%. The bold line shows the result of a Gaussian fit to the distribution.

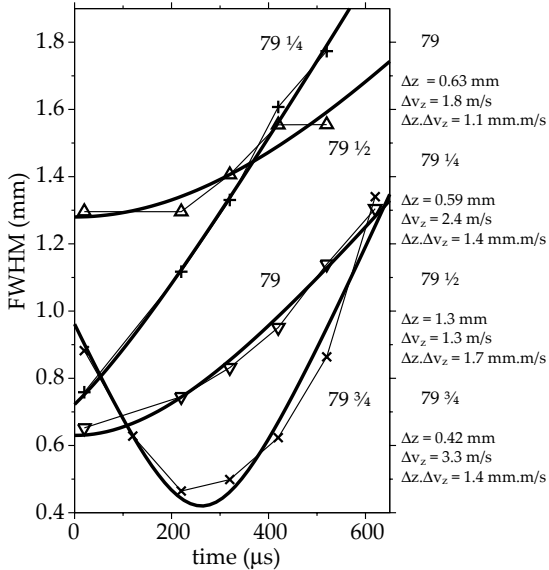


Figure 5.12: The FWHM that result from a Gaussian fit to the spatial distribution as a function of the expansion time. The molecules are released from the trap after  $79$  ( $\nabla$ ),  $79\frac{1}{4}$  (+),  $79\frac{1}{2}$  ( $\Delta$ ) or  $79\frac{3}{4}$  ( $\times$ ) cycles of the applied field with  $\Omega_{\text{driven}}/2\pi = 1100$  Hz and duty cycle = 45%. The bold curves show a square root formula fitted to the data.

distribution is tilted such that all molecules have a velocity towards the center of the trap, along the  $z$  axis of the trap. Therefore, at first the width along  $z$  becomes smaller and comes to a minimum about  $250 \mu\text{s}$  after the trap is switched off.

If we assume the velocity distribution to be Gaussian, the cloud expands as:

$$\Delta z(t) = \sqrt{(\Delta z(t=0))^2 + (\Delta v_z t)^2} \quad (5.23)$$

with  $\Delta z(t=0)$  the initial spatial distribution of the trapped molecules and  $\Delta v_z$  the velocity distribution. The bold curves show the fitted formula to the data. The fitted values for the velocity spread and the initial position spread are given in the figure. As the area of the phase-space distribution stays constant we expect  $\Delta z(t=0)$  times  $\Delta v_z$  to be constant. In actual effect, we find that the measured areas differ by more than 50%. Note that the determined velocity spread after 79 cycles of the applied field is more precise than the one measured after  $79\frac{1}{2}$  cycles. After 79 cycles the cloud expands rapidly along  $z$  and much more slowly along the  $\rho$  direction. Therefore, the signal integrated over  $z$  stays nearly constant. After  $79\frac{1}{2}$  cycles the cloud expands rapidly along  $\rho$  and much more slowly along the  $z$  direction. The signal integrated over  $z$ , therefore, drops



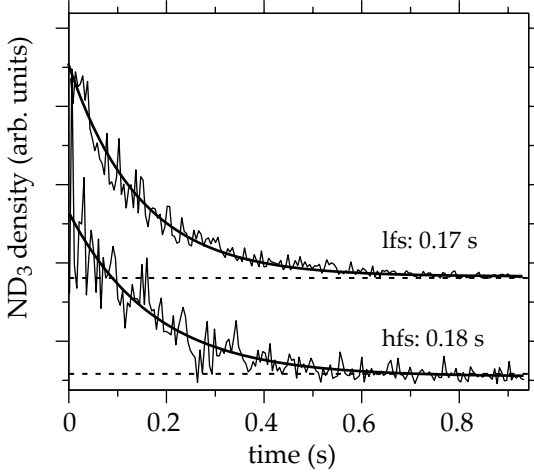


Figure 5.13: Density of  $^{15}\text{ND}_3$  molecules in low-field-seeking (upper curve) and high-field-seeking states (lower curve) at the center of the trap as a function of time. The bold lines show an exponential fit to the data with  $1/e=0.17$  s (low-field seekers) and  $1/e=0.18$  s (high-field seekers).

rather quickly.

Figure 5.13 shows the density at the center of the trap as a function of time for molecules in low-field-seeking (upper curve) and high-field-seeking states (lower curve). The bold lines through the data show an exponential fit. Molecules are seen to escape the trap with a  $1/e$  time of 0.17 s for low-field seekers and 0.18 s for high-field seekers. Within the error bars these lifetimes are equal to one another and to the 0.17 s found in earlier experiments performed in the same setup on molecules in low-field-seeking states trapped in a static trap (see figure 4.9 on page 77). We therefore conclude that the dominant loss channel is due to collisions with background atoms in the relatively poor ( $P = 5 \times 10^{-8}$  torr) vacuum.

At early times immediately after the trap is switched on, the density at the center of the trap shows some slight oscillations. These are mainly due to molecules that do not remain trapped. In order to measure the trap-frequency of the molecules directly, we have tried to make these oscillations more pronounced by deliberately switching the trap on too early, or by switching the trap off temporarily after having been on for 80 ms. Although these attempts were unsuccessful, we were able to verify that the trap frequency of the molecules along  $z$ ,  $\omega_{\text{secular},z}/2\pi$  is equal to about 240 Hz when we apply a frequency  $\Omega_{\text{driven}}/2\pi = 1100$  Hz with a duty cycle of 45% as expected from our simulations.

In all experiments discussed so far, we switch instantaneously (within 200 ns)

between the two different trap configurations. Under some conditions the trap will still be stable if we leave it off for a certain time before switching to the next configuration. During this time the motion of the molecules is  $x(t) = x(t_0) + v_x(t_0)(t - t_0)$ , with  $x(t_0)$  and  $v_x(t_0)$  the initial position and velocity of the molecule, respectively. So the transfer matrix is simply:

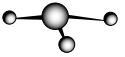
$$M(t|t_0) = \begin{pmatrix} 1 & t - t_0 \\ 0 & 1 \end{pmatrix} \quad O: \text{ free flight} \quad (5.24)$$

The transfer matrix during free flight is written as  $O$ . The transfer matrix for a single cycle now becomes  $F(T_{\text{on}} + T_{\text{off}}|\frac{1}{2}T_{\text{on}} + T_{\text{off}}) \cdot O(\frac{1}{2}T_{\text{on}} + T_{\text{off}}|\frac{1}{2}T_{\text{on}} + \frac{1}{2}T_{\text{off}}) \cdot D(\frac{1}{2}T_{\text{on}} + \frac{1}{2}T_{\text{off}}|\frac{1}{2}T_{\text{off}}) \cdot O(\frac{1}{2}T_{\text{off}}|0)$ . The stability for this arrangement can be determined as before. Figure 3 of reference [108] shows the stability diagram for an alternate gradient decelerator. This can be translated to our situation by simply replacing  $\kappa L$  and  $\kappa S$  by  $\Omega_{\text{hex}}T_{\text{on}}$  and  $\Omega_{\text{hex}}T_{\text{off}}$ , respectively.

Figure 5.14 shows the density at the center of the trap as a function of  $T_{\text{on}}$  for a number of different values of  $T_{\text{off}}$ . The measurements on the left are for molecules in low-field-seeking states, the measurements on the right for molecules in high-field-seeking states. As before, the duty cycle is adjusted such that the phase advance along  $z$  is equal to the phase advance along  $\rho$ . The measurements taken with  $T_{\text{off}} = 0$  are identical to those shown in figure 5.7 but now plotted as a function of  $2\pi/\Omega_{\text{driven}}$ . When  $T_{\text{off}}$  is increased, the maximum of the curves shifts to smaller values of  $T_{\text{on}}$ . Interestingly, the maximum density drops only slightly for higher values of  $T_{\text{off}}$ . When the fields are switched off for 500  $\mu\text{s}$ , the maximum density is obtained for  $T_{\text{on}} = 500 \mu\text{s}$ , i.e., the fields are applied only half of the time. With these settings, the density at the center of the trap is decreased by less than 20% compared to the situation in which the fields are applied all the time.

## 5.7 Summary and Conclusions

In this chapter, we have experimentally demonstrated trapping of molecules in both high-field-seeking and low-field-seeking states in a cylindrically symmetric electric AC trap. We have measured the spatial profile of the trapped cloud immediately after release and after a variable expansion time. We have compared these measurements to a simple linear model and to numerical simulations taking into account the true force on the molecules. By changing the duty cycle of the square wave voltage that is applied to the trap, the trapping frequencies along  $z$  and  $\rho$  can be chosen to be the same. At 1100 Hz and with a duty cycle of 45%, the trapping frequency is around 240 Hz. With these settings we find the full width at half maximum (FWHM) to be  $\Delta z = 1.3 \text{ mm}$ ,  $\Delta v_z = 1.3 \text{ m/s}$  ( $T=0.8 \text{ mK}$ ) and  $\Delta z = 0.63 \text{ mm}$ ,  $\Delta v_z = 1.8 \text{ m/s}$  ( $T=1.5 \text{ mK}$ ) when the fields are focusing along  $z$  and  $\rho$ , respectively. From numerical simulations, we find the phase-space volume that can be confined by the trap (the acceptance) to



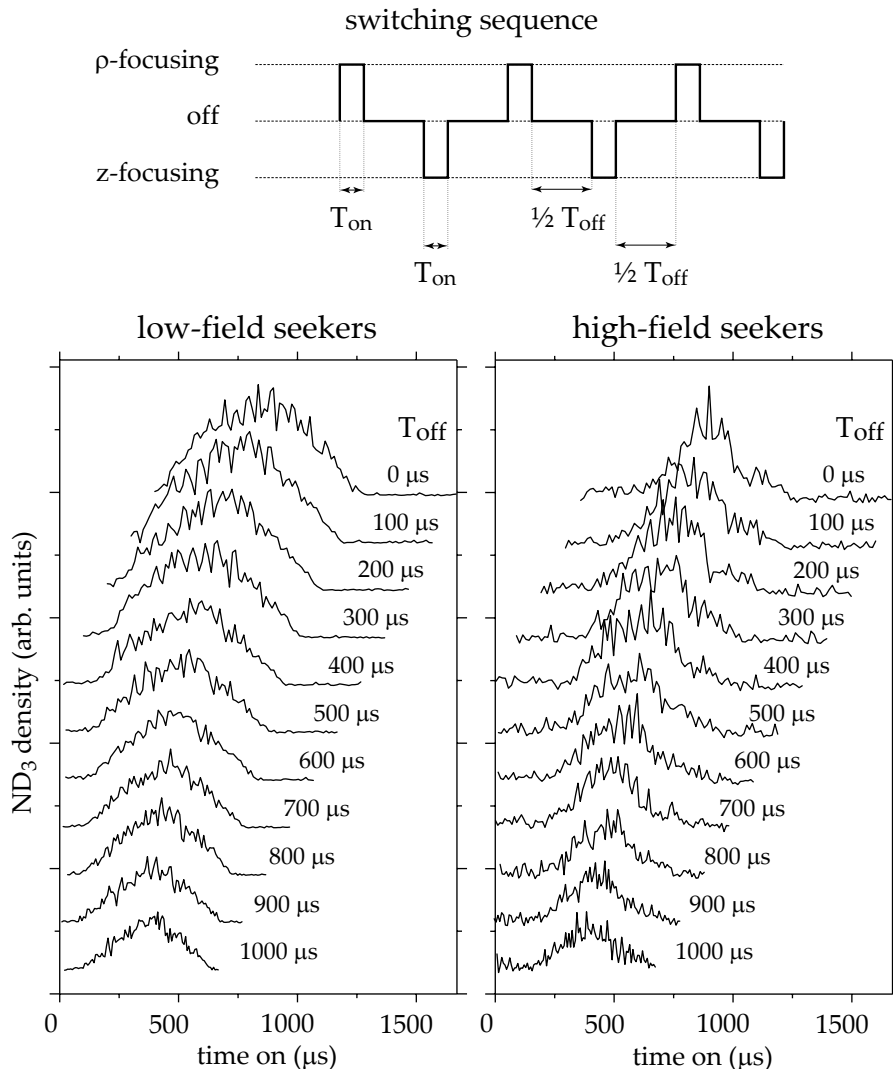


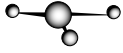
Figure 5.14: Density of  $^{15}\text{ND}_3$  molecules at the center of the trap as a function of the time that the focusing and defocusing fields are on for a number of different values for which the fields are off.

be  $270 \text{ mm}^3 \cdot (\text{m/s})^3$ , corresponding to a trap depth of about 5 mK and a trap volume of about  $20 \text{ mm}^2$ . The phase-space volume (the emittance) of the Stark decelerated molecular beam used to load the trap is about 5 times larger than the acceptance of the trap [148]. Therefore, we expect to homogeneously fill the acceptance of the trap, which is consistent with our measurements.

We find – both from simulation and from measurements – that the acceptance is limited by the non-linearities of the forces. Due to these non-linearities the maximum position spread of the packet scales as  $1/\Omega_{\text{driven}}^3$ , and consequently, the acceptance scales as  $1/\Omega_{\text{driven}}^9$  rather than the expected  $1/\Omega_{\text{driven}}^3$  if the forces would be perfectly linear. This has important consequences for the possibility of using evaporative – and to a lesser extent – sympathetic cooling in AC traps. When collisions between trapped molecules occur, energy that is stored in the micro motion can be transferred into secular motion. This process is called ‘viscous’ heating. Viscous heating competes with the ‘good’ consequences of collisions – thermalization and evaporation of the hottest molecules over the trap barrier leading to cooling. As the amount of viscous heating scales as  $(\omega_{\text{secular}}/\Omega_{\text{driven}})^2$ , evaporative cooling is more likely to work at higher frequencies [110, 172].

In minimizing non-linearities, we are constrained by the need to reverse the focusing and defocusing directions by adjusting the voltages only. When the shape of the electrodes is modified to improve the linearity of the focusing force in one configuration, the linearity of the other configuration is deteriorated. It was argued in section 5.4 that the cylindrical hexapole geometry used in our experiments has in fact the optimal shape. Other possible electrode geometries suffer from the same problem. Using the experimentally validated program used for the cylindrical trap, we have also calculated the acceptance for the linear and three-phase AC trap presented in section 5.3 and found them to be comparable.

Besides the acceptance and strength of confinement, there are other important criteria to choose a specific AC trap. The main advantage of the cylindrical trap over the other two traps is that at the center the electric field has a (controllable) constant direction and magnitude. This may be important for collision studies and experiments aimed at detecting the permanent electric dipole moment of the electron. Moreover, this may be needed for avoiding Majorana transitions induced by the varying electric field. As demonstrated in this chapter, the electric fields of the trap can also be switched off repeatedly – or switched to a variable homogeneous electric field – for as long as half a millisecond without significantly decreasing the trap depth. The cylindrical and three-phase trap can be used for AC trapping of molecules in both high-field-seeking and low-field-seeking states. Furthermore, by applying the appropriate voltages, the cylindrically symmetric trap can be used for trapping molecules in low-field-seeking states in a static quadrupole or hexapole potential (see chapter 4), and the three-phase trap can be used for trapping of molecules in low-field-seeking states in a Ioffe-Pritchard trap [64, 65]. The

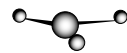


main advantages of the linear and, to a lesser extent, the three-phase trap are that they are conveniently loaded from a Stark decelerator [117], and are very accessible for laser beams to detect and manipulate the trapped molecules.

It is useful to compare the AC traps with other traps for neutral molecules that have been demonstrated. Traps using inhomogeneous static electric and magnetic fields are easily 1 K deep and typically have a trap volume of 1 cm<sup>3</sup> [52, 56, 57, 173]. These traps can only be used to trap molecules in low-field-seeking states. Although it is impossible to create a field maximum using static electric or magnetic fields, this does not apply to optical [95] or microwave fields [100]. Molecules in high-field-seeking states have been trapped in the focus of a CO<sub>2</sub> laser beam [97]. The light traps thus far demonstrated typically have a trap depth of a few hundred  $\mu$ K and a volume of 10<sup>-5</sup> cm<sup>3</sup>. Our AC electric trap demonstrated here can be used to trap molecules in both low-field and high-field-seeking states and has a trap depth of about 5 mK and a trap volume of about 20 mm<sup>3</sup>.

# Bibliography

- [1] *Merriam Webster Online dictionary*.
- [2] M. Niering, R. Holzwarth, J. Reichert, P. Pokasov, T. Udem, M. Weitz, T.W. Hänsch, P. Lemonde, G. Santarelli, M. Abgrall, P. Laurent, C. Salomon and A. Clairon, *Phys. Rev. Lett.* **84**, 5496 (2000).
- [3] T. Udem, A. Huber, B. Gross, J. Reichert, M. Prevedelli, M. Weitz and T.W. Hänsch, *Phys. Rev. Lett.* **79**, 2646 (1997).
- [4] B. de Beauvoir, F. Nez, L. Julien, B. Cagnac, F. Biraben, D. Touahri, L. Hilico, O. Acef, A. Clairon and J.J. Zondy, *Phys. Rev. Lett.* **78**, 440 (1997).
- [5] C. Schwob, L. Jozefowski, B. de Beauvoir, L. Hilico, E. Nez, L. Julien, F. Biraben, O. Acef, J.J. Zondy and A. Clairon, *Phys. Rev. Lett.* **86**, 4193 (2001).
- [6] J.J. Hudson, B.E. Sauer, M.R. Tarbutt and E.A. Hinds, *Phys. Rev. Lett.* **89**, 023003 (2002).
- [7] D. Kawall, F. Bay, S. Bickman, Y. Jiang and D. DeMille, *Phys. Rev. Lett.* **92**, 133007 (2004).
- [8] E. Arimondo, P. Glorieux and T. Oka, *Opt. Comm.* **23**, 369 (1977).
- [9] J. Crassous, F. Monier, J.P. Dutasta, M. Ziskind, C. Daussy, C. Grain and C. Chardonnet, *Chem. Phys. Chem.* **4**, 541 (2003).
- [10] M. Quack, *Angew. Chem. Int. Ed.* **41**, 4618 (2002).
- [11] W.A. Bonner, *Chirality* **12**, 114 (2000).
- [12] S.G. Karshenboim, *Can. J. Phys.* **78**, 639 (2000).
- [13] J.P. Uzan, *Rev. Mod. Phys.* **75**, 403 (2003).

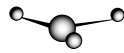


## Bibliography

---

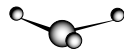
- [14] J.K. Webb, M.T. Murphy, V.V. Flambaum, V.A. Dzuba, J.D. Barrow, C.W. Churchill, J.X. Prochaska and A.M. Wolfe, *Phys. Rev. Lett.* **87**, 91301 (2001).
- [15] L.L. Cowie and A. Songaila, *Nature* **428**, 132 (2004).
- [16] R. Srianand, H. Chand, P. Petitjean and B. Aracil, *Phys. Rev. Lett.* **92**, 121302 (2004).
- [17] E.R. Hudson, H.J. Lewandowski, B.C. Sawyer and J. Ye, *Phys. Rev. Lett.* **96**, 143004 (2006).
- [18] R.I. Thompson, *Astrophys. Lett. & Comm.* **16**, 3 (1975).
- [19] W. Ubachs and E. Reinhold, *Phys. Rev. Lett.* **92**, 101302 (2004).
- [20] E. Reinhold, R. Buning, U. Hollenstein, A. Ivanchik, P. Petitjean and W. Ubachs, *Phys. Rev. Lett.* **96**, 151101 (2006).
- [21] A. Ivanchik, P. Petitjean, D. Varshalovich, B. Aracil, R. Srianand, H. Chand, C. Ledoux and P. Boisseé, *Astron. Astrophys.* **440**, 45 (2005).
- [22] P. Helminger, F.C. De Lucia, W. Gordy, H.W. Morgan and P.A. Staats, *Phys. Rev. A* **9**, 12 (1974).
- [23] C.H. Townes and A.L. Schawlow: *Microwave Spectroscopy*. Dover Publications, New York, 1975.
- [24] S.G. Kukolich, *Phys. Rev.* **156**, 83 (1967).
- [25] V.V. Flambaum, D.B. Leinweber, A.W. Thomas and R.D. Young, 2004. V.V. Flambaum, private communication.
- [26] N. Balakrishnan and A. Dalgarno, *J. Chem. Phys.* **113**, 621 (2000).
- [27] N. Balakrishnan and A. Dalgarno, *Chem. Phys. Lett.* **341**, 652 (2001).
- [28] T. Kraemer, M. Mark, P. Waldburger, J.G. Danzl, C. Chin, B. Engeser, A.D. Lange, K. Pilch, A. Jaakkola, H.C. Nägerl and R. Grimm, *Nature* **440**, 315 (2006).
- [29] C. Day, *Physics Today* **4**, 18 (2006).
- [30] C. Chin, T. Kraemer, M. Mark, J. Herbig, P. Waldburger, H.C. Nägerl and R. Grimm, *Phys. Rev. Lett.* **94**, 123201 (2005).
- [31] J.L. Bohn, *Phys. Rev. A* **63**, 052714 (2001).
- [32] R.V. Krems and A. Dalgarno, *J. Chem. Phys.* **120**, 2296 (2004).
- [33] J.M. Doyle. *private communication*, 2006.

- [34] M.H. Anderson, J.R. Ensher, M.R. Matthews, C.E. Wieman and E.A. Cornell, *Science* **269**, 198 (1995).
- [35] K.B. Davis, M.O. Mewes, M.R. Andrews, N.J. van Druten, D.S. Durfee, D.M. Kurn and W. Ketterle, *Phys. Rev. Lett.* **75**, 3969 (1995).
- [36] C.C. Bradley, C.A. Sackett and R.G. Hulet, *Phys. Rev. Lett.* **78**, 985 (1997).
- [37] S. Jochim, M. Bartenstein, A. Altmeyer, G. Hendl, S. Riedl, C. Chin, J. Hecker Denschlag and R. Grimm, *Science* **302**, 2101 (2003).
- [38] M. Greiner, C.A. Regal and D.S. Jin, *Nature* **426**, 537 (2003).
- [39] M.W. Zwierlein, C.A. Stan, C.H. Schunck, S.M.F. Raupach, S. Gupta, Z. Hadzibabic and W. Ketterle, *Phys. Rev. Lett.* **91**, 250401 (2003).
- [40] L. Santos, G.V. Shlyapnikov, P. Zoller and M. Lewenstein, *Phys. Rev. Lett.* **85**, 1791 (2000).
- [41] J. Stuhler, A. Griesmaier, T. Koch, M. Fattori, T. Pfau, S. Giovanazzi, P. Pedri and L. Santos, *Phys. Rev. Lett.* **95**, 150406 (2005).
- [42] V.V. Vladimirovskii, *Soviet Physics - JETP* **12**, 740 (1961).
- [43] C. Heer, *Rev. Sci. Instrum.* **34**, 532 (1963).
- [44] K.J. Kügler, W. Paul and U. Trinks, *Phys. Lett. B* **72**, 422 (1978).
- [45] D.E. Pritchard, *Phys. Rev. Lett.* **51**, 1336 (1983).
- [46] H. Metcalf, *Prog. Quant. Electr.* **8**, 169 (1984).
- [47] T. Bergeman, G. Erez and H.J. Metcalf, *Phys. Rev. A* **35**, 1535 (1987).
- [48] V.I. Balykin, V.G. Minogin and V.S. Letokhov, *Rep. Prog. Phys.* **63**, 1429 (2000).
- [49] J.G.E. Harris, R.A. Michniak, S.V. Nguyen, W.C. Campbell, D. Egorov, S.E. Maxwell, L.D. van Buuren and J.M. Doyle, *Rev. Sci. Instrum.* **75**, 17 (2004).
- [50] Y.V. Gott, M.S. Ioffe and V.G. Telkovsky, *Nuclear fusion Suppl.* **3**, 1045 (1962).
- [51] A.L. Migdall, J.V. Prodan, W.D. Phillips, T.H. Bergeman and H.J. Metcalf, *Phys. Rev. Lett.* **54**, 2596 (1985).
- [52] J.D. Weinstein, R. deCarvalho, T. Guillet, B. Friedrich and J.M. Doyle, *Nature* **395**, 148 (1998).



- [53] W.H. Wing, *Phys. Rev. Lett.* **45**, 631 (1980).
- [54] D.P. Katz, *J. Chem. Phys.* **107**, 8491 (1997).
- [55] H.L. Bethlem, G. Berden and G. Meijer, *Phys. Rev. Lett.* **83**, 1558 (1999).
- [56] H.L. Bethlem, G. Berden, F.M.H. Crompvoets, R.T. Jongma, A.J.A. van Roij and G. Meijer, *Nature* **406**, 491 (2000).
- [57] S.Y.T. van de Meerakker, P.H.M. Smeets, N. Vanhaecke, R.T. Jongma and G. Meijer, *Phys. Rev. Lett.* **94**, 023004 (2005).
- [58] F.M.H. Crompvoets, H.L. Bethlem, R.T. Jongma and G. Meijer, *Nature* **411**, 174 (2001).
- [59] F.M.H. Crompvoets, H.L. Bethlem, J. Küpper, A.J.A. van Roij and G. Meijer, *Phys. Rev. A* **69**, 063406 (2004).
- [60] S.Y.T. van de Meerakker, R.T. Jongma, H.L. Bethlem and G. Meijer, *Phys. Rev. A* **64**, 041401 (2001).
- [61] C.E. Heiner. *private communication*, 2006.
- [62] T. Rieger, T. Junglen, S.A. Rangwala, P.W.H. Pinkse and G. Rempe, *Phys. Rev. Lett.* **95**, 173002 (2005).
- [63] T. Junglen, T. Rieger, S.A. Rangwala, P.W.H. Pinkse and G. Rempe, *Phys. Rev. Lett.* **92**, 223001 (2004).
- [64] G. Xu: *Manipulation and Quantum Control of Ultracold Atoms and Molecules for Precision Measurements*. The University of Texas at Austin, Dissertation, 2001.
- [65] N.E. Shafer-Ray, K.A. Milton, B.R. Furneaux, E.R.I. Abraham and G.R. Kalbfleisch, *Phys. Rev. A* **67**, 045401 (2003).
- [66] A. André, D. DeMille, J.M. Doyle, M.D. Lukin, S.E. Maxwell, P. Rabl, R.J. Schoelkopf and P. Zoller, *Nature Physics* **2**, 636 (2006).
- [67] B.H. Bransden and C.J. Joachain: *Quantum Mechanics*. 1. edition. Addison Wesley Longman Limited, Harlow, England, 1989.
- [68] P.F. Bernath: *Spectra of atoms and molecules*. Oxford university press, New York, NY, USA, 1995.
- [69] L. Fusina and S.N. Murzin, *J. Mol. Spec.* **167**, 464 (1994).
- [70] B.E. Sauer, J. Wang and E.A. Hinds, *J. Chem. Phys.* **105**, 7412 (1996).
- [71] D.R. Borst, T.M. Korter and D.W. Pratt, *Chem. Phys. Lett.* **350**, 485 (2001).

- [72] M. Kajita, *Eur. Phys. J. D* **38**, 315 (2006).
- [73] T.R. Rizzo, Y.D. Park, L.A. Peteanu and D.H. Levy, *J. Chem. Phys.* **84**, 2534 (1986).
- [74] R. Weinkauf, J. Schermann, M.S. de Vries and K. Kleinermanns, *Eur. Phys. J. D* **20**, 309 (2002).
- [75] C.S. Wu, E. Ambler, R.W. Hayward, D.D. Hopps and R.P. Hudson, *Phys. Rev.* **105**, 1413 (1957).
- [76] L.I. Schiff, *Phys. Rev.* **132**, 2194 (1963).
- [77] P.G.H. Sandars, *Phys. Lett.* **14**, 194 (1965).
- [78] M.A. Bouchiat and C. Bouchiat, *Rep. Prog. Phys.* **60**, 1351 (1997).
- [79] C.S. Wood, S.C. Bennet, D. Cho, B.P. Masterson, J.L. Roberts, C.E. Tanner and C.E. Wieman, *Science* **275**, 1759 (1997).
- [80] M. Ziskind, C. Daussy, T. Marrel and C. Chardonnet, *Eur. Phys. J. D* **20**, 219 (2002).
- [81] R. Berger and M. Quack, *Chem. Phys. Chem.* **1**, 57 (2000).
- [82] J.K. Laerdahl, R. Wesendrup and P. Schwerdtfeger, *Chem. Phys. Chem.* **1**, 60 (2000).
- [83] R. Wesendrup, J.K. Laerdahl, R.N. Compton and P. Schwerdtfeger, *J. Phys. Chem. A* **107**, 6668 (2003).
- [84] S. Earnshaw, *Trans. Camb. Phil. Soc.* **7**, 97 (1842).
- [85] W. Jones, *Eur. J. Phys.* **1**, 85 (1980).
- [86] J.C. Helmer, F.B. Jacobus and P.A. Sturrock, *J. Appl. Phys.* **31**, 458 (1960).
- [87] K.R. Chien, P.B. Foreman, K.H. Castleton and S.G. Kukolich, *Chem. Phys.* **7**, 161 (1975).
- [88] S.K. Sekatskiĭ, *JETP Lett.* **62**, 916 (1995).
- [89] S.K. Sekatskiĭ and J. Schmiedmayer, *Europhys. Lett.* **36**, 407 (1996).
- [90] J. Schmiedmayer, *Appl. Phys. B* **60**, 169 (1995).
- [91] L.V. Hau, M.M. Burns and J.A. Golovchenko, *Phys. Rev. A* **45**, 6468 (1992).
- [92] J. Schmiedmayer, *Phys. Rev. A* **52**, R13 (1995).



- [93] H.J. Loesch and B. Scheel, *Phys. Rev. Lett.* **85**, 2709 (2000).
- [94] R.T. Jongma, G. von Helden, G. Berden and G. Meijer, *Chem. Phys. Lett.* **270**, 304 (1997).
- [95] R. Grimm, M. Weidemüller and Y. Ovchinnikov, *Adv. Atom. Mol. Opt. Phys.* **42**, 95 (1999).
- [96] S. Chu, J.E. Bjorkholm, A. Ashkin and A. Cable, *Phys. Rev. Lett.* **57**, 314 (1986).
- [97] T. Takekoshi, B.M. Patterson and R.J. Knize, *Phys. Rev. Lett.* **81**, 5105 (1998).
- [98] M. Schnell. *private communication*, 2006.
- [99] R.J.C. Spreeuw, C. Gerz, L.S. Goldner, W.D. Phillips, S.L. Rolston, C.I. Westbrook, M.W. Reynolds and I.F. Silvera, *Phys. Rev. Lett.* **72**, 3162 (1994).
- [100] D. DeMille, D.R. Glenn and J. Petricka, *Eur. Phys. J. D* **31**, 375 (2004).
- [101] E.D. Courant, M.S. Livingston and H.S. Snyder, *Ann. Phys.* **3**, 1 (1958).
- [102] E.D. Courant and H.S. Snyder, *Phys. Rev.* **88**, 1190 (1952).
- [103] D. Auerbach, E.E.A. Bromberg and L. Wharton, *J. Chem. Phys.* **45**, 2160 (1966).
- [104] D. Kakati and D.C. Lainé, *Phys. Lett. A* **24**, 676 (1967).
- [105] D. Kakati and D.C. Lainé, *J. Phys. E* **4**, 269 (1971).
- [106] H.L. Bethlem, A.J.A. van Roij, R.T. Jongma and G. Meijer, *Phys. Rev. Lett.* **88**, 133003 (2002).
- [107] M.R. Tarbutt, H.L. Bethlem, J.J. Hudson, V.L. Ryabov, V.A. Ryzhov, B.E. Sauer, G. Meijer and E.A. Hinds, *Phys. Rev. Lett.* **92**, 173002 (2004).
- [108] H.L. Bethlem, M.R. Tarbutt, J. Küpper, D. Carty, K. Wohlfart, E.A. Hinds and G. Meijer, *J. Phys. B* **39**, R263 (2006).
- [109] R.V.E. Lovelace, C. Mehanian, T.J. Tommila and D.M. Lee, *Nature* **318**, 30 (1985).
- [110] E.A. Cornell, C. Monroe and C.E. Wieman, *Phys. Rev. Lett.* **67**, 2439 (1991).
- [111] F. Shimizu and M. Morinaga, *Jpn. J. Appl. Phys.* **31**, L1721 (1992).

- [112] F. Shimizu: In *Atomic Physics 13*, ed. by H. Walther, T. Hänsch and B. Neizert, volume 275 of *AIP Conf. Proc.*. American Institute of Physics, New York, NY, USA (1993).
- [113] M. Morinaga and F. Shimizu, *Laser Phys.* **4**, 412 (1994).
- [114] E. Peik, *Eur. Phys. J. D* **6**, 179 (1999).
- [115] H. Katori and T. Akatsuka, *Jpn. J. Appl. Phys.* **43**, 358 (2004).
- [116] T. Kishimoto, H. Hachisu, J. Fujiki, K. Nagato, M. Yasuda and H. Katori, *Phys. Rev. Lett.* **96**, 123001 (2006).
- [117] M. Schnell et al., In preparation.
- [118] C.E. Cleeton and N.H. Williams, *Phys. Rev.* **45**, 234 (1934).
- [119] J.P. Gordon, H.J. Zeiger and C.H. Townes, *Phys. Rev.* **95**, 282 (1954).
- [120] J.P. Gordon, H.J. Zeiger and C.H. Townes, *Phys. Rev.* **99**, 1264 (1955).
- [121] A.C. Cheung, D.M. Rank, C.H. Townes, D.D. Thornton and W.J. Welch, *Phys. Rev. Lett.* **21**, 1701 (1968).
- [122] P.T.P. Ho and C.H. Townes, *Ann. Rev. Astron. Astrophys.* **21**, 239 (1983).
- [123] G.R. Gunther-Mohr, R.L. White, A.L. Schawlow, W.E. Good and D.K. Coles, *Phys. Rev.* **94**, 1184 (1954).
- [124] G.R. Gunther-Mohr, C.H. Townes and J.H. van Vleck, *Phys. Rev.* **94**, 1191 (1954).
- [125] J.P. Gordon, *Phys. Rev.* **99**, 1253 (1955).
- [126] G.F. Hadley, *J. Chem. Phys.* **26**, 1482 (1957).
- [127] G.F. Hadley, *Phys. Rev.* **108**, 291 (1957).
- [128] K. Shimoda and K. Kondo, *J. Phys. Soc. Jpn.* **15**, 1125 (1960).
- [129] K. Kondo and K. Shimoda, *J. Phys. Soc. Jpn.* **20**, 437 (1965).
- [130] R.G. Nuckolls, L.J. Rueger and H. Lyons, *Phys. Rev.* **89**, 1101 (1953).
- [131] G. Herrmann, *J. Chem. Phys.* **29**, 875 (1958).
- [132] S.N. Murzin and B.D. Osipov, *Opt. Spektrosk.* **52**, 146 (1982).
- [133] S.N. Murzin and B.D. Osipov, *Opt. Spektrosk.* **53**, 579 (1982).



- [134] S.N. Murzin, *Opt. Spektrosk.* **59**, 438 (1985).
- [135] L. Fusina, M. Carlotti, G. Dilonardo, S.N. Murzin and O.N. Stepanov, *J. Mol. Spec.* **147**, 71 (1991).
- [136] H. Howe: *Stripline circuit design*. Artech House, Inc., Norwood, MA, 1974.
- [137] M.N.R. Ashfold, R.N. Dixon, N. Little, R.J. Stickland and C.M. Western, *J. Chem. Phys.* **89**, 1754 (1988).
- [138] J. van Veldhoven, J. Küpper, H.L. Bethlem, B. Sartakov, A.J. van Roij and G. Meijer, *Eur. Phys. J. D* **31**, 337 (2004).
- [139] L.D. Landau and E.M. Lifshitz: *Quantum Mechanics – Nonrelativistic Theory*. 3. edition. Pergamon Press, Oxford, 1977. Translated from Russian by J.B. Sykes and J.S. Bell.
- [140] N.F. Ramsey, *Rev. Mod. Phys.* **62**, 541 (1990).
- [141] H. Katori, M. Takamoto, V.G. Pal'chikov and V.D. Ovsiannikov, *Phys. Rev. Lett.* **91**, 173005 (2003).
- [142] M.A. Kasevich, E. Riis, S. Chu and R.G. Devoe, *Phys. Rev. Lett.* **63**, 612 (1989).
- [143] C. Audoin and B. Guinot: *The Measurement of Time*. Oxford University Press, 2001.
- [144] P.E. Durand, G. Nogues, V. Bernard, A. Amy-Klein and C. Chardonnet, *Europhys. Lett.* **37**, 103 (1997).
- [145] A. Amy-Klein, L.F. Constantin, R.J. Butcher, C. Daussy, P.E. Durand, G. Nogues and C. Chardonnet, *Opt. Exp.* **4**, 67 (1999).
- [146] H.L. Bethlem and G. Meijer, *Int. Rev. Phys. Chem.* **22**, 73 (2003).
- [147] F.M.H. Crompvoets, R.T. Jongma, H.L. Bethlem, A.J.A. van Roij and G. Meijer, *Phys. Rev. Lett.* **89**, 093004 (2002).
- [148] H.L. Bethlem, F.M.H. Crompvoets, R.T. Jongma, S.Y.T. van de Meerakker and G. Meijer, *Phys. Rev. A* **65**, 053416 (2002).
- [149] W. Demtröder: *Laser Spectroscopy: Basic Concepts and Instrumentation*. 3. edition. Springer Verlag, Berlin, 2003.
- [150] J.W. Cederberg, *Am. J. Phys.* **40**, 159 (1972).
- [151] J.K.G. Watson, *J. Mol. Spec.* **66**, 500 (1977).

- [152] R.L. Bhattacharjee, L.H. Johnston, G.R. Sudhakaran and J.C. Sarker, *J. Mol. Spec.* **138**, 38 (1989).
- [153] M.R. Andrews, C.G. Townsend, H.J. Miesner, D.S. Durfee, D.M. Kurn and W. Ketterle, *Science* **275**, 637 (1997).
- [154] S. Inouye, S. Gupta, T. Rosenband, A.P. Chikkatur, A. Görlitz, T.L. Gustavson, A.E. Leanhardt, D.E. Pritchard and W. Ketterle, *Phys. Rev. Lett.* **87**, 080402 (2001).
- [155] M. Albiez, R. Gati, J. Fölling, S. Hunsmann, M. Cristiani and M.K. Oberthaler, *Phys. Rev. Lett.* **95**, 010402 (2005).
- [156] C. Buggle, J. Léonard, W. von Klitzing and J.T.M. Walraven, *Phys. Rev. Lett.* **93**, 173202 (2004).
- [157] D.A. Dahl: *Simion 3D Version 6.0*. Idaho National Engineering Laboratory, Idaho Falls (USA), 1995.
- [158] O.J. Luiten, M.W. Reynolds and J.T.M. Walraven, *Phys. Rev. A* **53**, 381 (1996).
- [159] F. Reif: *Fundamentals of statistical and thermal physics*. McGraw-Hill, Singapore, 1985.
- [160] B.G. Sartakov. *private communication*, 2006.
- [161] Special Issue “Ultracold Polar Molecules”, *Eur. Phys. J. D* **31** (2004).
- [162] W. Paul, *Rev. Mod. Phys.* **62**, 531 (1990).
- [163] H. Nishimura, G. Lambertson, J.G. Kalnins and H. Gould, *Eur. Phys. J. D* **31**, 359 (2004).
- [164] R.F. Wuerker, H.M. Goldenberg and R.V. Langmuir, *J. Appl. Phys.* **30**, 441 (1958).
- [165] M. Abramowitz and I.A. Stegun: *Handbook of Mathematical Functions*. 9. edition. Dover Publications, New York, NY, USA, 1970.
- [166] S.Y. Lee: *Accelerator physics*. 2. edition. World Scientific, Singapore, 2004.
- [167] G.B. Arfken and H.J. Weber: *Mathematical Methods for Physicists*. Academic Press, New York, 1995.
- [168] K. Gubbels, G. Meijer and B. Friedrich, *Phys. Rev. A* **73**, 063406 (2006).
- [169] H.G. Dehmelt, *Adv. Atom. Mol. Opt. Phys.* **3**, 53 .



## Bibliography

---

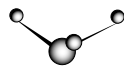
- [170] L.D. Landau and E.M. Lifshitz: *Mechanics*. 3. edition. Pergamon, Oxford, 1976.
- [171] P. Paasche, C. Angelescu, S. Ananthamurthy, D. Biswas, T. Valenzuela and G. Werth, *Eur. Phys. J. D* **22**, 183 (2003).
- [172] W. Petrich, M.H. Anderson, J.R. Ensher and E.A. Cornell, *Phys. Rev. Lett.* **74**, 3352 (1995).
- [173] N. Vanhaecke, W. de Souza Melo, B.L. Tolra, D. Comparat and P. Pillet, *Phys. Rev. Lett.* **89**, 063001 (2002).

# Hoofdstuk 6

## Samenvatting

Koude moleculen zijn cool. En wie kan het beter weten dan iemand die er 5 jaar lang onderzoek naar heeft gedaan? Toch vragen veel mensen zich af wat het nut van een dergelijk onderzoek eigenlijk is. Het is tenslotte fundamenteel onderzoek, bedoeld om de fundamenten van de wereld om ons heen beter te begrijpen zonder direct een duidelijke toepassing te leveren. Ja, wat is überhaupt het nut van fundamenteel onderzoek?

Dat ook mensen die het niet beoefenen wetenschap leuk vinden, blijkt uit de populariteit van populair-wetenschappelijke televisie programma's en tijdschriften. Echter, hoe toegepaster het onderzoek, hoe makkelijker het is zich een voorstelling te maken van het onderzoek zelf en ook van de impact die het zal hebben op de maatschappij. Fundamenteel onderzoek klinkt vaak erg abstract, een hobby voor een stel vakidioten. Maar bij een nadere beschouwing blijkt dat aan elk toegepast onderzoek fundamenteel onderzoek ten grondslag ligt. Om de wereld om ons heen beter te begrijpen, is het niet alleen nodig te begrijpen hoe dingen werken, maar ook waarom ze werken. Als we ons begrip van de onderliggende principes van een proces kunnen vergroten, blijkt vaak dat die op ver uiteenlopende situaties van toepassing zijn. En wie kan zeggen welk kleine stukje fundamentele kennis uiteindelijk tot een doorbraak op een ander gebied zal leiden, dat wel direct toepasbaar is in de maatschappij? Wil ik bijvoorbeeld beter begrijpen hoe het menselijk lichaam in elkaar zit, en daarom alle grote biomoleculen en hun interacties met elkaar bestuderen, is het vrijwel onmogelijk dat te doen zonder een fundamentele kennis van hoe moleculen in het algemeen in elkaar zitten. En dus bestuderen we ook kleinere moleculen en ontwikkelen we technieken om ze beter te kunnen onderzoeken. En dit doen we niet altijd met zo'n duidelijk beeld voor ogen als het begrijpen van biomoleculen. Hadden de wetenschappers van 100 jaar geleden dromen over macromoleculen en het begrijpen van biologische processen in het lichaam? Ik weet het niet. Toch heeft de kennis die zij toen hebben vergaard bijgedragen aan het begrip dat we nu van biomoleculen hebben. Net als de wetenschappers

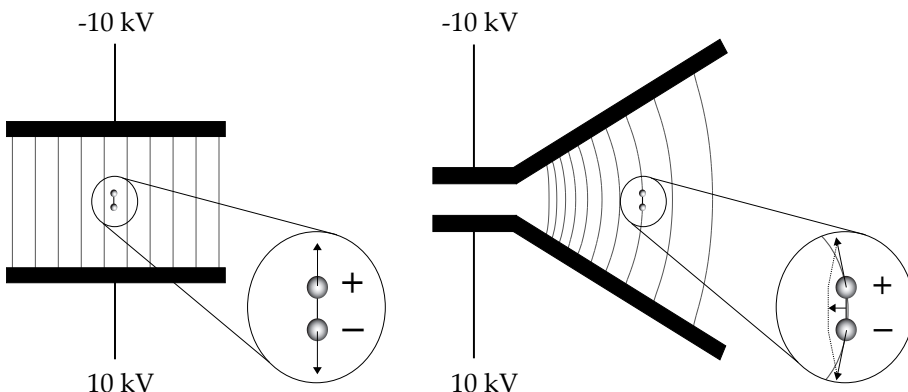


nu zijn ze aan een reis begonnen met open doel, een reis door een doolhof waar elke nieuwe afslag tot een hoogtepunt kan leiden waarvan we van tevoren het bestaan niet hadden kunnen vermoeden. En niemand weet waar we uitkomen als we nog 10 afslagen verder zijn...

Onderweg blijkt vaak dat niet alleen dat onbekende eindpunt belangrijk is, maar ook de reis zelf. Want terwijl wij technieken ontwikkelen om onze kennis te vergroten, blijken het soms die technieken te zijn die breder toepasbaar zijn dan iemand van tevoren had kunnen bedenken. Neem bijvoorbeeld de laser. Wie zou kunnen ontkennen dat de laser breed toepasbaar is, met een impact op de maatschappij die de wereld er hier en daar anders heeft doen uitzien? De laser wordt niet alleen gebruikt in de industrie, maar ook in de medische wereld heeft hij grote veranderingen teweeg gebracht. Toch is de laser een direct resultaat van fundamenteel onderzoek. Ten tijde van zijn ontdekking had niemand kunnen vermoeden hoe wijd verbreid de laser ooit eens gebruikt zou worden. De toenmalige onderzoekers wisten niet beter dan dat dit een interessant fysisch proces was. Leuk, nieuw, misschien toepasbaar voor verder fundamenteel onderzoek, maar aanvankelijk wist niemand of het enig maatschappelijk nut zou hebben. En als zij het al niet wisten, dan wisten hun voorgangers, de ontdekkers van de maser, het al helemaal niet. Welke fundamentele kennis lag hier nog meer aan ten grondslag, die onontbeerlijk was om op het punt in de reis aan te komen waar we nu zijn? Waarschijnlijk meer dan we zouden denken. Reden te over dus om onze weg op het pad van de fundamentele wetenschap te vervolgen, niet wetende waar we uit zullen komen, maar in de zekerheid dat de reis ons langs een paar interessante plekken zal voeren...

### 6.1 Temperatuur

Het kleine hoekje van de fundamentele natuurkunde dat ik de afgelopen jaren heb onderzocht maakt gebruik van koude moleculen. Maar wat is koud precies? Temperatuur heeft te maken met de snelheid van de moleculen in de lucht. Hoe warmer het is, hoe sneller de moleculen gemiddeld bewegen. Als we het dus hebben over koude moleculen, bedoelen we eigenlijk langzame moleculen. Natuurlijk bewegen de moleculen in de lucht niet allemaal even snel en niet allemaal dezelfde kant op. Als dat laatste wel het geval zou zijn, zouden we nooit een windstille dag kennen! Maar omdat er evenveel moleculen aan de voorkant tegen ons aan botsen als aan de achterkant, worden we niet omgeblazen. Bij kamertemperatuur ( $20^{\circ}\text{C}$ ) is de meest waarschijnlijke snelheid van stikstof moleculen in de lucht ongeveer 590 m/s, wat gelijk is aan 2100 km/uur. Zelfs op een koude dag in Moskou, laten we zeggen bij  $-40^{\circ}\text{C}$ , is de meest waarschijnlijke snelheid nog 530 m/s ( $\sim 1900$  km/uur). Zulke hoge snelheden maken het natuurlijk moeilijk deze moleculen te bestuderen. Daarom willen we ze graag afremmen, wat dus hetzelfde is als ze afkoelen. De techniek die hiervoor bij



Figuur 6.1: Aan de linkerkant is een dipolaire molecuul in een homogeen elektrisch veld te zien. De twee krachten op het molecuul heffen elkaar op en netto is er geen kracht. Aan de rechterkant bevindt het dipolaire molecuul zich in een inhomogeen veld. De twee krachten heffen elkaar nu niet op en netto is er een kracht in de richting van het hoogste elektrische veld.

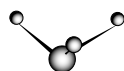
ons in het lab<sup>1</sup> ontwikkeld is, maakt gebruik van een Stark afremmer.

## 6.2 Stark afremmer

Om moleculen af te kunnen remmen, hebben we een kracht nodig. Door deze kracht zal de snelheid van het molecuul veranderen. Als een molecuul bijvoorbeeld naar links vliegt en de kracht is ook naar links, dan versnelt het molecuul. Is de kracht naar rechts, dan remt het molecuul af. Als de kracht uit een andere richting komt, zoals bijvoorbeeld van onderen of van boven, dan verandert niet alleen de grootte van de snelheid, maar ook de richting.

In de Stark afremmer wordt de zogeheten Stark kracht gebruikt. Deze kracht werkt op dipolaire moleculen. Dit wil zeggen dat de moleculen een kleine ladingsverdeling hebben, alhoewel ze in hun geheel neutraal zijn. De ene kant van het molecuul is dus een beetje positief, terwijl de andere kant van het molecuul evenveel negatief is. Als dit molecuul nu in een elektrisch veld komt, wordt er op beide kanten van het molecuul een kracht uitgeoefend, bijvoorbeeld op het positieve deel een kracht naar boven en op het negatieve deel een kracht naar beneden (zie de linkerkant van figuur 6.1). Als het elektrische veld overal even groot is en overall dezelfde richting heeft (een homogeen veld), dan zijn

<sup>1</sup>Het lab waarin deze techniek ontwikkeld is bevindt zich in Nijmegen aan de Radboud universiteit. Sindsdien hebben de Stark afremmers kort verwijld in Nieuwegein, in het FOM-Instituut voor Plasmafysica ‘Rijnhuizen’, waarna ze, hopelijk voor langere tijd, verhuisd zijn naar Berlijn, naar het Fritz-Haber-Institut.

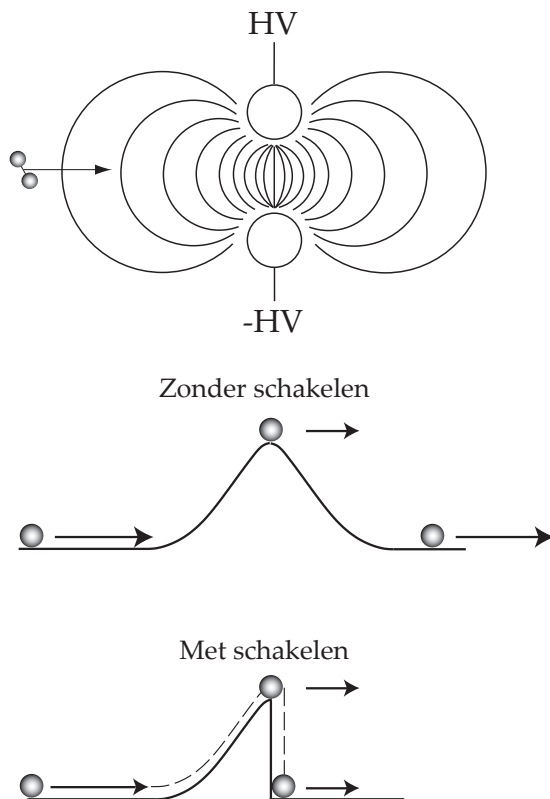


beide krachten even groot en heffen elkaar dus op. Er is geen netto kracht aanwezig en het molecuul zal dan ook niet van snelheid veranderen. Anders wordt het als het elektrische veld niet overal even groot is of als het van richting verandert, een zogenaamd inhomogeen veld. Nu zijn de twee krachten verschillend en heffen elkaar niet op. We houden een zeer kleine kracht over, die ervoor zorgt dat het molecuul een bepaalde kant op gedruwd wordt. Welke kant hangt af van de oriëntatie van het molecuul in het veld. Een voorbeeld is te zien aan de rechterkant van figuur 6.1. Het veld dat gemaakt wordt door de twee schuine platen wordt naar links toe steeds groter (de veldlijnen staan dichter bij elkaar). Ook is te zien dat het veld niet overal dezelfde richting heeft (de veldlijnen staan krom). De kracht die dit veld veroorzaakt op het positieve deel van het molecuul wijst naar linksboven. De kracht op het negatieve deel wijst naar linksonder. Als de twee krachten opgeteld worden, houd je een kracht naar links over, dus in de richting van het grotere elektrische veld. Daarom noemen we zo'n molecuul een hogeveldzoeker. Als het molecuul omgedraaid zou zijn, zou de kracht precies de andere kant op wijzen, in de richting van het kleinste veld. Zo'n molecuul noemen we een laagveldzoeker.

Volgens de klassieke natuurkunde kan het molecuul ook elke oriëntatie hebben tussen de twee die we net besproken hebben. Volgens de quantummechanica echter, zijn er maar een paar discrete oriëntaties mogelijk.

De afremmer is gebouwd voor laagveldzoekende moleculen. Het inhomogene veld maken we door een spanning aan te leggen op twee parallelle staafjes, zoals te zien is in figuur 6.2. Het veld is het hoogst tussen de staafjes en wordt kleiner als je verder weg gaat. Een laagveldzoekend molecuul dat richting de twee staafjes vliegt zal dus een kracht voelen die van de staafjes afwijst, in de richting van het laagste elektrische veld. Dit is te vergelijken met een knikker die tegen een berg oprolt. Net als de knikker, zal ook het molecuul afremmen als het tegen de berg opvliegt. Als het echter snel genoeg gaat om bovenaan de berg te komen, rolt het molecuul aan de andere kant weer naar beneden en onderaan de berg zal het molecuul net zo snel gaan als voordat het de berg opliep (zie het middelste plaatje in figuur 6.2). Om dit te voorkomen schakelen we voordat het molecuul de top bereikt snel de spanning uit en trekken zo als het ware de berg onder het molecuul vandaan. Op die manier kan het molecuul niet meer versnellen en blijft afgereemd, zoals ook te zien is onderaan in figuur 6.2.

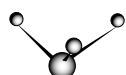
De afremmer werkt natuurlijk niet als de moleculen niet naar de afremmer toevliegen. De moleculen in de lucht vliegen alle kanten uit, dus die kunnen we niet gebruiken. Daarom nemen we als eerste een metalen kamer waar we de lucht uit pompen. Dit wordt een vacuum genoemd. In het vacuum bouwen we een kleinere kamer met gas, waarin een klein gaatje zit. Iedere keer dat we het gaatje openen, spuit er een straaltje moleculen uit, dat richting onze afremmer vliegt. De laagste snelheid die we met normale technieken kunnen bereiken is ongeveer 280 m/s ( $\sim 1000$  km/uur). Dat is zo snel dat één keer door een stel afremmer staafjes vliegen nog weinig effect heeft. Als we de

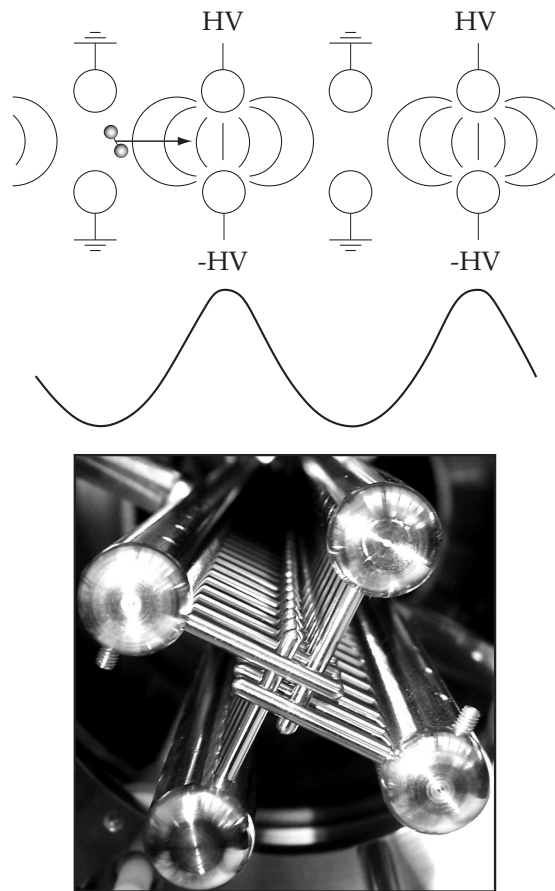


Figuur 6.2: Een set afremmerstaafjes. Door het spanningsverschil tussen de staafjes is er een elektrisch veld dat het hoogst is tussen de staafjes en lager verder weg. Voor de moleculen ziet het eruit als een berg. De snelheid van de moleculen wordt aangegeven door de lengte van de pijltjes.

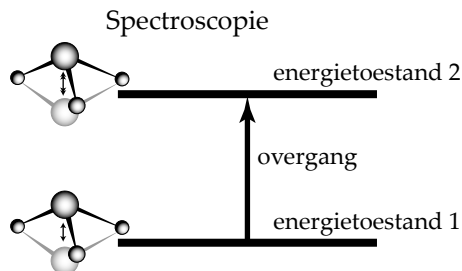
moleculen merkbaar af willen remmen, of zelfs tot stilstand willen brengen, moeten we het proces een paar keer herhalen. Daarom ziet de afremmer eruit als in figuur 6.3, met meerdere afremmer staafjes achter elkaar. De afremmer die ik heb gebruikt staat afgebeeld op de foto in figuur 6.3. In totaal zijn er 95 sets van staafjes, die bij elkaar worden gehouden door de grotere staven die de foto inlopen. Deze staven zorgen ook voor de elektrische verbinding: de oneven staafjes zijn verbonden met de grote staven linksboven en rechtsonder, terwijl de even staafjes verbonden zijn met de grote staven rechtsboven en linksonder. Hierdoor is elke set van afremmerstaafjes  $90^\circ$  gedraaid ten opzichte van zijn voorganger.

Op elk van de grotere staven kan een spanning van 10.000 V gezet worden. We sluiten de spanning nu eerst aan op de eerste afremmerset (en daarmee





Figuur 6.3: Een schematische voorstelling van de afremmer. Onder is een foto van de afremmer te zien.



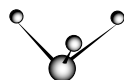
Figuur 6.4: Een overgang tussen twee energietoestanden. Het molecuul vibreert meer in het hogere energieniveau.

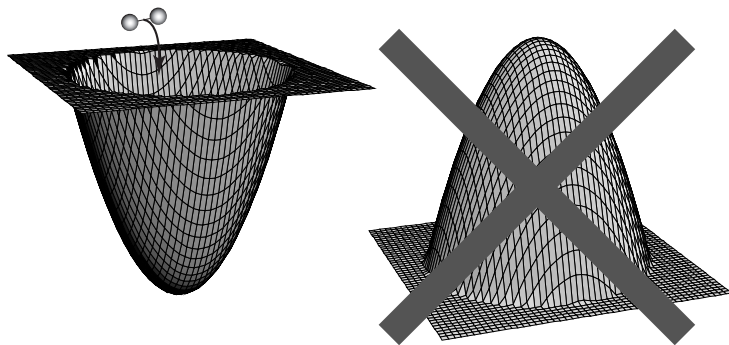
ook op alle oneven sets). Als de moleculen zijn afgeremd, schakelen we de spanning snel uit en tegelijkertijd schakelen we de tweede set aan (en daarmee ook alle even sets). Dit proces herhalen we tot de moleculen aan het eind van de afremmer zijn. Elke keer dat één set van paaltjes uitgeschakeld wordt, wordt de volgende aangeschakeld. Deze hele schakelreeks wordt door een computer aangestuurd. Door de verschillende settings te veranderen, kunnen we de eindsnelheid van de moleculen net zo kiezen als we zelf willen.

## 6.3 Spectroscopie

Moleculen kunnen beter bestudeerd worden als ze langzaam zijn. Eén manier om dat te doen is door middel van spectroscopie. In de spectroscopie wordt bestudeerd welke kleuren licht door een molecuul geabsorbeerd worden. Dit werkt op de volgende manier.

Omdat moleculen uit meerdere atomen bestaan, zijn er allerlei soorten van vibraties mogelijk binnen het molecuul. Klassiek gezien zou je denken dat elke vibratie willekeurig snel kan zijn. Kwantummechanisch gezien blijkt dat er slechts enkele discrete vibratiesnelheden mogelijk zijn. Bij elke hoeveelheid vibratie hoort een bepaalde hoeveelheid energie die ook discreet is en hoger wordt naarmate het molecuul harder vibreert. Daarom worden alle vibratietoestanden waarin het molecuul kan verkeren energietoestanden genoemd. Als het molecuul van de ene naar de andere energietoestand gaat, dus als het meer of minder gaan vibreren, wordt dat een overgang genoemd (zie figuur 6.4). Zo'n overgang kan veroorzaakt worden door het molecuul een hoeveelheid energie aan te bieden die precies gelijk is aan het energieverlies tussen zijn begin- en eindtoestand. Dit kan bijvoorbeeld gedaan worden met een laser. De hoeveelheid energie van de laser hangt af van zijn frequentie, ofwel van zijn kleur. Als de laser precies de juiste kleur heeft, dus precies de juiste hoeveelheid energie heeft, dan wordt het licht door het molecuul geabsorbeerd en gaat het molecuul harder vibreren. Als nu de structuur van het molecuul anders is, zal het





Figuur 6.5: Links een val voor laagveldzoekende moleculen. Rechts het equivalent voor hoogveldzoekende moleculen, dat niet gemaakt kan worden.

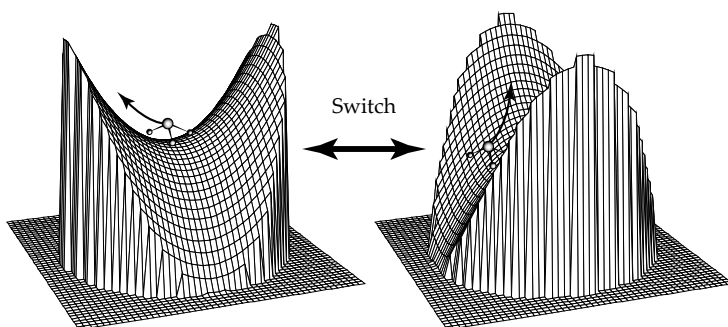
natuurlijk ook anders vibreren en dus andere kleuren licht absorberen. Als we dat dus kunnen meten, kunnen we met behulp daarvan de structuur van het molecuul uitleggen.

Spectroscopie kun je zowel aan koude als aan warme moleculen doen. Het nadeel van warme moleculen is alleen dat de kleur niet zo precies bepaald kan worden, en dat de structuur van het molecuul dus ook niet zo goed uitgerekend kan worden. Daarom is het beter om dit met koude moleculen te doen.

## 6.4 Een val

Om nog een stapje verder te gaan met het hele afremproces, zouden we de moleculen zo langzaam willen maken dat we ze op kunnen sluiten in een val. Het opluiten van laagveldzoekende moleculen is relatief eenvoudig. Wat je nodig hebt is een veld dat klein is in het midden en in alle richtingen groter wordt als je verder van het midden weg gaat. Als het molecuul langzaam genoeg gaat, valt het in deze val als een knikker in een knikkerpotje (zie de linkerkant van figuur 6.5).

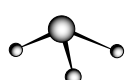
Lastiger wordt het als je hoogveldzoekende moleculen wilt opluiten. Toch is het belangrijk ook deze moleculen beter te bestuderen, omdat in veel gevallen hoogveldzoekende moleculen interessanter zijn dan laagveldzoekende. Eén reden daarvoor is bijvoorbeeld dat als het molecuul de laagst mogelijke hoeveelheid energie heeft, het altijd hoogveldzoekend is. Het is dan ook het meest stabiel. Verder zijn erg grote moleculen, zoals bijvoorbeeld biomoleculen, bijna alleen maar hoogveldzoekend. Als we ook deze moleculen op willen sluiten, hebben we een veld nodig dat eruit ziet als een berg: groot in het midden en steeds kleiner als je verder weg gaat. Jammer genoeg kan zo'n veld niet gemaakt worden. Het hoogste veld is altijd op de electrode, en het wordt kleiner naarmate je verder weg gaat. De enige manier dus om een maximum van elek-



Figuur 6.6: De twee zadels waartussen geschakeld wordt in een val voor hoogveldzoekende moleculen.

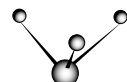
trisch veld in het midden van de val krijgen is een electrode midden in de val te zetten. Maar dan zouden de hoogveldzoekende moleculen direct naar deze electrode toevliegen, en daar tegenaan kleven. Dat willen we niet. Wat we in plaats daarvan doen is bewegende velden gebruiken. We maken twee velden die eruit zien als een zadel (zie figuur 6.6). In het midden van het zadel heeft het eerste veld een maximum in één richting en een minimum in de andere richting. Het tweede veld draait dat precies om, het heeft een minimum in de eerste richting en een maximum in de andere richting. In de richting met het maximum worden de moleculen naar het midden van de val geduwd, precies zoals we willen. Maar in een richting met een minimum worden de moleculen uit de val geduwd; het grootste elektrische veld ligt nu aan de rand van de val. Als we heel snel tussen de twee zadelvelden schakelen, zien de moleculen in alle richtingen afwisselend een minimum en een maximum. Doordat het hoogste elektrische veld zich steeds beweegt, rennen de moleculen door de val op zoek naar het maximum en blijven zo gevangen. Deze val noemen we vanwege de voortdurend wisselende spanning (en dus ook stroom) in de val een AC val. AC staat hier voor ‘alternating current’, de engelse uitdrukking voor wisselstroom.

## 6.5 Ammoniak



Voor al de experimenten die beschreven staan in dit proefschrift heb ik steeds hetzelfde molecuul gebruikt, namelijk ammoniak ( $\text{ND}_3^1$ ). Ammoniak is best een bijzonder molecuul, met een rijke geschiedenis. Het heeft bijvoorbeeld in de industrie een grote rol gespeeld.

<sup>1</sup>De normale vorm van ammoniak,  $\text{NH}_3$ , bestaat uit één stikstof atoom (N) en drie waterstofatomen (H). Van waterstof bestaat er ook zwaardere vorm, genaamd deuterium (D). Daarmee kan gedeutereerd ammoniak ( $\text{ND}_3$ ) gevormd worden.



Vroeger werd ammoniak gemaakt van verschillende stoffen die in de natuur gevonden werden. Tegenwoordig wordt het gemaakt van de stikstof in de lucht, met behulp van het zogenaamde Haber-Bosch proces. Eén van de uitvinders van dit proces, Fritz Haber, was de eerste directeur van het instituut in Berlijn waar ik ongeveer de helft van mijn metingen heb gedaan. In 1913 werd dit instituut naar hem vernoemd. De eerste toepassing van zijn geïndustrialiseerde ammoniak was in de eerste wereldoorlog, waar het door Duitsland gebruikt werd om explosieven te fabriceren. Gelukkig werd het later ook gebruikt met een wat positiever doel voor ogen, namelijk voor de productie van kunstmest, wat ertoe bij heeft gedragen de voedselsituatie op veel plekken in de wereld te verbeteren. Hiervoor heeft Fritz Haber in 1918 dan ook de Nobelprijs gekregen.

Wetenschappelijk gezien is ammoniak ook heel interessant. Ammoniak wordt bijvoorbeeld vaak als testmolecuul gebruikt. Zo is de eerste maser, de voorganger van de laser, met ammoniak gemaakt. Ook is ammoniak het eerste meeratomige molecuul dat in de ruimte is aangetroffen. En sinds kort is het ook het eerste molecuul dat in een AC val is opgesloten.

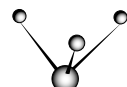
## 6.6 Mijn onderzoek

In het eerste deel van mijn proefschrift heb ik onderzocht welke kleuren licht door het ammoniak molecuul geabsorbeerd worden. In mijn geval was het ‘licht’ dat ik daarvoor gebruikt heb niet zichtbaar; het had zo’n lage frequentie dat het microgolfstraling genoemd wordt (rond de 1.6 GHz). Straling met een frequentie in hetzelfde bereik wordt ook in magnetrons gebruikt (2.45 GHz). De beweging die ik hiermee bestudeerd heb, is de zogenaamde paraplubeweging. Bij deze beweging klappen de D-atomen naar de andere kant van het N-atoom, ongeveer als een paraplu die binnenste buiten klapt. Door snel door dit proefschrift te bladeren, is deze beweging rechtsonder in de hoek te zien. In het tweede hoofdstuk heb ik dit onderzoek met snelle moleculen gedaan van 280 m/s ( $\sim$  1000 km/uur). Het nadeel daarvan is dat de moleculen te snel gaan om nauwkeurig te kunnen meten welke kleuren geabsorbeerd worden. Daarom heb ik dit experiment in het derde hoofdstuk herhaald met moleculen die met de Stark afremmer tot 50 m/s (180 km/uur) waren afgeremd. Hierdoor kon de structuur van het molecuul veel nauwkeuriger worden bepaald. Zo lagen bijvoorbeeld sommige van de kleuren die door ammoniak geabsorbeerd worden zo dicht bij elkaar, dat ik ze in het eerste experiment niet onderscheiden kon. Met de afgeremde moleculen konden de verschillende kleuren wel apart gezien worden. Dit was de eerste keer dat experimenteel bewezen werd dat een afremmer er inderdaad voor kan zorgen dat moleculen beter bestudeerd kunnen worden.

In het tweede deel van mijn onderzoek wilde ik laten zien dat ook hoogveldzoekende moleculen in een val opgesloten kunnen worden. Nadat de val was ingebouwd, heb ik hem eerst op een meer conventionele manier gebruikt, voor

het opluiten van de laagveldzoekers. Door het bijzonder veelzijdige ontwerp van de val kan er makkelijk tussen verschillende valtypen gewisseld worden. Het enige wat nodig is, is de spanningen op de elektroden op een andere manier aan te sluiten. Hierdoor kan er niet alleen een val als aan de linkerkant van figuur 6.5 gemaakt worden, maar ook een val die eruit ziet als een omgekeerde kameel, met twee putten, of een ringvormige val, die eruit ziet als een donut. Dit kan erg nuttig zijn voor toekomstig onderzoek, waarbij we bijvoorbeeld botsingen zouden willen bestuderen. Het opluiten van ammoniak moleculen in deze verschillende valtypen wordt beschreven in hoofdstuk 4.

In hoofdstuk 5 wordt beschreven hoe de val voor zijn uiteindelijke doel wordt gebruikt: het opluiten van hoogveldzoekers. Omdat de moleculen die afgeremd worden in de Stark afremmer laagveldzoekers zijn, schiet ik eerst een microgolfpuls op de moleculen af, die ervoor zorgt dat ze hoogveldzoekers worden. Direct daarna wordt de val aangezet. Met behulp van de AC val heb ik op deze manier voor het eerst in de geschiedenis hoogveldzoekende moleculen gevangen. Om erachter te komen hoe de val optimaal functioneert, heb ik de relatief vele parameters die veranderd kunnen worden bestudeerd. Hopelijk kan de val met deze kennis in de toekomst gebruikt worden om meer moleculen in het coole rijk der koude moleculen te verzamelen, zodat we meer kennis over complexere (en dus hoogveldzoekende) moleculen kunnen vergaren...



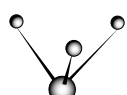


# Kapitel 7

## Zusammenfassung

Kalte Moleküle sind cool. Und wer kann das besser wissen als jemand der fünf Jahre daran geforscht hat? Dennoch fragen sich viele Menschen was eigentlich der Nutzen einer derartigen Forschung ist. Es ist letztendlich Grundlagenforschung, also dazu gedacht die Grundlagen der Welt um uns herum besser zu verstehen, ohne unmittelbar eine direkte Anwendung zu liefern. Ja, was ist überhaupt der Nutzen der Grundlagenforschung?

Dass Wissenschaft auch Menschen Spaß macht, die sie nicht betreiben, geht aus der Beliebtheit populärwissenschaftlicher Fernsehsendungen und Zeitschriften hervor. Je angewandter aber die Forschung, desto leichter fällt es, sich die Forschung selbst und auch ihre Auswirkungen auf die Gesellschaft vorzustellen. Grundlagenforschung wirkt häufig sehr abstrakt, ein Hobby für Fachidioten. Wenn man es aber näher betrachtet, stellt sich heraus, dass jeder angewandten Forschung Grundlagenforschung zugrunde liegt. Um die Welt um uns herum besser verstehen zu können, müssen wir nicht nur verstehen wie Sachen funktionieren, sondern auch warum sie funktionieren. Wenn wir unser Verständnis der vorliegenden Grundsätze erweitern können, stellt sich häufig heraus, dass sie auf weit voneinander entfernte Situationen zutreffen. Und wer kann sagen, welches kleine Stückchen fundamentalen Wissens letztendlich zu einem Durchbruch in einem anderen Gebiet führen wird, das dann unmittelbar für die Gesellschaft anwendbar ist? Möchte ich zum Beispiel besser verstehen, wie der menschliche Körper funktioniert und deswegen sämtliche großen Biomoleküle und ihre Wechselwirkungen erforschen, kann man das ohne fundamentale Kenntnis über die Zusammensetzung von Moleküle im Allgemeinen kaum machen. Und daher studieren wir auch kleinere Moleküle und entwickeln neue Techniken, die es ermöglichen, sie besser untersuchen zu können. Das machen wir aber nicht immer mit so einem deutlichen Ziel vor Auge wie dem Verstehen von Biomolekülen. Träumten die Wissenschaftler vor 100 Jahren auch von Makromolekülen und dem Verständnis biologischer Prozesse im Körper? Ich weiß es nicht. Trotzdem haben die Erkenntnisse, die sie damals gewonnen haben, dazu



beigetragen, dass wir jetzt ein besseres Verständnis von Biomolekülen haben. Wie die heutigen Wissenschaftler, begonnen sie eine Reise mit unbestimmtem Ziel, eine Reise durch einen Irrgarten, in dem jede neue Abzweigung zu einem Höhepunkt führen kann, dessen Existenz vorher noch nicht klar war. Und keiner weiß wo wir zehn Abzweigungen weiter sein werden...

Unterwegs stellt sich häufig heraus, dass nicht nur jenes Ziel wichtig ist, sondern auch die Reise selbst. Denn weil wir Techniken entwickeln um unsere Kenntnisse zu erweitern, sind es manchmal die Techniken selbst, die breiter anwendbar sind als jemand sich vorher vorstellen konnte. Schauen wir uns zum Beispiel den Laser an. Wer könnte leugnen, dass der Laser breit anwendbar ist, mit Auswirkungen auf die Gesellschaft, die die Welt in manchen Bereichen anders aussehen lässt als vorher? Der Laser wird nicht nur in der Industrie benutzt, aber auch in der medizinischen Welt hat er große Änderungen herbeigeführt. Dennoch ist der Laser ein unmittelbares Ergebnis der Grundlagenforschung. Zur Zeit seiner Entdeckung konnte keiner ahnen, wie breit der Laser jetzt verwendet wird. Für die damaligen Forscher war es lediglich ein interessanter physikalischer Prozess. Toll, neu, vielleicht anwendbar für weitere Grundlagenforschung, aber anfangs wusste keiner, ob es überhaupt gesellschaftlichen Nutzen haben würde. Und wenn die Erfinder des Lasers das schon nicht wussten, dann wussten ihre Vorgänger, die Erfinder des Masers, es sicherlich nicht. Welche fundamentale Erkenntnis war wohl außerdem noch unentbehrlich, um bis zur jetzigen Stelle in unserer Reise zu gelangen? Wahrscheinlich mehr als man denken würde. Also Gründe im Überfluss um unseren Weg auf dem Pfad der Grundlagenforschung fortzusetzen, ohne zu wissen wo wir landen werden, aber in der Sicherheit, dass die Reise uns an einigen interessanten Stellen vorbeiführen wird...

### 7.1 Temperatur

Der kleine Bereich der fundamentalen Physik, den ich erforscht habe, benutzt kalte Moleküle. Aber was bedeutet kalt eigentlich? Temperatur hat mit der Geschwindigkeit der Moleküle in der Luft zu tun. Je wärmer es ist, desto schneller bewegen sie sich im Durchschnitt. Wenn wir also von kalten Molekülen sprechen, meinen wir eigentlich langsame Moleküle. Natürlich bewegen die Moleküle in der Luft sich nicht alle gleich schnell und auch nicht alle in die gleiche Richtung. Würde das Letztere der Fall sein, würden wir nie einen windstillen Tag haben! Aber da genauso viele Moleküle gegen unsere Vorderseite stoßen wie gegen unsere Hinterseite, werden wir nicht davongeblasen. Bei Raumtemperatur ( $20^{\circ}\text{C}$ ) ist die meist wahrscheinliche Geschwindigkeit der Stickstoffmoleküle in der Luft ungefähr  $590 \text{ m/s}$ , was  $2100 \text{ km/Stunde}$  entspricht. Sogar an einem kalten Tag in Moskau, sagen wir mal bei  $-40^{\circ}\text{C}$ , ist die meist wahrscheinliche Geschwindigkeit noch immer  $530 \text{ m/s}$  ( $\sim 1900 \text{ km/Stunde}$ ). Solche hohen Geschwindigkeiten machen es schwierig diese Moleküle zu untersuchen. Deswegen

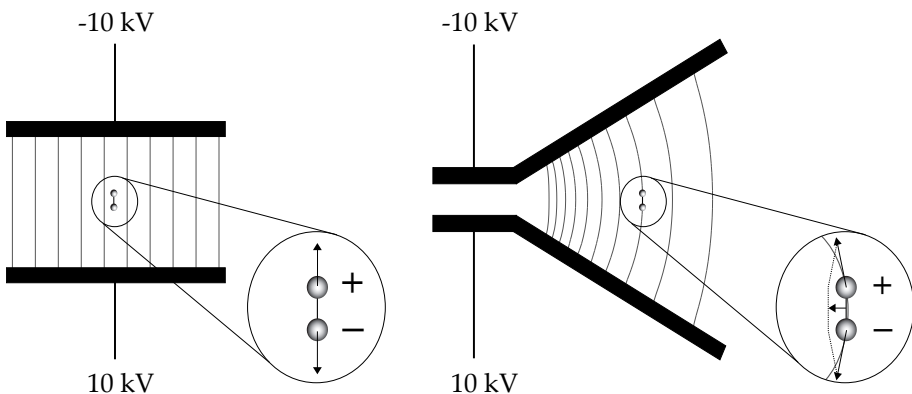


Abbildung 7.1: Auf der linken Hälfte gibt es ein dipolares Molekül in einem homogenen elektrischen Feld zu sehen. Die zwei Kräfte auf das Molekül heben sich gegenseitig auf und netto bleibt keine Kraft übrig. Auf der rechten Hälfte ist das Molekül in einem inhomogenen elektrischen Feld. Die zwei Kräfte heben sich jetzt nicht gegenseitig auf und netto gibt es eine Kraft in der Richtung des höchsten elektrischen Feldes.

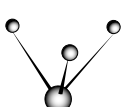
möchten wir sie abbremsen, was also das Gleiche ist wie sie abzukühlen. Die Technik, die dazu in unserem Labor<sup>1</sup> entwickelt wurde, benutzt einen Starkabbremser.

## 7.2 Starkabbremser

Um Moleküle abbremsen zu können, brauchen wir eine Kraft. Aufgrund dieser Kraft wird sich die Geschwindigkeit des Moleküls ändern. Wenn ein Molekül zum Beispiel nach links fliegt und die Kraft ist auch nach links gerichtet, dann beschleunigt das Molekül. Ist die Kraft nach rechts gerichtet, dann bremst das Molekül ab. Wenn die Kraft aus einer anderen Richtung kommt, wie zum Beispiel von unten oder von oben, dann ändert sich nicht nur die Größe der Geschwindigkeit, sondern auch ihre Richtung.

Im Starkabbremser wird die sogenannte Starkkraft benutzt. Diese Kraft wirkt auf dipolare Moleküle. Das heißt, dass die Moleküle eine kleine Ladungsungleichverteilung haben, obwohl sie insgesamt neutral sind. Die eine Seite des Moleküls ist also ein bisschen positiv, während die andere Seite des Moleküls um den gleichen Betrag negativ ist. Wenn dieses Molekül sich jetzt in einem elektrischen Feld befindet, wird auf beide Seiten des Moleküls eine Kraft aus-

<sup>1</sup>Das Labor, in dem diese Technik entwickelt wurde, liegt in Nijmegen, an der Radboud Universität. Seitdem haben die Starkabbremser kurz in Nieuwegein verweilt, wonach sie, hoffentlich für längere Zeit, an das Fritz-Haber-Institut in Berlin umgezogen sind.



geübt, zum Beispiel eine Kraft nach oben auf den positiven Teil und eine Kraft nach unten auf den negativen Teil (siehe die linke Hälfte der Abbildung 7.1). Wenn das elektrische Feld überall gleich groß ist und überall die gleiche Richtung hat (ein homogenes Feld), dann sind die beiden Kräfte gleich groß und heben sich gegenseitig auf. Insgesamt ist keine Nettokraft vorhanden, und das Molekül wird seine Geschwindigkeit also nicht ändern. Anders ist es, wenn das elektrische Feld nicht überall gleich groß ist oder wenn es seine Richtung ändert, also im Fall eines inhomogenen Feldes. Die Kräfte sind jetzt unterschiedlich und heben sich nicht mehr gegenseitig auf. Es resultiert eine sehr kleine Kraft, die bewirkt, dass das Molekül in eine bestimmte Richtung geschoben wird. Welche Richtung das ist, ist abhängig von der Orientierung des Moleküls im Feld. In der rechten Hälfte der Abbildung 7.1 ist ein Beispiel dargestellt. Das Feld, das von den zwei schrägen Platten erzeugt wird, wird nach links zunehmend größer, was dadurch deutlich wird, dass die Feldlinien einander näher sind. Auch kann man sehen, dass das Feld nicht überall die gleiche Richtung hat (die Feldlinien sind gekrümmt). Die Kraft, die dieses Feld auf den positiven Teil des Moleküls ausübt, zeigt nach links oben, während die Kraft auf den negativen Teil nach links unten zeigt. Werden beide Kräfte aufaddiert, so bleibt eine Kraft nach links übrig, also in der Richtung des größeren elektrischen Feldes. Deswegen wird dieses Molekül Hochfeldsucher genannt. Wäre das Molekül um  $180^\circ$  gedreht, dann würde die Kraft genau in die andere Richtung zeigen, nämlich in die Richtung des kleinsten elektrischen Feldes. So ein Molekül wird Niedrigfeldsucher genannt.

Gemäß der klassischen Physik könnte das Molekül auch jede Orientierung zwischen den beiden die wir gerade besprochen haben annehmen. Aber die Quantenmechanik erlaubt nur einige diskrete Orientierungen.

Der Abbremsen ist für niedrigfeldsuchende Moleküle gebaut worden. Das inhomogene Feld wird erzeugt, indem wir eine Spannung an zwei parallele Stäbchen anlegen, wie in Abbildung 7.2 dargestellt. Das Feld ist am Höchsten zwischen den Stäbchen und wird kleiner, wenn man sich weiter entfernt. Ein niedrigfeldsuchendes Molekül, das auf die zwei Stäbchen zufliegt, wird also eine Kraft spüren, die von den Stäbchen weg zeigt, also in die Richtung des kleinsten elektrischen Feldes. Dieses ist analog zu einer Murmel, die einen Berg hinauf rollt. Wie die Murmel wird auch das Molekül abbremsen, wenn es den Berg hoch fliegt. Wenn es aber schnell genug ist, um den Gipfel des Berges zu erreichen, wird es auf der anderen Seite wieder nach unten rollen und am Fuße des Berges genau die gleiche Geschwindigkeit haben wie vorher (siehe den mittleren Teil der Abbildung 7.2). Um dem vorzubeugen, schalten wir die Spannungen schnell ab, bevor das Molekül den Gipfel erreicht, und ziehen so quasi den Berg unter dem Molekül heraus. Auf diese Weise wird das Molekül nicht wieder auf seine Ursprungsgeschwindigkeit beschleunigt, sondern bleibt abgebremst, wie man auch in dem unteren Teil der Abbildung 7.2 sehen kann.

Wenn die Moleküle nicht auf den Abbremsen zu fliegen, funktioniert er natürlich nicht. Die Moleküle in der Luft fliegen in alle Richtungen, so dass

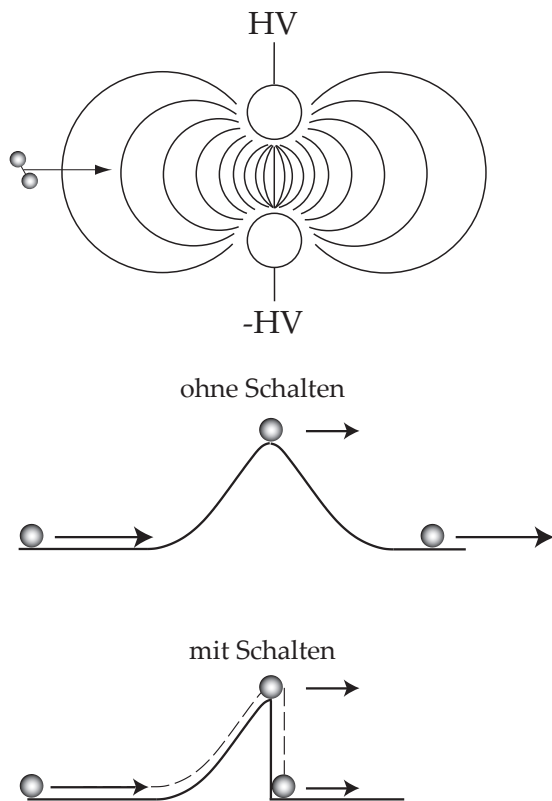
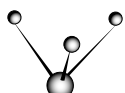


Abbildung 7.2: Ein Paar Abbremserstäbchen. Wegen des hohen Spannungsunterschiedes zwischen den Stäbchen ist das elektrische Feld zwischen den Stäbchen am Höchsten und nimmt mit zunehmender Entfernung ab. Für die Moleküle sieht es wie ein Berg aus. Die Geschwindigkeit der Moleküle wird angegeben durch die Länge der Pfeile.



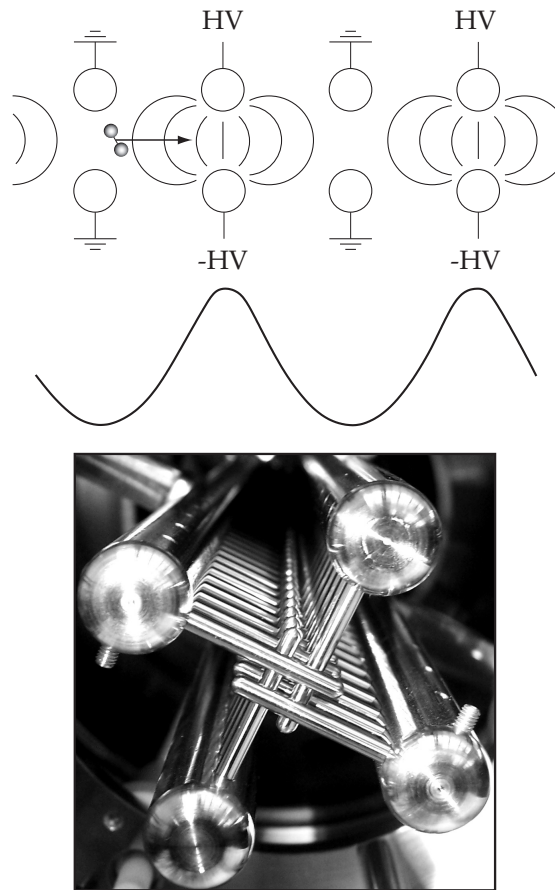


Abbildung 7.3: Schematische Darstellung und Bild des Abbremsers.

wir sie also nicht für die Abbremsung benutzen können. Deswegen nehmen wir zuerst eine Metallkammer, aus der wir die Luft heraus pumpen. Der resultierende luftleere Zustand in der Kammer wird Vakuum genannt. An die Kammer bauen wir einen mit Gas gefüllten Behälter, der mit einem kleinen Loch versehen ist. Jedes Mal, wenn wir das Loch öffnen, kommt ein Strahl Moleküle aus dem Behälter heraus, der im Vakuum in die Richtung unseres Abbremsers fliegt. Die niedrigste Geschwindigkeit, die man mit normalen Techniken erreichen kann, ist ungefähr 280 m/s ( $\sim 1000$  km/Stunde). Das ist so schnell, dass es kaum einen Effekt hätte, ließe man die Moleküle nur durch ein einziges Elektrodenpaar des Abbremsers fliegen. Wenn wir die Moleküle merklich abbremsen oder sogar zum Stillstand bringen möchten, müssen wir den Prozess einige Male wiederholen. Deswegen sieht der Abbremsr so aus wie in Abbildung 7.3

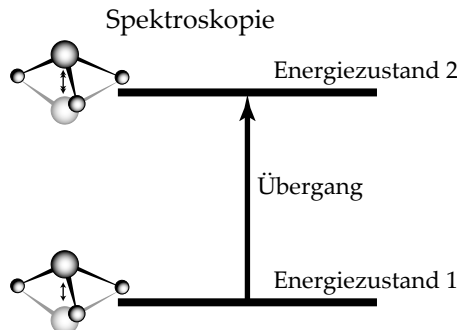


Abbildung 7.4: Ein Übergang zwischen zwei Energiezuständen. Im höheren Energiezustand vibriert das Molekül stärker.

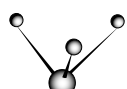
dargestellt, mit vielen Abbremsstäbchen hintereinander. Der Abremser, den ich benutzt habe, wird in dem Bild in Abbildung 7.3 gezeigt. Insgesamt gibt es 95 Stäbchenpaare, die von den größeren Stangen, die in das Bild herein zeigen, zusammen gehalten werden. Diese Stangen sind auch für die elektrische Verbindung notwendig: die ungeraden Stäbchen sind mit den großen Stangen links oben und rechts unten verbunden, während die geraden Stäbchen mit den großen Stangen rechts oben und links unten verbunden sind. Hierdurch ist jedes Abremserpaar um  $90^\circ$  gegenüber seinem Vorgänger gedreht.

An jede große Stange kann eine Spannung von 10.000 V angelegt werden. Wir legen die Spannung jetzt erst an das erste Abremserpaar an (und damit auch an sämtlichen ungeraden Paaren). Wenn die Moleküle abgebremst sind, schalten wir die Spannung schnell aus und gleichzeitig schalten wir die Spannung am zweiten Paar an (und damit auch an sämtlichen geraden Paaren). Diesen Prozess wiederholen wir bis die Moleküle am Ende des Abremses sind. Jedes Mal, wenn die Spannung an einem Stäbchenpaar ausgeschaltet wird, wird die Spannung am folgenden Paar eingeschaltet. Diese ganze Schaltserie wird von einem Rechner angesteuert. Indem wir die verschiedene Einstellwerte ändern, können wir die Endgeschwindigkeit der Moleküle so wählen wie wir möchten.

## 7.3 Spektroskopie

Moleküle kann man besser studieren, wenn sie langsam sind. Eine Möglichkeit dazu ist Spektroskopie. In der Spektroskopie wird untersucht, welche Farben des Lichts von einem Molekül absorbiert werden. Dieses funktioniert in folgender Weise.

Weil Moleküle aus mehreren Atomen bestehen, gibt es allerlei mögliche Vibratoren innerhalb des Moleküls. Klassisch gesehen würde man denken, dass jede Vibration beliebig schnell sein kann. Quantenmechanisch gesehen stellt



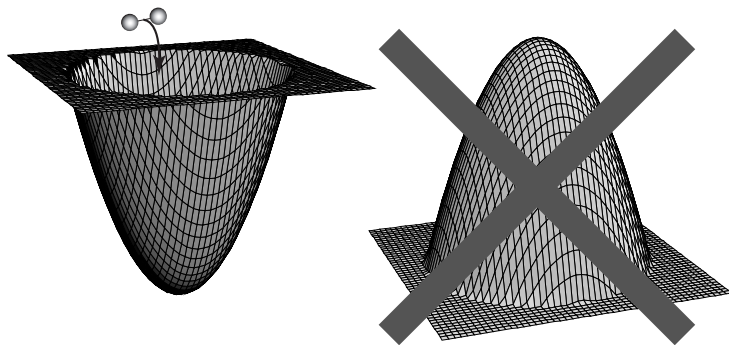


Abbildung 7.5: Links eine Falle für niedrigfeldsuchende Moleküle. Rechts das Äquivalent für hochfeldsuchende Moleküle, das nicht realisiert werden kann.

sich heraus, dass nur einige diskrete Vibrationsgeschwindigkeiten möglich sind. Zu jeder Vibrationstärke gehört eine bestimmte Energiemenge, die auch diskret ist und mit zunehmender Vibrationsgeschwindigkeit ebenfalls zunimmt. Deswegen werden alle Vibrationszustände in denen sich das Molekül befinden kann Energiezustände genannt. Wenn das Molekül von einem in den anderen Energiezustand übergeht, also wenn es mehr oder weniger vibriert als vorher, so nennt man das einen Übergang (siehe Abbildung 7.4). So ein Übergang kann verursacht werden, indem man dem Molekül eine bestimmte Energiemenge anbietet, die genau dem Energieunterschied zwischen seinem Anfangs- und Endzustand entspricht. Das kann zum Beispiel mit einem Laser gemacht werden. Die Energiemenge des Lasers hängt von seiner Frequenz ab, also von seiner Farbe. Wenn der Laser genau die richtige Farbe hat, also wenn er genau die richtige Energiemenge hat, dann wird das Licht vom Molekül absorbiert und das Molekül wird schneller vibrieren. Hätte das Molekül nun eine andere Struktur, so wird es natürlich auch anders vibrieren und andere Lichtfarben absorbieren. Wenn wir das also messen können, können wir so die Struktur des Moleküls ermitteln.

Spektroskopie kann man sowohl mit kalten als auch mit warmen Molekülen machen. Der Nachteil warmer Moleküle ist nur, dass die Farbe des Lichtes nicht so genau bestimmt werden kann und dass demnach die Struktur des Moleküls auch nicht so genau bestimmt werden kann. Deswegen ist es vorteilhaft Spektroskopie mit kalten Molekülen zu machen.

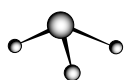
## 7.4 Eine Falle

Um noch einen Schritt weiter zu gehen im Abbremsprozess, würden wir die Moleküle gerne so langsam machen, dass wir sie in einer Falle einsperren können. Das Einsperren niedrigfeldsuchender Moleküle ist relativ leicht. Man braucht

nur ein Feld, das in der Fallenmitte klein ist und in alle Richtungen mit zunehmender Entfernung von der Fallenmitte größer wird. Wenn das Molekül langsam genug ist, fällt es in diese Falle wie eine Murmel in eine Mulde im Boden (siehe die linke Hälfte der Abbildung 7.5).

Schwieriger wird es, wenn man hochfeldsuchende Moleküle einsperren möchte. Dennoch ist es wichtig, gerade diese Moleküle zu erforschen, weil in vielen Fällen hochfeldsuchende Moleküle interessanter sind als niedrigfeldsuchende. Ein Grund dafür ist, dass ein Molekül mit geringstmöglichen Energie immer hochfeldsuchend ist. Dann ist es auch am Stabilsten. Weiterhin sind sehr große Moleküle, wie zum Beispiel Biomoleküle, fast nur hochfeldsuchend. Wenn wir auch diese Moleküle einsperren möchten, brauchen wir ein Feld, das wie ein Berg aussieht: groß in der Mitte und nach außen kleiner werdend. Leider ist ein solches Feld nicht realisierbar. Das höchste Feld ist nämlich immer an der Elektrode und nimmt mit zunehmender Entfernung davon ab. Also der einzige Weg, ein Maximum des elektrischen Feldes in die Fallenmitte zu bekommen, wäre, eine Elektrode in die Fallenmitte zu stellen. Dann würden allerdings die hochfeldsuchenden Moleküle sofort auf jene Elektrode zufliegen und an ihr kleben bleiben. Das möchten wir nicht. Stattdessen benutzen wir sich bewegende Felder. Wir nehmen zwei Felder, die jeweils wie ein Sattel aussehen (siehe Abbildung 7.6). In der Sattelmitte hat das erste Feld ein Maximum in einer Richtung und ein Minimum in der anderen Richtung. Beim zweiten Feld ist das genau umgekehrt: Es hat ein Minimum in der ersten Richtung und ein Maximum in der anderen Richtung. In der Richtung mit einem Maximum werden die Moleküle zur Mitte der Falle geschoben, genau wie wir es uns wünschen. In einer Richtung mit einem Minimum hingegen werden die Moleküle aus der Falle heraus geschoben; das höchste elektrische Feld ist jetzt am Fallenrand. Wenn wir sehr schnell zwischen diesen beiden Sattelfeldern schalten, sehen die Moleküle in allen Richtungen abwechselnd ein Minimum und ein Maximum. Da sich die Position des höchsten elektrischen Feldes ständig bewegt, rennen die Moleküle durch die Falle auf der Suche nach dem Maximum und bleiben so gefangen. Diese Falle wird wegen der ständig wechselnden Spannung (und daher auch Strom) in der Falle AC-Falle genannt. AC bedeutet hier ‘alternating current’, der englische Ausdruck für Wechselstrom.

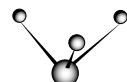
## 7.5 Ammoniak



Für alle Experimente beschrieben in dieser Doktorarbeit habe ich stets das gleiche Molekül benutzt, nämlich Ammoniak ( $\text{ND}_3$ <sup>1</sup>).

Ammoniak ist ein ziemlich besonderes Molekül mit einer reichen Geschichte. Es hat zum Beispiel in der Industrie eine große Rolle gespielt.

<sup>1</sup> Die normale Form von Ammoniak,  $\text{NH}_3$ , besteht aus einem Stickstoffatom (N) und drei Wasserstoffatomen (H). Wasserstoff hat auch eine schwerere Form, die Deuterium genannt wird (D). Damit erhält man deuteriertes Ammoniak ( $\text{ND}_3$ ).



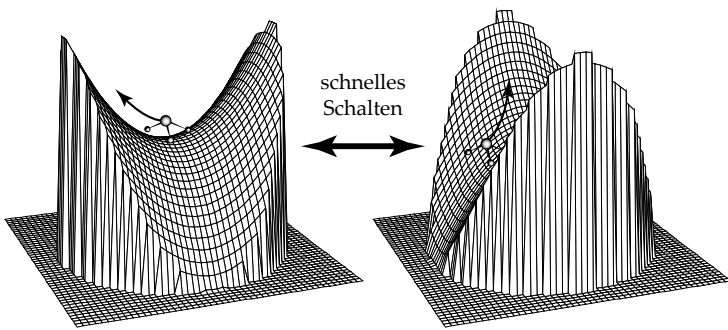


Abbildung 7.6: Die zwei Sattelformen, zwischen denen in einer Falle für hochfeldsuchende Moleküle hin- und hergeschaltet wird.

Früher wurde Ammoniak aus verschiedenen stickstoffhaltigen Stoffen, die in der Natur gefunden wurden, synthetisiert. Heutzutage wird es aus dem Stickstoff der Luft mittels des sogenannten Haber-Bosch Prozesses hergestellt. Einer der Erfinder dieses Prozesses, Fritz Haber, war der erste Direktor des Instituts in Berlin, an dem ich ungefähr die Hälfte meiner Messungen durchgeführt habe. 1953 wurde dieses Institut nach ihm benannt. Die erste Anwendung seines industrialisierten Ammoniaks war im ersten Weltkrieg, als es von Deutschland für die Sprengstoffherstellung benutzt wurde. Glücklicherweise wurde es später auch in einem positiveren Sinne benutzt, nämlich für die Erzeugung künstlichen Düngemittels, was dazu beigetragen hat, die Ernährungssituation an vielen Orten der Welt zu verbessern. Deswegen hat Fritz Haber 1918 den Nobelpreis bekommen.

Auch wissenschaftlich gesehen ist Ammoniak sehr interessant. Ammoniak wird zum Beispiel häufig als Testmolekül benutzt. So wurde der erste Maser, der Vorgänger des Lasers, mit Ammoniak gemacht. Ammoniak ist auch das erste mehratomige Molekül, das im Weltraum gefunden wurde. Und seit kurzem ist es auch das erste Molekül, das in einer AC-Falle gefangen wurde.

## 7.6 Meine Forschung

Im ersten Teil meiner Doktorarbeit habe ich untersucht welche Lichtfarben vom Ammoniakmolekül absorbiert werden. In meinem Fall war das Licht, das ich dazu genutzt habe, nicht sichtbar; seine Frequenz war so niedrig, dass man es Mikrowellenstrahlung nennt (um 1.6 GHz). Strahlung mit einer Frequenz im gleichen Bereich wird auch im Mikrowellenherd benutzt (2.45 GHz). Die Bewegung, die ich damit studiert habe, ist die sogenannte Regenschirmbewegung. In dieser Bewegung klappen die D-Atome von der einen zur anderen

Seite des N-Atoms, ungefähr so wie ein Regenschirm verkehrt umklappt. Wenn man schnell durch diese Doktorarbeit blättert, ist die Bewegung rechts unten in der Ecke zu sehen. Im zweiten Kapitel habe ich diese Untersuchung mit 280 m/s ( $\sim 1000$  km/Stunde) schnellen Molekülen gemacht. Der Nachteil davon ist, dass die Moleküle zu schnell sind, um genau messen zu können, welche Farben absorbiert werden. Deswegen habe ich dieses Experiment im dritten Kapitel mit Molekülen wiederholt, die mit dem Starkabbremser bis auf 50 m/s (180 km/Stunde) abgebremst waren. Hierdurch konnte die Struktur des Moleküls viel genauer berechnet werden. So liegen zum Beispiel manche Farben, die vom Ammoniak absorbiert werden so nahe bei einander, dass ich sie im ersten Experiment mit den schnellen Molekülen nicht unterscheiden konnte. Mit den abgebremsten Molekülen konnten die verschiedenen Farben nun einzeln gesehen werden. Dies war das erste Mal, dass experimentell bewiesen wurde, dass ein Abbremser tatsächlich für eine bessere und genauere Untersuchung von Molekülen verwendet werden kann.

Im zweiten Teil meiner Forschung wollte ich zeigen, dass auch hochfeldsuchende Moleküle in einer Falle eingesperrt werden können. Nachdem die Falle eingebaut worden war, habe ich sie zuerst eher konventionell für das Einsperren niedrigfeldsuchender Moleküle genutzt. Dank des besonders vielseitigen Entwurfs der Falle kann leicht zwischen verschiedenen Fallenarten gewechselt werden. Dazu müssen lediglich die Spannungen an den Elektroden anders ange schlossen werden. Demzufolge kann nicht nur eine Falle wie in der linken Hälfte der Abbildung 7.5 dargestellt gemacht werden, sondern auch eine Falle, die aussieht wie ein umgekehrtes Kamel, mit zwei Wellen, oder eine ringförmige Falle, die wie ein Donut aussieht. Dies kann sehr nützlich sein für zukünftige Forschung, wenn wir zum Beispiel Stöße untersuchen möchten. Das Einsperren von Ammoniakmolekülen in diesen verschiedenen Fallenarten wird in Kapitel 4 beschrieben.

In Kapitel 5 wird beschrieben, wie die Falle für ihren endgültigen Zweck benutzt wird: das Fangen von Hochfeldsuchern. Weil die Moleküle, die im Starkabbremser abgebremst werden, Niedrigfeldsucher sind, schieße ich zuerst einen Mikrowellenpuls auf die Moleküle, der sie in Hochfeldsucher überführt. Unmittelbar danach wird die Falle eingeschaltet. Mittels der AC-Falle habe ich auf diese Weise zum ersten Mal in der Geschichte hochfeldsuchende Moleküle gefangen. Um herauszufinden, wie die Falle optimal funktioniert, habe ich die zahlreichen Parameter, die geändert werden können, studiert. Hoffentlich kann die Falle mit dieser Kenntnis in Zukunft benutzt werden, um mehr Moleküle im coolen Reich der kalten Moleküle anzusammeln, so dass wir mehr Kenntnis über komplizierte (und deswegen hochfeldsuchende) Moleküle erwerben können...



# Appendix

Maxwell's equations do not allow for a three dimensional maximum in free space of the electric or magnetic field strength, using static fields. This can easily be deduced with the use of some vector algebra and the aforementioned equations (where free space implies an absence of charge or current):

$$\nabla \cdot \vec{E} = \frac{\rho}{\epsilon_0} = 0 \quad (1)$$

$$\nabla \times \vec{E} = -\frac{\partial \vec{B}}{\partial t} = 0 \quad (2)$$

$$\nabla \cdot \vec{B} = 0 \quad (3)$$

$$\nabla \times \vec{B} = \mu_0 \vec{J} + \mu_0 \epsilon_0 \frac{\partial \vec{E}}{\partial t} = 0. \quad (4)$$

In the following, the actual derivation is given for electric fields. However, the exact same arguments can be used for magnetic fields, and consequently, for combinations of magnetic and electric fields.

A maximum in the electric field occurs when the first derivative of the electric field strength  $E$  ( $= \sqrt{\vec{E} \cdot \vec{E}}$ , with  $\vec{E}$  the electric field) is equal to zero, and the second derivative is negative (when the second derivative is positive, the field displays a minimum, whereas it shows a saddle-point when it is equal to zero). Fortunately, as the square root function is strictly monotonic, it is allowed to examine derivatives of  $E^2$  instead, which simplifies the calculations somewhat. Consequently, we will strive to prove that when  $\nabla(\vec{E} \cdot \vec{E}) = 0$ ,  $\nabla \cdot \nabla(\vec{E} \cdot \vec{E}) \equiv \Delta(\vec{E} \cdot \vec{E})$  cannot be negative.

Using vector identities we can write:

$$\nabla(\vec{E} \cdot \vec{E}) = 2 \left\{ \vec{E} \times (\nabla \times \vec{E}) + (\vec{E} \cdot \nabla) \vec{E} \right\} = 2(\vec{E} \cdot \nabla) \vec{E}, \quad (5)$$

where we use Maxwell's second equation in the last step. For magnetic fields, Maxwell's fourth equation gives a similar result. We can now write for the

second derivative:

$$\begin{aligned}
 \nabla \cdot \nabla(\vec{E} \cdot \vec{E}) &= 2\nabla \cdot (\vec{E} \cdot \nabla)\vec{E} \\
 &= 2 \left( \sum_i \frac{\partial}{\partial x_i} \hat{i} \right) \cdot \left( \sum_j E_j \frac{\partial}{\partial x_j} \right) \left( \sum_k E_k \hat{k} \right) \\
 &= 2 \left( \sum_i \frac{\partial}{\partial x_i} \hat{i} \right) \cdot \left( \sum_{j,k} E_j \frac{\partial E_k}{\partial x_j} \hat{k} \right) \\
 &= 2 \sum_{i,j} \frac{\partial}{\partial x_i} \left( E_j \frac{\partial E_i}{\partial x_j} \right) \\
 &= 2 \left\{ \sum_{i,j} \frac{\partial E_j}{\partial x_i} \frac{\partial E_i}{\partial x_j} + E_j \frac{\partial^2 E_i}{\partial x_i \partial x_j} \right\} \\
 &= 2 \left\{ \sum_i \left( \frac{\partial E_i}{\partial x_i} \right)^2 + \sum_{i \neq j} \frac{\partial E_j}{\partial x_i} \frac{\partial E_i}{\partial x_j} + \sum_j E_j \frac{\partial}{\partial x_j} \sum_i \frac{\partial E_i}{\partial x_i} \right\} \\
 &= 2 \left\{ \sum_i \left( \frac{\partial E_i}{\partial x_i} \right)^2 + \sum_{i \neq j} \left( \frac{\partial E_i}{\partial x_j} \right)^2 + (\vec{E} \cdot \nabla)(\nabla \cdot \vec{E}) \right\} \quad (6)
 \end{aligned}$$

For the second term on the last line, we make use of Maxwell's second equation once more, as  $\nabla \times \vec{E} = 0$  assures that  $\frac{\partial E_i}{\partial x_j} = \frac{\partial E_j}{\partial x_i}$ . Again, Maxwell's fourth equation ensures the same result for magnetic fields. As the last term vanishes due to Maxwell's first equation (or Maxwell's third equation for magnetic fields), we arrive at:

$$\nabla \cdot \nabla(\vec{E} \cdot \vec{E}) = 2 \left\{ \sum_i \left( \frac{\partial E_i}{\partial x_i} \right)^2 + \sum_{i \neq j} \left( \frac{\partial E_i}{\partial x_j} \right)^2 \right\} \geq 0$$

and we see that a static electric (or magnetic) field can have no field-strength maximum in free space.



# Curriculum Vitae

Als middelste van drie meisjes werd ik op 25 april 1979 geboren in het Gelderse Ede. Zowel de kleuterschool als de lagere school (de Horst) lagen erg praktisch aan de overkant van de straat. Iets verder weg, maar toch nog binnen Ede lag mijn middelbare school, het Marnix College, waar ik van 1991 tot 1997 het gymnasium doorlopen heb. Op het laatste moment heb ik toen besloten een studie natuurkunde te gaan volgen, ditmaal in Nijmegen, aan de toenmalige Katholieke Universiteit Nijmegen. Als laatste onderdeel van die studie heb ik vanaf maart 2001 een jaar stage gelopen bij Gerard Meijer, die, alhoewel hij nog steeds professor aan de Nijmeegse universiteit was, zijn werk verlegd had naar een charmant FOM-instituut in Nieuwegein, het instituut voor Plasmafysica ‘Rijnhuizen’. Onder directe begeleiding van Rienk Jongma heb ik daar in de Koude Moleculen groep een opstelling opgebouwd voor inversie spectroscopie aan ammoniak moleculen.

Omdat zowel het werk als de werkatmosfeer mij prima bevonden, heb ik aan het eind van dat jaar (maart 2002 dus) besloten mijn opstelling niet uit handen te geven, maar de verdere uitbreiding met een Stark afremmer tot het begin van mijn promotie onderzoek te maken. De nieuwe metingen met de afgeremde bundel, dit keer onder begeleiding van Jochen Küpper, waren echter maar net klaar, toen de gehele groep naar Berlijn verhuisd moest worden, om hier de Abteilung Molekülphysik te vormen aan het Fritz-Haber-Institut der Max-Planck-Gesellschaft. Na in Berlijn nog wat laatste spectroscopie metingen te hebben uitgevoerd, heb ik mij de laatste jaren van mijn promotie samen met mijn derde en laatste begeleider Rick Bethlehem met het opluiten van (weer) ammoniak moleculen bezig gehouden, zowel in een meer conventionele val voor laagveldzoekers als in een AC val voor hoogveldzoekers.

# Publicatielijst

*Hyperfine structure of ND<sub>3</sub>*

Jacqueline van Veldhoven, Rienk T. Jongma, Boris Sartakov, Waldo A. Bongers, and Gerard Meijer  
Physical Review A **66**, 032501 (2002)

*Microstructured Switchable Mirror for Polar Molecules*

Stephan A. Schulz, Hendrick L. Bethlem, Jacqueline van Veldhoven, Jochen Küpper, Horst Conrad, and Gerard Meijer  
Physical Review Letters **93**, 020406 (2004)

*Decelerated molecular beams for high-resolution spectroscopy; The hyperfine structure of <sup>15</sup>ND<sub>3</sub>*

Jacqueline van Veldhoven, Jochen Küpper, Hendrick L. Bethlem, Boris Sartakov, André J.A. van Roij, and Gerard Meijer  
The European Physical Journal D **31**, 337 (2004)

*ac Electric Trap for Ground-State Molecules*

Jacqueline van Veldhoven, Hendrick L. Bethlem, and Gerard Meijer  
Physical Review Letters **94**, 083001 (2005)

*Versatile electrostatic trap*

Jacqueline van Veldhoven, Hendrick L. Bethlem, Melanie Schnell, and Gerard Meijer  
Physical Review A **73**, 063408 (2006)

*Trapping polar molecules in an AC trap*

Hendrick L. Bethlem, Jacqueline van Veldhoven, Melanie Schnell, and Gerard Meijer  
submitted

